分类号_____ 密级_____

UDC_____ 编号_____

华中师范大学

博士学位论文

质心系能量200GeV金金碰撞中中心快度区质子和反质子的产额

学位申请人姓名：刘志旭

申请学位学科专业：理论物理

指导教师姓名：刘峰 教授 许怒 教授

博士学位论文

质心系能量200GeV金金碰撞中中心快度区质子和反质子的产额

论文作者：　刘志旭

指导教师：　刘峰　教授　许怒　教授

学科专业：　理论物理

研究方向：　重离子物理

华中师范大学物理学院

2005年6月

A dissertation for Doctor of Philosophy in Physics

Proton and Anti-Proton Production at mid-Rapidity from $^{197}Au + {}^{197}Au$ Collisions at $\sqrt{s_{NN}} = 200$ GeV

The Physics of Flow, Stopping and Baryon Transfer in High Energy Nuclear Collisions

by

Zhixu Liu

Co-supervisor: Professor Feng Liu

Co-supervisor: Professor Nu Xu

Central China Normal University

June 9, 2005

Dedicate to my family for
their infinite support!

摘要

人类的好奇心驱使着我们几千年来探索同一个问题：物质的最基本的组成部分是什么？由于缺少实验的支持，对这个问题最初的回答只能是哲学上的观点。只是在最近几百年来，随着近代科技的发展，我们对这个问题的认识才越来越深入！1883年英国科学家约翰·道尔顿发展了古希腊哲学家德谟克利特的朴素的原子观点。原子又是由电子和原子核组成。原子核包括质子和中子。但随后又发现的一大批新的粒子使人们认识到这些粒子可能由更基本的结构组成，这就是夸克和胶子。并且发展了量子色动力学（QCD）来描述它们之间的相互作用：强相互作用。目前我们所了解的物质基本组成部分是夸克/胶子和轻子。QCD的两个基本特征是渐进自由和夸克禁闭，即夸克之间的相互作用在很小距离上变弱以及夸克不能以自由粒子存在，而只能禁闭在强子物质内。QCD理论预测在极高温度和（或）重子数密度下，强子物质可能会解除禁闭而以夸克胶子等离子体（QGP）的形式存在。在这种新的物质形态内，夸克和胶子可以在较大的（超出核子）范围内运动。

夸克胶子等离子体可能存在于宇宙大爆炸早期阶段（很高的温度）以及中子星（重子数密度很高）内。然而这两种情况要么是发生在过去，要么就是离我们距离太远，因此没法直接探测。在实验室里我们让两束高能重离子（高重子数密度）束流以极高的能量（高温）对撞，从而产生能量密度很高以及生存时间比较长的强相互作用物质，QGP有可能在这种环境下存在。从最早的伯克力（Berkeley）的Bevalac，到欧洲核子研究中心（CERN）的超级质子同步加速器（SPS），以及布鲁克海汶国家实验室（BNL）的交变梯度同步加速器（AGS），人们已经进行了很多有意义的工作，对高温高密度下的核物质的性质进行了大量的研究。2000年夏天，相对论重离子对撞机（RHIC）在BNL开始投入运行。RHIC的最高质心系能量（核核对撞）$\sqrt{s_{NN}} = 200$ GeV为目前最高的能量。预计2007年在CERN运行的大型强子对撞机（LHC）将有更高的质心系能量（pp对撞$\sqrt{s_{NN}} = 14$ TeV，重离子对撞$\sqrt{s_{NN}} = 5.4$ TeV）。

由于洛伦兹收缩，两个高速飞行的重离子就像两个“铁饼”一样对撞。在较低能量的情况下，两个“铁饼”会简单的弹开。随着碰撞能量的不断升高，它们会开始穿透对方从而形成高度激发的核物质并伴随着碎裂的核碎片以及其他新的粒子的

产生。如果碰撞能量继续升高，核会变得像透明似的，也就是两个“铁饼”简单的穿过对方，由于真空的激发，在它们中间能量沉积并产生新的粒子。这个系统的密度和温度会很高，粒子可能会以部分子的形式存在，QGP亦可能在中间快度区域产生。J. D. Bjørken认为在高能碰撞的情况下，在中间快度区会存在一个快度平台，从而形成一个在纵向洛伦兹平移不变的反应区域。同时由于重子数守恒，如果核是完全透明的，在中心快度区的净重子（重子减去反重子）数应该为零，这和早期宇宙的情况类似。与这种情况对应的情况是，如果核完全阻止（Landau极限），即两个“铁饼”的纵向运动完全停止，净重子数将不为零。事实上，在质心系能量大于5A GeV的情况下，核开始穿透而不可能被完全阻止。实验上直接测量所有的重子数是比较困难的，因此我们常用净质子数（质子减去反质子）来代替。“铁饼”碰撞后产生的大量粒子组成的系统由于内部压力梯度的存在会有大量的相互作用，从而朝着化学平衡和动力学平衡的方向演化。集体运动和（或）集体效应亦会对末态粒子的分布有影响。随着系统的温度的降低，系统会首先化学冻结（非弹性相互作用停止，粒子数不再改变），然后动力学冻结（弹性相互作用停止，粒子可以自由运动）。

相对论重离子碰撞过程的初态只有沿着束流方向的纵向集体运动存在。在碰撞发生后，所产生的末态粒子的运动会朝向四面八方。然而，在研究末态的集体运动时要去掉初始纵向运动的影响是比较困难的，因此研究开始没有的横向（垂直于束流方向）的集体运动会有助于比较清楚的了解在碰撞过程中发生的集体行为。横向流的产生是由于碰撞后的高温高密系统由于内部压力而扩张的自然结果。实验上常常借助于末态粒子的横动量（或横质量）分布来研究横向流。借助于热力学模型对粒子的横动量分布进行拟合能得到系统的横向流以及系统的动力学冻结条件。相对论量子分子动力学模型（RQMD）是被广泛应用的一个半经典输运模型。RQMD只包含了强子层次上的相互作用，但普遍认为在RHIC上存在着部分子层次上的相互作用。通过这个模型的研究结果和RHIC上的实验数据的比较能让我们理解强子层次的相互作用对末态粒子的影响，从而分离出部分子层次的结果。

RHIC由两个周长约为3.8公里的超导加速存储环组成，能加速从质子到金核之间的核。它是目前世界上重离子对撞能量最高（$\sqrt{s_{NN}} = 200$ GeV）的加速器。STAR实验是RHIC上较大的两个实验之一。STAR 的特点是其径迹探测器时间投影室（TPC）在中心快度区间具有全空间的方位角覆盖率。借助于不同质量和（或）电荷的带电粒子在TPC中飞行的能量损失不同，我们能进行粒子鉴别。然而随着粒子动量的升高，能量损失对质量的依赖关系变弱而无法进行粒子鉴别。加上带电粒子的飞行时间信息会有助于我们提高对更高的动量区域的带电粒子的鉴别能力。因此，一小片基于光电倍增管技术的飞行时间谱仪（TOFp）被安装

在STAR实验上。更便宜的平板阻抗玻璃板（RPC）技术也被应用到STAR的飞行时间探测器上。由于RPC技术造价更便宜，覆盖整个桶部的STAR飞行时间探测器将会采用RPC技术。

STAR的数据获取系统（DAQ）的设计是高度模块化的。不同的探测器可以根据各自的特点来实现自己的数据获取系统，然后采用规定的协议和STAR DAQ交换数据和控制信息。我们采用普通的运行Linux操作系统的PC机以及常规的CAMAC实现了TOFp DAQ系统。其前端电子学处理部分是由探测器上的前端电子学以及NIM逻辑和CAMAC插件组成。探测器上前端电子学直接将模拟信号送到CAMAC上的ADC（模拟－数字转化插件）和TDC（时间数字转化插件）转化为数字信号后被PC机读出。一台运行Linux操作系统（内核版本2.2）的PC机通过CAMAC上的I/O插件来与TOFp的本地触发系统以及STAR触发系统通信，从而决定怎样处理所获得的数据。PC机和CAMAC机箱的通信是由一块Kinetics System 2915 PCI卡和3922机箱控制器实现的。我们成功的将已有的2.0下的2915PCI卡的驱动程序移植到了2.2下。在通过触发系统的判选条件后，探测器获得的数据将通过以太网被送到STAR DAQ。

高能物理实验的大统计量决定了必须采用计算机集群系统来对这些数据进行分析处理。利用廉价的PC和大量的自由软件，我们在本地实现了这样一个集群系统。我们利用SystemImage软件实现了大量集群节点操作系统的自动安装和配置。在集群系统上我们配置了各种各样的基础服务设施，如DNS，LDAP，Kerberos，WWW，NTP，防火墙等。这些服务保证了整个集群系统的规范的和方便的管理。根据不同类型的数据，我们采用了不同的文件系统来提供文件服务。STAR以及其他公用的软件是由AFS文件系统提供的，而实验和Monte Carlo数据的访问则由NFS提供。为保证整个集群系统资源的充分和合理的利用，我们安装了批处理软件（利用SGE或者OpenPBS）以及并行计算设施如MPI，PVM等。整个系统的监控则由Nagios来提供，一旦系统的任何一个服务失败，管理员就会以给定的方式被通知到，从而尽快的恢复被中断的服务。最后系统也提供了详细的使用统计信息，这不仅可以让用户了解整个系统的运行状况，也为系统的升级改造提供了决策依据。Wiki系统被用来提供各种各样的用户支持文档以及讨论区。总的来说，我们实现的这个集群系统为本地的数据分析处理提供了坚实的基础，极大的加快了我们分析处理数据的速度。

本文报告了质心系能量$\sqrt{s_{NN}}=200$ GeV的金金碰撞中在中心快度区的质子和反质子产额。所采用的数据来自RHIC上的STAR探测器2001年运行的结果。本文报告的结果包含横动量范围$0.4<p_t<1.05$ GeV/c和快度区间$|y|<0.5$。从偏心碰撞到对心碰撞，质子和反质子的横动量分布越来越突起，这表明了在系统演化的早期阶段

较强的集体扩展行为。质子和反质子的快度分布在所测量的快度区间$|y|<0.5$内都是平坦的表明在中心快度区存在一个洛伦兹平移不变的区域。质子和反质子的产额比$\bar{p}/p \approx 0.8$在测量的快度区间$|y|<0.5$与快度无关并且从偏心碰撞（≈ 0.85）到对心碰撞（≈ 0.8）轻微减小。在RHIC能区还没有达到净重子数为零的状态。$\bar{p}/p$的轻微减小反映了在RHIC能区丰富的碰撞动力学性质：初态重子数输运和末态强子再散射都对最后的观察结果有重要的影响！

通过采用融合了径向流的热力学模型对测量的质子和反质子的产额进行拟合，我们能获得系统的动力学冻结条件。利用这个模型拟合的结果结合已经测量的结果我们能外推出所测量粒子在我们不能测到的动量区间内的产额，从而获得不同粒子的平均横动量（$\langle p_t \rangle$）。系统的动力学冻结温度从偏心碰撞（≈ 135 MeV）到对心碰撞（≈ 89 MeV）呈降低的趋势。同时这个温度还是比化学冻结温度（$\approx 160 \pm 5$ MeV）要低，这表明在RHIC能区的金金碰撞中，在化学冻结后系统还经历了一个强子再散射阶段。系统的横向流速度从偏心碰撞到对心碰撞呈增加的趋势。不同粒子（π, K, P）平均横动量对中心度的依赖关系证实了这个结论。这些粒子的平均横动量之间的差别随着中心度的增加而增加，这表明集体流的发展在中心对撞的情况下比偏心对撞更强。

利用输运模型：相对论量子分子动力学模型（RQMD），我们做了和上面实验数据分析类似的计算。不同粒子（π, K, P）的谱破坏了所谓的横质量标度不变律（m_t scaling）。平均横动量的结果尽管在绝对值上比实验数据要低，但呈现出相同的趋势。更重要的是，对绝对值的低估可能意味着更早期的集体流的发展。在RQMD模型里奇异粒子（ϕ, Ξ, Ω）的最后冻结时间以及半径的分布显示了这些粒子可能比其它非奇异粒子更早冻结。对这个结论的检验需要在实验上对这些粒子的分布进行测量。同样应用热模型对由RQMD获得的粒子谱进行拟合，系统的动力学冻结条件显示出和实验数据相同的趋势。通过让由RQMD中得到的共振态粒子在PYTHIA模型中衰变，我们研究了粒子衰变对热模型拟合结果的影响。在RQMD模型的框架下，这个影响可以忽略不计。最后，在关掉RQMD模型中的再散射后，粒子谱则呈现出横质量标度不变性，并且粒子的平均横动量对中心度的依赖关系消失。这从反面表明了再散射在重离子碰撞中的重要性。然而，在RQMD模型中只包含了强子层次的相互作用。从我们分析的结果看到，在仅包括强子层次的相互作用下系统的集体流没有实验结果所表现的强。这显示了在RHIC能区需要部分子层次的相互作用。部分子层次上的集体运动的实现对进一步的理解高能核碰撞中部分子的状态方程是很重要的。

关键词： 相对论重离子碰撞 夸克胶子等离子体 集体运动 核阻止 核穿透 重子输运 质子和反质子的产额

Abstract

The mid-rapidity proton and anti-proton yields are presented for the $\sqrt{s_{NN}} = 200$ GeV Au+Au data sets which were taken by the Solenoidal Tracker at RHIC (STAR) in 2001 run. The results are from transverse momentum range $0.4 < p_t < 1.05$ GeV/c and rapidity range $|y| < 0.5$ by using the energy loss in the Time Projection Chamber (TPC). The measured transverse momentum distribution becomes more convex from peripheral to central collisions for both proton and anti-proton implying the strong collective expansion at the early stage of the collision. The measured rapidity distributions of both proton and anti-proton are flat within $|y| < 0.5$ indicating a boost invariant region around mid-rapidity. $\bar{p}/p \approx 0.8$ is independent of the measured rapidity region $|y| < 0.5$ and decreases slightly from peripheral collision (≈ 0.85) to central collisions (≈ 0.80). It's still not net baryon free at RHIC energy. The slight decrease in the $\bar{p}/p$ ratio reflects the rich collision dynamics at RHIC: both initial baryon transfer and final stage hadronic rescatterings are important for the observation.

The kinetic freeze-out conditions are extracted by applying a thermal + radial flow fit to the proton data and $\langle p_t \rangle$ are calculated by extrapolating the measured spectra with the model. The kinetic freeze-out temperature decreases from peripheral (≈ 135 MeV) to most central collision (≈ 89 MeV). They are all smaller than the chemical freeze-out temperature ($\approx 160 \pm 5$ MeV) indicating an additional hadronic rescattering phase after the chemical freeze-out in Au + Au collisions at RHIC. The transverse flow velocity increases from peripheral to central collision. The centrality dependence of $\langle p_t \rangle$ for different particles (π, K, P) confirm this conclusion. The difference between the $\langle p_t \rangle$ of different particles (π, K, P) increases as centrality increases, this indicates that the development of collective flow is stronger in central collisions than in peripheral collisions.

The same results are also calculated by employing a transport model: Relativistic Quantum Molecular Dynamics (RQMD). The spectra of different particles (π, K, P) are not following the so called m_t scaling. While the $\langle p_t \rangle$ of them show similar trend with the experiment data despite of the underestimation of the absolute value. Furthermore, the underestimation of the absolute value might indicate early flow development. The earlier freeze-out of multi-strange particles (ϕ, Ξ, Ω) is demonstrated with this model from the freeze-out time and radius distribution of these particles. The measurements of these particles are necessary to confirm this. By applying thermal model fit to the spectra from this model, the same trend of kinetic freeze-out condition as in data is observed. The effects of resonance decay on the thermal fit parameters are also studied by letting the resonance particles decay with PYTHIA. The effect is small under this model's framework. After

switch off the rescattering in this model, the violation of m_t scaling and centrality dependence of $\langle p_t \rangle$ disappear. This indicates the importance of rescattering in heavy-ion collisions. However, only hadronic interactions are included in RQMD. Such hadronic interaction does not generate enough collective flow comparing to data. This demonstrates that partonic collectivity is needed in the heavy ion collisions at RHIC. The realization of the partonic collectivity is important toward the understanding of the partonic equation of state in high-energy nuclear collisions.

Keywords: Relativistic Heavy Ion Collisions, Quark Gluon Plasma, Collective Flow, Stopping, Baryon Transfer, Proton and Anti-Proton Yields

Contents

List of Figures

List of Tables

Chapter 1

Introduction

We human beings are always full of curiosity, and this curiosity is driving us to ask the same question over the history: what are the ultimate building blocks of matter? Thousands of years ago, people believed that different types of matter were made of different combinations of 4 things: earth, fire, air, and water. Around 400 B.C., the Greek philosopher Democritus suggested that matter was actually composed of tiny particles. He called these particles *atomos* (means indivisible). This is only a philosophical viewpoint, however. The primal atomic theory gets developed with strong experimental support until 1803. First the British scientist John Dalton improved upon Democritus's idea of atomos and developed the first "atomic" theory. Then, in 1897, J.J. Thomson dramatically changed the modern view of the atom with his discovery of the electron [1]. So the atom was not an "indivisible" particle. Subsequently, Ernest Rutherford found the existence of atomic nucleus [2] from the experiment scattering α-particles off gold foil in 1911. Atomic nucleus in turn are made of protons and neutrons which are called *nucleons*. Nucleon and many other latter found particles such as pion, kaon are called "*elementary particle*", but as the number of the so called "elementary particle" increase, people begun to doubt: is elementary particle really elementary? Then, in 1964, Gell-Mann and G. Zweig suggest that these particles may be composed of more elementary particles, $i.e.$, *quarks* [3, 4]. Soon, in 1969, during the experiment probing the internal structure of nucleons via deep inelastic electron scattering (DIS) in Stanford Linear Accelerator Center, people got the first evidence for the existence of quarks [5] (partons in Feynman's model [6]). We believe that the fundamental building blocks of matter are quarks and leptons as show in Fig. 1.1(a).

Besides these building blocks of matter, it is nature to ask the question: what holds them together? This is due to the underlying interactions of the particles. Practically according the so-called *Standard Model*, all the matter are built from the fundamental spin $\frac{1}{2}$ particles, or *fermions*, the interactions between the fermions are described as exchange of characteristic *bosons* (particles with integral spin). All the bosons are listed in Fig. 1.1(b) and table 1.1. The relative magnitudes of the four types of interaction are shown in the table too. (Please note that gravity is not included into the Standard Model.)

There are four types of fundamental interactions. Strong interactions are re-

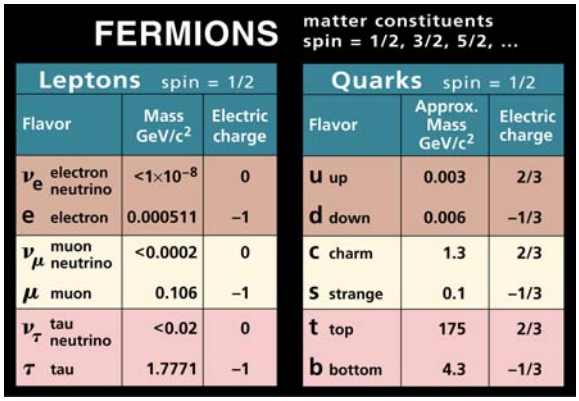

FERMIONS matter constituents spin = 1/2, 3/2, 5/2, ...

Leptons spin = 1/2

Flavor	Mass GeV/c^2	Electric charge
ν_e electron neutrino	$<1\times10^{-8}$	0
e electron	0.000511	−1
ν_μ muon neutrino	<0.0002	0
μ muon	0.106	−1
ν_τ tau neutrino	<0.02	0
τ tau	1.7771	−1

Quarks spin = 1/2

Flavor	Approx. Mass GeV/c^2	Electric charge
u up	0.003	2/3
d down	0.006	−1/3
c charm	1.3	2/3
s strange	0.1	−1/3
t top	175	2/3
b bottom	4.3	−1/3

(a)

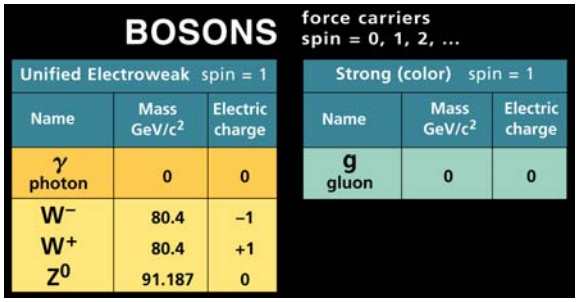

BOSONS force carriers spin = 0, 1, 2, ...

Unified Electroweak spin = 1

Name	Mass GeV/c^2	Electric charge
γ photon	0	0
W^-	80.4	−1
W^+	80.4	+1
Z^0	91.187	0

Strong (color) spin = 1

Name	Mass GeV/c^2	Electric charge
g gluon	0	0

(b)

Figure 1.1: The known fundamental building block of matter (left) and the interactions between them (right), graviton is not shown, figure from http://particleadventure.org.

Interaction	Mediator	Spin Parity	relative magnitudes	interaction range
strong	gluon, g	1^-	1	$\sim 10^{-13}$ cm
electromagnetic	photon, γ	1^-	10^{-2}	∞
weak	$W^\pm, Z^0$	$1^-, 1^+$	10^{-12}	$\sim 10^{-16}$ cm
gravity	graviton, g	2^+	10^{-38}	∞

Table 1.1: Summary of interaction mediators.

sponsible for binding the quarks in the nucleons, and the protons and neutrons within nuclei. The force is mediated by *gluon*, a massless particle. Electromagnetic interactions are responsible for virtually all the phenomena in extra-nuclear physics. *Photon* is the mediator. Weak interactions appeared in decay process such as β decay. The mediators for weak interactions are the $W^\pm$ and Z^0 bosons. Gravitational interactions act between all particles. Gravity is by far the weakest of the four interactions, although it is the dominant role of our universe. The mediator for gravity is supposed to be a spin 2 boson, the *graviton*. There are still no experimental evidences for the existence of graviton. Of the four types of interactions, gravity and electromagnetic are long ranged, the other two are short ranged.

Just have a glance at the history, who can say that the quarks/leptons are the most fundamental particles? Maybe they have internal structures too, see, for example, Ref. [7] amd [8]. Moreover, we still don't know much detail about them! This is the reason why we do experiments of relativistic heavy-ion collisions with high energy accelerators and detectors. In fact, all the high energy collision experiments can be regarded as the modern versions of Rutherford's scattering experiment. Let's do an analogy with an optical microscope. The resolution of mi-

croscope is given by $\Delta r \backsimeq \lambda / sin\theta$, where λ is the wavelength of light beam, θ is the angular aperture of the light beam used to view the object. The larger the angle of scatter θ and the smaller the wavelength λ the better the resolution is. For high energy collisions, we substitute the light beam for high energy particles and employ the de Broglie relation $\lambda = h/p$ (p is the momentum and h is Planck's constant), the resolution becomes $\Delta r \backsimeq h/(p \sin\theta) \backsimeq h/q$, q is the momentum transferred to the object scattered by the target. Thus, the bigger q the better resolution is. However, the analysis of the data from this kind of "microscope" is a very complicated process! People build detectors to take data from these microscopes, and then use computers to analyze the data. Figure 1.2 shows a typical event recorded by one of such kind of detectors.

For an excellent introduction on all the materials presented here, please refer to http://particleadventure.org/ and also Ref. [9], [10], [11] and [12].

This dissertation starts with a general introduction for the physics of quark-gluon plasma (chapter 2), followed by a description of the STAR experiment (both RHIC collider and STAR detector, chapter 3). The analysis software, method and results are presented in chapter 4. Comparisons of the results to a Monte-Carlo event generator RQMD are presented in chapter 5. Finally with the discussion (chapter 6) of the physics results and a summary (chapter 7).

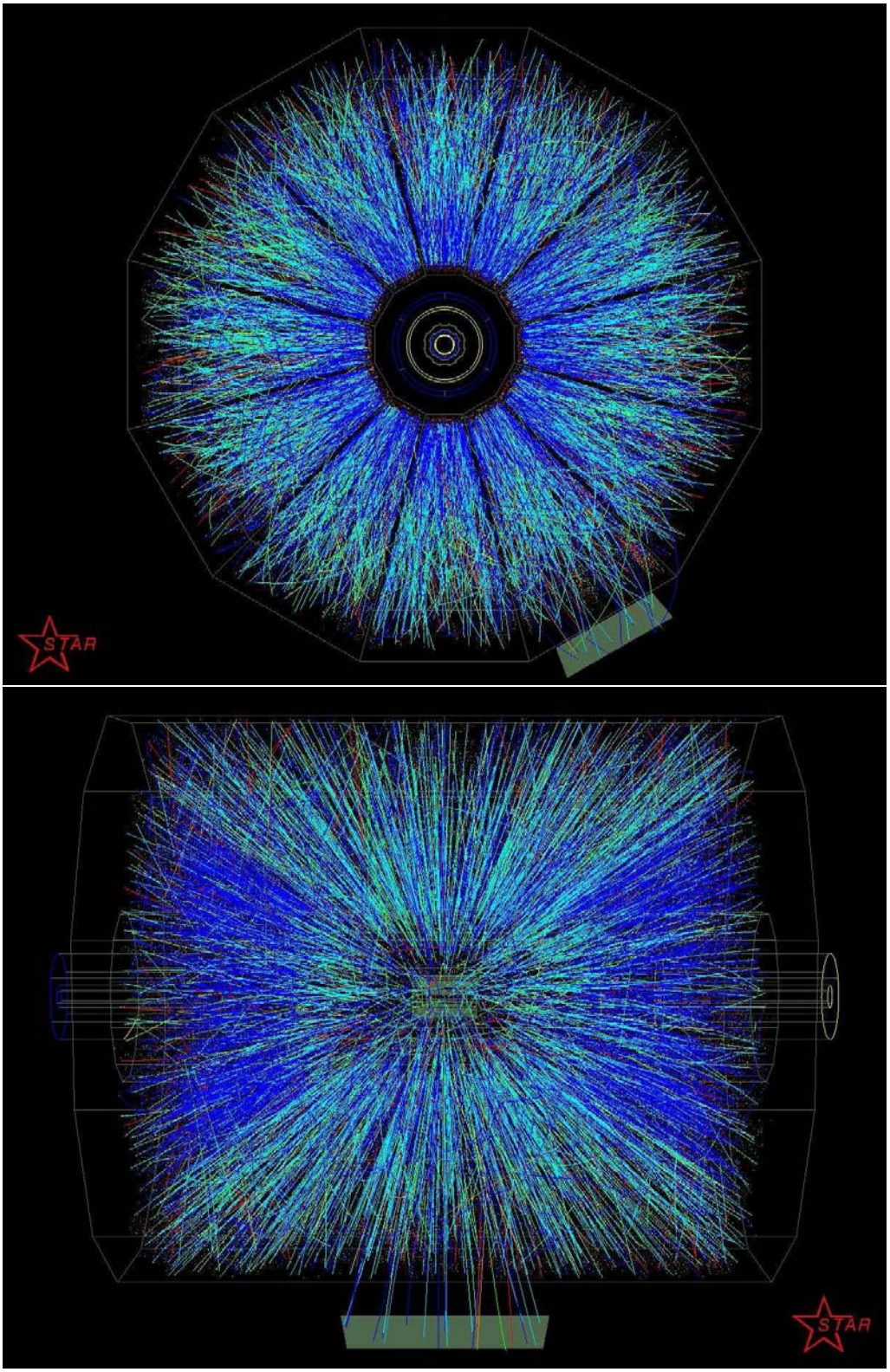

Figure 1.2: Front (top) and side (bottom) view of the first $\sqrt{s_{NN}} = 200$ GeV $^{197}Au + ^{197}Au$ collision at RHIC from STAR detector. The different colors represent different momenta. The grey rectangle which can be seen in both views is a schematic representation of the RICH detector.

Chapter 2

Physics of Quark-Gluon Plasma

As discussed in chapter 1, quarks and leptons are by far the most fundamental building blocks of matter. Leptons have no strong interactions, and they all have point-like structures under current experimental investigation. Gluon is the mediator for quark interactions. The main interactions between quarks and gluons are strong interactions. Particles consisting of quarks and gluons are called '*hadrons*' and they are classified as '*baryons*' (a baryon is built of three quarks) and '*mesons*' (a meson is built of a quark and an anti-quark).

2.1 From Hadronic Matter to Quark-Gluon Plasma

However, we have never seen free quarks. We first know its existence from DIS experiments. In these experiments, an electron (or a muon) scatters from a single quark (or anti-quark) inside the proton and transfers a large fraction of its energy to the quark. The electron exquisitely probes the quark substructure of the proton with a known spatial resolution. It is found that with high momentum transfer, the quarks and gluons inside the proton act as almost free particles. However, they are interacted with each another exceedingly strong in low-energy experiments (where only small momentum transfer), which implies the confinement at large length scale. Quantum chromodynamics (QCD) is the basic theory of strong interactions. Confinement at large distance or low-momentum interactions and asymptotically freedom [13, 14, 15][1] in short-distance or high-energy interactions are well described by QCD.

In quark model, quarks are point-like particles and confined in the hadron by a binding potential $V_0(r)$ which increases linearly with the quark separation r,

$$V_0(r) \sim \sigma r \tag{2.1}$$

where the string tension σ measures the energy per unit separation distance. Thus, to isolate a quark, infinite amount of energy are needed.

[1] 2004 Nobel Prize in Physics

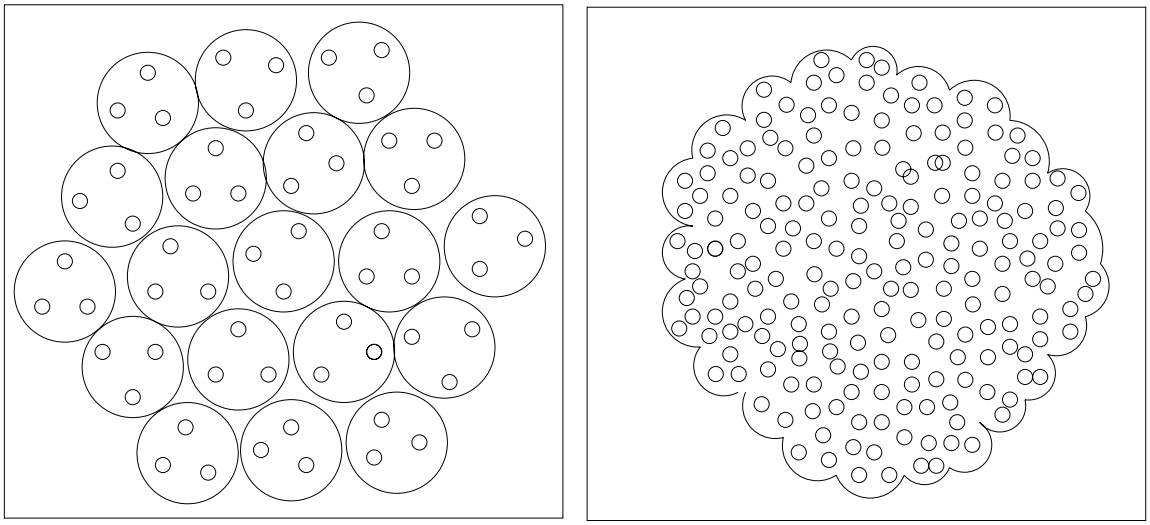

(a) (b)

Figure 2.1: Strongly interacting matter as nuclear matter at density of closely packed nucleons (a) and as quark matter at much higher density (b), figure from [16].

So it's not possible to split an isolated hadron into its quark constituents, *i.e.*, the quarks are confined in the hadrons! Confinement is a long-range feature. Now let us image what will happen if we compress the hadron matter toward higher density, *i.e.*, not trying to break them apart but push them together. We assume the nucleon with their intrinsic spatial extension is both elementary and incompressible, then a state of close packing will constitute the high-density limit of matter (Fig. 2.1(a)). Since the nucleons are built of point-like quarks, they will start to overlap with higher density, then each quark will see a considerable number of other quarks around itself (Fig. 2.1(b)). In such state, it has no way to identify which quark belongs to which hadron in the low-density state. So hadron loses its meaning, only a medium whose basic constituents are unbounded quarks. This new matter is called *Quark Gluon plasma* (QGP). In fact, let us take an analogy between QED and QCD. In QED, a so called Debye screening radius will exist in a high charge density environment which will change the Coulomb potential between the electric charges, the insulating matter will undergo a phase transition and become conducting. In QCD, the interaction of quarks is based on colour charge. Thus colour screening is expected to emerge, so the potential 2.1

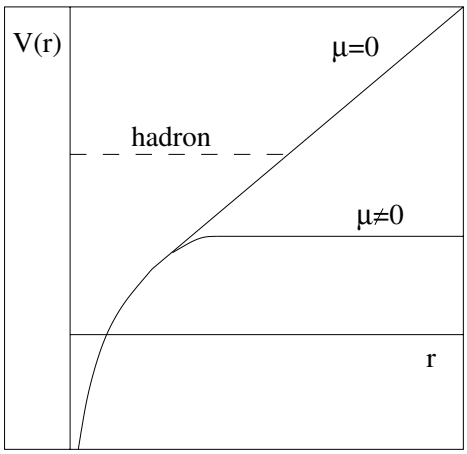

Figure 2.2: Colour screening of the confining potential, colour screening mass μ is also the inverse of the screening radius for colour charges. Figure from [16]

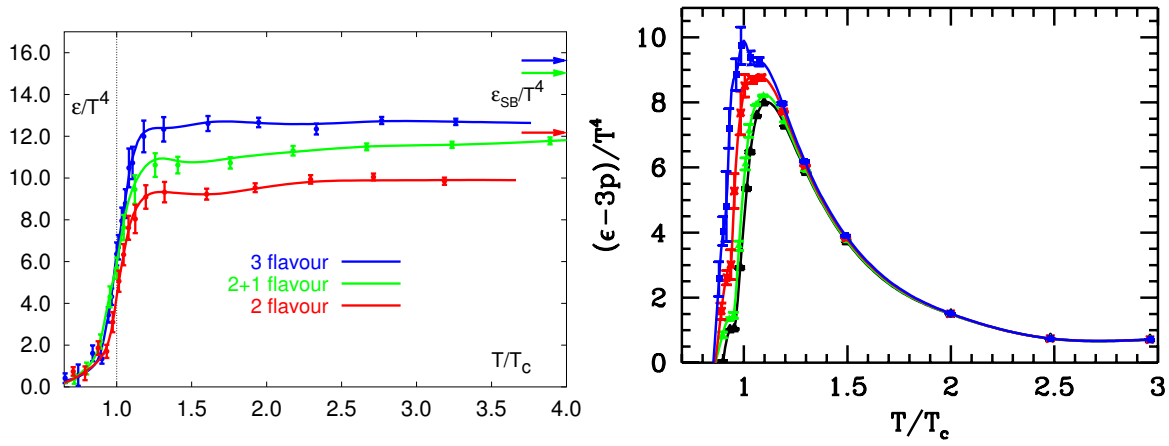

Figure 2.3: Lattice QCD results, (a) shows the energy density vs the temperature, arrows indicate the ideal gas value, figure from [20], (b) shows the energy density deviation from idea gas $\left((\varepsilon - 3P)/T^4\right)$ vs the temperature (T/T_c) at different baryon chemical potential $\mu_B = 0, 210, 410, 530$ MeV, figure from [21].

becomes

$$V(r) \simeq \sigma r \left(\frac{1 - exp(-\mu r)}{\mu r} \right) \tag{2.2}$$

where μ is the colour screening mass and also the inverse of the screening radius for colour charges. See Fig. 2.2. When $\mu = 0$, the potential increase linearly, as in equation 2.1. When $\mu \neq 0$, the potential tend to saturate as r increasing. So under colour screening, the interaction between the quarks and gluons will be short-range. The colour insulator becomes the colour conductor, the hadron matter becomes the quark-gluon plasma [16].

2.2 Lattice Treatment of QGP

QCD is a non-Abelian gauge field theory which describes the strong interactions of colored quarks and gluons. The Lagrangian of QCD is

$$\mathcal{L}_{QCD} = -\frac{1}{4} F^a_{\mu\nu} F^{\mu\nu}_a - \sum_f \overline{\psi}^f_a (i\gamma^\mu \partial_\mu + m_f - g\gamma^\mu A_\mu)^{\alpha\beta} \psi^f_\beta \tag{2.3}$$

with

$$F^a_{\mu\nu} = (\partial_\mu A^a_\nu - \partial_\nu A^a_\mu - g f^a_{bc} A^b_\mu A^c_\nu) \tag{2.4}$$

Here A^a_μ denotes the gluon field of colour a $(a = 1, 2, ..., 8)$ and ψ^f_a the quark field of colour α $(\alpha = 1, 2, 3)$ and flavour f; the input ('bare') quark masses are given by m_f. g is a free parameter to be determined from experiment. $\alpha_s = g^2/4\pi$ is the coupling constant. While α_s is related to the scale of the momentum transfer [17]. When distance scale of the interaction is small, α_s is small. This is the case of 'asymptotic freedom'. In such case, a perturbative treatment is a good description

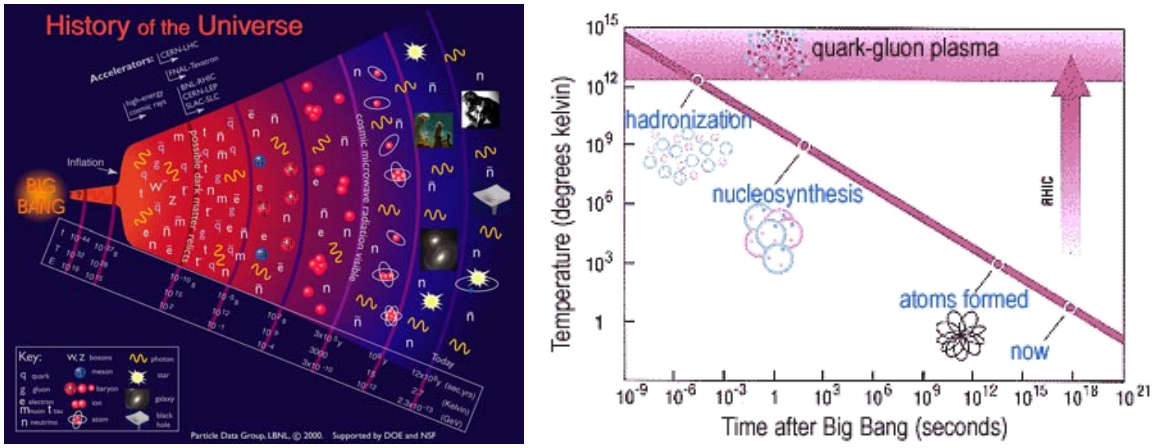

Figure 2.4: Evolution of the universe after the big bang. As you can see by the purple arrow on right plot, RHIC will recreate (on a small scale) the temperatures that existed at the dawn of the universe, this corresponding to the region before 10^{-5} seconds on left plot. Figures from http://particleadventure.org and http://www.bnl.gov/RHIC.

of the process. However, when the distance scale is large, a perturbative treatment based on an expansion in powers of the coupling constant is no longer applicable. The constituent quarks are subject to be confined and a nonperturbative treatment is needed. A phenomenological model, bag model [19], is such kind of treatment. *Lattice gauge theory* is another nonperturbative treatment of QCD formulated on a discrete lattice of space-time coordinates from the first principle.

Lattice QCD calculations based on 2 (and 3) light quark flavors and (2+1) (2 light and 1 heavier quark) quark flavors predict a cross over from hadron to QGP take place at a temperature T_c around $150 \sim 170$ MeV [20]. Fig. 2.3(a) shows the energy density, ε scaled by T^4, vs. temperature, T scaled by T_c, for 2, 3 and 2+1 flavors. At high temperature, it is expected that ε/T^4 will asymptotically approach the idea gas limit (Stefan-Boltzmann limit) which is roughly proportional to the number of particle degrees of freedom. We can see a sharp transition of energy density around T_c from the plot. However, lattice results clearly deviate from the idea gas limit until $3T_c$, Fig. 2.3(b) shows the deviations for different baryon chemical potential. This indicates strong interactions among the partons even above the cross over temperature T_c.

2.3 Relativistic Heavy Ion Collisions

QCD predicts a new state of matter QGP at extreme temperature and/or density. QGP is expected to exist in early universe, in neutron stars and high energy heavy ion collisions.

According to the Big-Bang theory of cosmology, our universe was born during the big-bang from a hot and dense fire ball about 15 billion years ago. The universe has been cooling and expanding since then. A phase transition from the QGP phase to hadron phase happened about 10^{-5} seconds after the big-bang. See Fig. 2.4. The neutron stars have high baryon density, a cold QGP is expected to

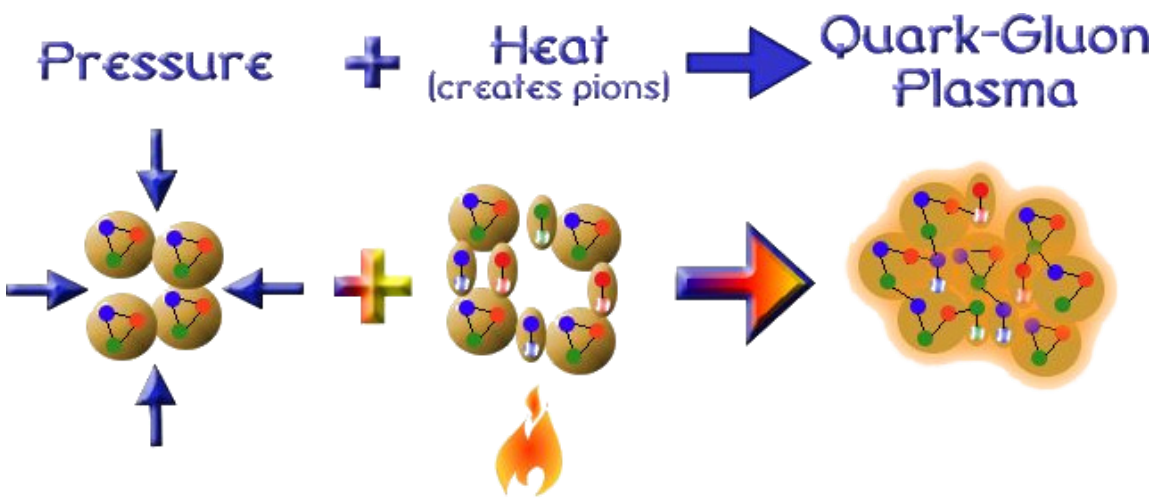

Figure 2.5: Illustration of the phase transition from hadronic matter to QGP. The red, green and blue circles are quarks, connected by black lines representing gluons. At the beginning, trios of quarks and gluons are packaged in protons and neutrons, which are held together in the nucleus of an atom. As the pressure and temperature rise, new particles called pions (made of a quark and an anti-quark, shown in pastels) arise. Finally, the conditions are just right for the phase transition to happen, and quark-gluon plasma is produced. The quarks, gluons and anti-quarks are liberated from their usual bonds, and bond with one another freely. Figure from http://www.bnl.gov/rhic.

exist there. However, they happened either in the past time or too far to reach. In laboratory, as illustrated in Fig. 2.5, by colliding two high energy heavy ion beam with each other, a large volumes of matter with high temperature and/or high energy density would be created. QGP might be created in such environments. This is why we're doing experiments beginning at Bevalac of Berkeley[2] and continuing at CERN[3] SPS[4], BNL[5] AGS[6], BNL RHIC[7] and the future CERN LHC[8]. This is the only way to search and confirm the existence of QGP in a laboratory. Also, *'confirming its existence would have a major impact on fundamental questions common to nuclear physics, particle physics, astrophysics, and cosmology'* [9].

Fig. 2.6 shows the phase diagram of strong interact matter. From this figure, we can see where normal nuclear matter sit and where the phase transition curve lie on. The area RHIC can detect is similar to the environment in the early universe. Neutron stars lie on the area with high baryon potential and low temperature.

[2] http://www.lbl.gov
[3] http://www.cern.ch
[4] http://greybook.cern.ch/programmes/SPS.html
[5] http://www.bnl.gov/
[6] http://www.bnl.gov/bnlweb/facilities/AGS.asp
[7] http://www.bnl.gov/RHIC/
[8] http://lhc.web.cern.ch/

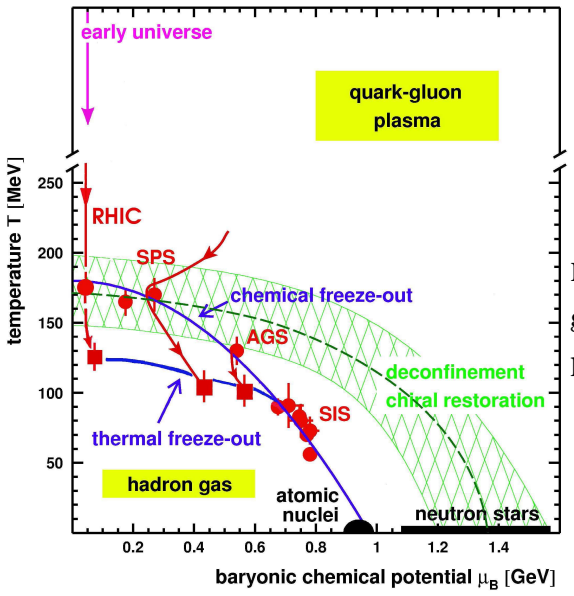

Figure 2.6: Sketch of the QCD phase diagram, temperature T vs. baryonic chemical potential μ_B, figure from [22].

2.3.1 The Space-Time evolution of Heavy Ion Collisions

Because of Lorentz contraction, the normal nuclei will look like a thin discus. In a low energy nucleus-nucleus collision, the two nuclei will remain intact and simply 'bounce off' each other. With increasing energy, they will penetrate each other more and more, leading to highly excited nuclear matter, which rapidly breaks up into nuclear fragments with the production of many mesons concentrating mostly at mid-rapidity. If the collision energy is increased still further, nuclear transparency begins to set in: the two colliding nuclei pass through each other, leaving behind them a 'vapour trail' of deposited energy, which eventually decays into hadrons [16, 26, 27, 28].

The dynamics of the collision can be illustrated in the space-time diagram with the longitudinal coordinate z and the time coordinate t, as shown in Fig. 2.7. The trajectories of the projectile nucleus and target nucleus are shown as thick lines.

The evolution of this picture is as following:

- The two lorentz-contracted nucleus interpenetrate each other. The energy density and the temperature of the system are expected to be maximum. The creation of a state of deconfined hadrons, *i.e.*, QGP, is possible in this stage. Also, hard processes with large momentum transfer occur, which will produce hadrons with high momentum.

- The interaction of the particles drives the system towards chemical and thermal equilibrium. If QGP forms, the individual parton-parton scattering is expected to play an important role in thermalizing the system during this stage. The development of collective flow is also originated. Rapid expansion (both longitudinal and transverse direction, mainly former) lowers the temperature of the system and eventually approaches the cross over temperature T_c.

- As the temperature smaller than T_c, hadronization takes place, system (*chemical freeze-out*, $T \sim 160 - 170$ MeV) freeze-out, *i.e.*, inelastic collisions have

ceased, no more new particles will be produced and the particle ratio is fixed at this point. As the system continues to cool down, elastic interactions cease finally, the momentum spectra of the particles do not change further (*kinetic or thermal freeze-out*, the hadrons can propagate freely.).

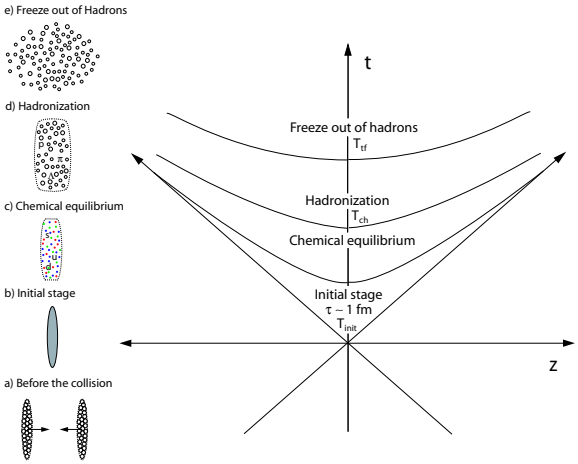

Figure 2.7: Space-time evolution of the high-energy nuclear collisions. Beams are in the z-direction and time is in the t-direction. Light-cone are indicated by the 45-degree-arrows. Different stages of the high-energy nuclear collisions, namely the initial stage, chemical freeze-out, and thermal freeze-out, are indicated by T_{int}, T_{ch}, and T_{tf}, respectively. Figure from [25].

We can only measure the final state particles in experiment. These particles provide the very useful information to determine the initial conditions such as centrality, initial spatial volume and possible energy density. Some hardronic observables are thought to be sensitive to the early stage too, such as the azimuthal anisotropy flow, v_2. Signals such as direct photons and dilepton pairs can also provide information for the early stages because of their much smaller cross section in interactions with other hadrons.

2.4 Signatures of QGP and Selected Results at RHIC

Before further discussion, it's important to give a definition of QGP. "We take the QGP to be **a (locally) thermally equilibrated state of matter in which quarks and gluons are deconfined from hadrons, so that color degrees of freedom become manifest over *nuclear*, rather than merely nucleonic, volumes**" [34]. What we see from the relativistic heavy ion collisions are just the final state particles. If QGP does exist, these final particles will provide valuable information concerning the state of the plasma despite of the possible modification by the final-state interactions in the hadronic level. However, it is generally recognized that there is no single unique signal which allows an unequivocal identification of the quark-gluon phase. Simultaneous observations of multiple hadronic observables in the final state serve as strong evidence of QGP formation [27]. In this section, we'll briefly describe some of experimental signals that have been proposed, and selected results at RHIC will also be presented. For a review on the signatures of QGP, see [29, 30]. The new experimental results and theory progress can be found at [31, 32, 33, 34, 35, 36, 37].

2.4.1 Collective Flow

Two heavy nuclei with head-on collisions with each other will produce lots of particles which will then expand and freeze-out subsequently. The underlying properties of such kind of large system will be reflected on the macroscopic quantities of the final system such as flow. Here, flow means the collectivity, *i.e.*, a common feature such as the velocity or direction observed for many particles. Historically, it's first suggested by Landau [38] to use the fluid dynamical models to describe the collisions of the nucleons and nuclei, shock waves were predicted later based on hydrodynamical calculations, and then it is argued that the particles are pushed in the transverse direction. For a review of the collective flow in heavy-ion collisions, see [39, 40] and references therein. A detail review of the hydrodynamical calculations at RHIC energy is presented in [41, 42].

The most studied flow are defined as follows: "longitudinal flow" describes the collective phenomena in the direction defined by the beam; "radial flow" means the particle emission are spherical symmetry, *i.e.*, independent of the direction; "transverse flow" denotes the azimuthal angle independence and "elliptic flow" describes the azimuthal distribution of the particles. Different flow reflects the different part of the global picture of the collisions. By assuming the system reaches thermalization, hydrodynamical model can be employed to describe the evolution of system. By using different equations of state and initial condition [43], one can predict what will happen at RHIC and then do a comparison with the experiment.

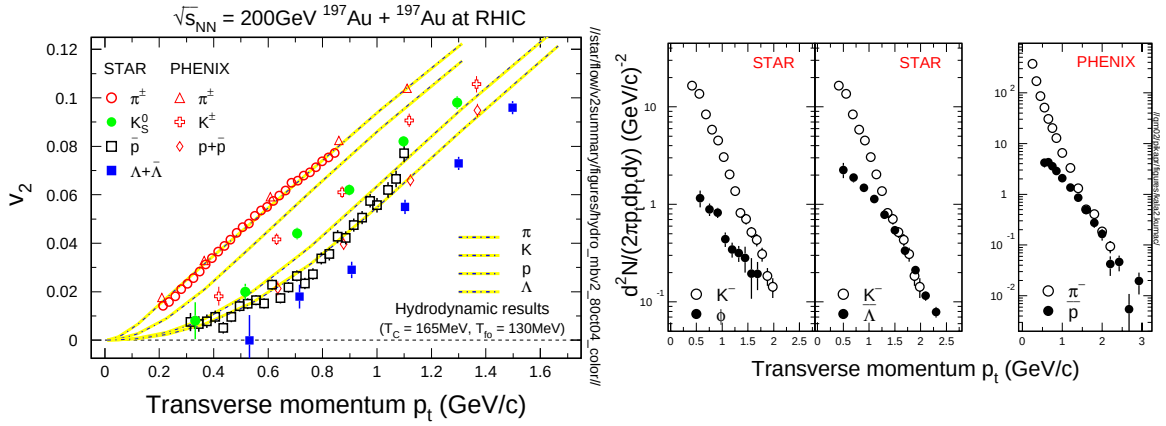

Figure 2.8: Left: $v_2(p_t)$ for K^0_S, Λ + $\bar{\Lambda}$, p, $\bar{p}$, and $\pi^{\pm}$ at RHIC ($\sqrt{s_{NN}} = 200$ GeV). Hydrodynamical calculations of v_2 for pions, kaons, protons, and lambdas are also plotted. Right: Transverse momentum from central Au + Au collisions at RHIC ($\sqrt{s_{NN}} = 130$ GeV). At $p_t \sim 2$ GeV/c heavier particle yields are approaching the lighter ones which indicating a strong collective expansion. Figure from [53].

Elliptic flow (or v_2) describes the azimuthal distribution of the final particles in momentum space. For non-central collision, the initial overlap region in coordinate space is an almond like shape, and large anisotropy in momentum space can be observed only with large rescattering in the early stage of the collisions [45]. While, elliptic flow is also self-quenching [47] as the system continues to expand. Thus elliptic flow reflects the early stage information of the system. In RHIC, v_2 of different identified particles have been measured. Fig. 2.8 left shows the results.

We can see that the v_2 of the identified particles are consistent with the hydrodynamical calculations and have mass dependence in low p_t region, this might suggest the system reaches thermalization very fast which means strong interaction and so very short mean free path at the early stage. While at intermediate p_t (not shown in the figure), hydrodynamics no longer works and v_2 saturates. Baryon saturates later and has larger value than meson. If we scale the p_t and v_2 by the number of constituent quarks (n), v_2/n vs p_t/n is the same for both baryon and meson above $p_t/n \sim 0.7$ GeV/c [55]. This is consistent with the prediction of coalescence or recombination models [48, 49, 50, 51]. More statistics are required to support this. Fig. 2.8 right shows the transverse momentum distribution from $\sqrt{s_{NN}} = 130$ GeV Au + Au collisions. We can see that the yields of the heavier particles are approaching to that of the lighter ones while has nothing to do with the number of constituent quarks. The mass dependence here clearly indicates a strong transverse collective expansion (transverse flow) at RHIC energy [53]. Hydrodynamical inspired blast wave + transverse radial flow model [56] was employed to fit the spectra to extract the kinetic parameter of the system such as the $\langle p_t \rangle$, flow velocity, etc. This will be discussed in chapter 6. Unlike elliptic flow which is sensitive to the early stage information, transverse flow is the integral over the whole period of evolution.

2.4.2 Hard Probes: Jet Quenching

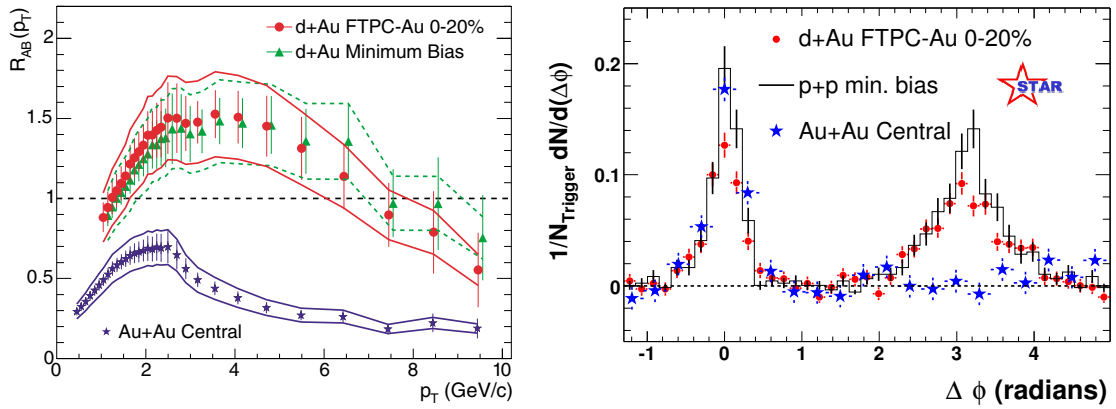

Figure 2.9: Left: R_{AB} for central Au + Au collisions, minimum bias and central d + Au collisions at $\sqrt{s_{NN}} = 200$ GeV. The minimum bias d + Au data are displaced 100 MeV/c to the right for clarity. The bands show the normalization uncertainties, which are highly correlated point-to-point and between the two d + Au distribution; right: Comparison of two-particle azimuthal distributions for central d + Au collisions and central Au + Au collisions to those seen in p + p collisions. The respective pedestals have been subtracted. Figures from [60].

It is well known that a fast charge particle will lose energy because of medium effect or radiation when traverse matter. Applying this to the QCD matter, a fast parton will suffer similar effect which is called jet quenching [57, 58]. Reflected on the final particle distribution, the transverse momentum spectrum of the particles

compared to the appropriately scaled distributions from pp collisions will show a suppression at moderate p_t region. In experiment, this is shown by using the ratio

$$R_{AB}(p_t) = \frac{d^2N/dp_t\,d\eta}{T_{AB}d^2\sigma^{pp}/dp_t\,d\eta} \tag{2.5}$$

where $d^2N/dp_t\,d\eta$ is the differential yield per event in the nuclear collision A + B, $T_{AB} = \langle N_{bin}\rangle/\sigma^{pp}_{inel}$ describes the nuclear geometry, $\langle N_{bin}\rangle$ is the mean number of binary nucleon-nucleon collisions, and $d^2\sigma^{pp}/dp_t\,d\eta$ for p + p inelastic collisions is determined from the measured p + p differential cross section. In addition, a quark or gluon jet propagating through a dense medium will not only lose energy, it will also be deflected. This will lead to an asymmetry of the high p_t particle azimuthal distribution in contrast to pp collisions. All these effects have been observed at RHIC [59, 60, 61, 62, 63]. Fig. 2.9 shows the R_{AB} and the two particle azimuthal distribution at $\sqrt{s_{NN}} = 200$ GeV. We can see both the high p_t suppression and the disappearance of away-side two-hadron correlation in central Au + Au collisions. While the d + Au results prove that the observed high-p_t suppression in Au + Au collisions are not initial effects such as the saturation of gluon densities in the incoming nuclei [64].

2.4.3 Direct Photons and Thermal Dileptons

From the cosmic microwave background radiation [66], we can get some essential information such as the temperature and evolution of the universe. The photon (both real and virtual) emission from the QGP (direct photon) is proposed as a promising signal. Because they participate in only electro-magnetic interaction, so their mean free path is large compared to the fireball. Thus they are not likely to interact with other particles and leave the reaction zone undisturbed. The dominated process of direct photon production is the compton processes $(qg \to q\gamma)$ and quark-antiquark annihilation process $(q\bar{q} \to q\gamma)$. Unfortunately, there are quite large background photon emission, such as the thermal photons from the hadron gas by hadron decay (mainly π^0 and η) and prompt photons [67] from initial hard collisions which make the measurements of direct photon rather difficult. However, the ratio of signal over background is predicted to be visible at a window near or above $p_t = 2$ GeV/c region. For a excellent review, see [68]. Similar properties (participate only electro-magnetic interaction and large mean-free-path) of direct photon can be applied to dileptons (crated by $q\bar{q}$ annihilation) too. They carry similar information as direct photon. Same difficulty of direct photon also applied to dilepton: the large background! Recently, PHENIX presented their preliminary results [69] which show the evidence of direct photon. STAR has published the photon spectra by reconstructed of $(\gamma \to e^+e^-)$ and π^0 spectra via $\pi^0 \to \gamma\gamma$ [70]. The results are helpful to understand the background better and to improve the measurements of the direct photons!

Chapter 3

STAR Experiment

The Solenoidal Tracker at RHIC (STAR)[1] [73] is one of the four experiments currently set up at the Relativistic Heavy Ion Collider (RHIC) at Brookhaven National Laboratory (BNL), USA. The other three are BRAHMS[2] [78], PHOBOS[3] [79] and PHENIX[4] [80]. STAR is one of the two large detector systems. STAR was constructed to search for signatures of quark-gluon plasma (QGP) formation and to investigate the behavior of strongly interacting matter at high energy density. The key features of the nuclear environment at RHIC are a large number of produced particles (up to approximately one thousand per unit pseudorapidity) and high momentum particles from hard parton-parton scattering. STAR will measure many observables simultaneously to study signatures of a possible QGP phase transition and to understand the space-time evolution of the collision process in ultra-relativistic heavy ion collisions. The goal is to obtain a fundamental understanding of the microscopic structure of these hadronic interactions at high energy densities.

More details about the RHIC collider, all the experiments as well as the (sub-)detectors and the computing facility can be found in a special volume of Nucl. Instrum. and Methods in Phys. Res., Sect. A [72].

3.1 The Relativistic Heavy Ion Collider

The Relativistic Heavy Ion Collider (RHIC) is located at Brookhaven National Laboratory in Long Island, New York. The basic design parameters of the collider are given in Table 3.1. The top energy for heavy ion beams (e.g., for gold ions) is 100 GeV/u and that for protons is 250 GeV. Counter-rotating beams collide head-on at six interaction points. The collider consists of two quasi-circular concentric accelerator/strorage rings on a common horizontal plane, one ("Blue ring") for clockwise beams and the other ("Yellow Ring") for counter-clockwise beams. Each ring possess a total number of 870 superconducting magnets and

[1] http://www.star.bnl.gov

[2] http://www.rhic.bnl.gov/brahms/

[3] http://www.phobos.bnl.gov

[4] http://www.phenix.bnl.gov

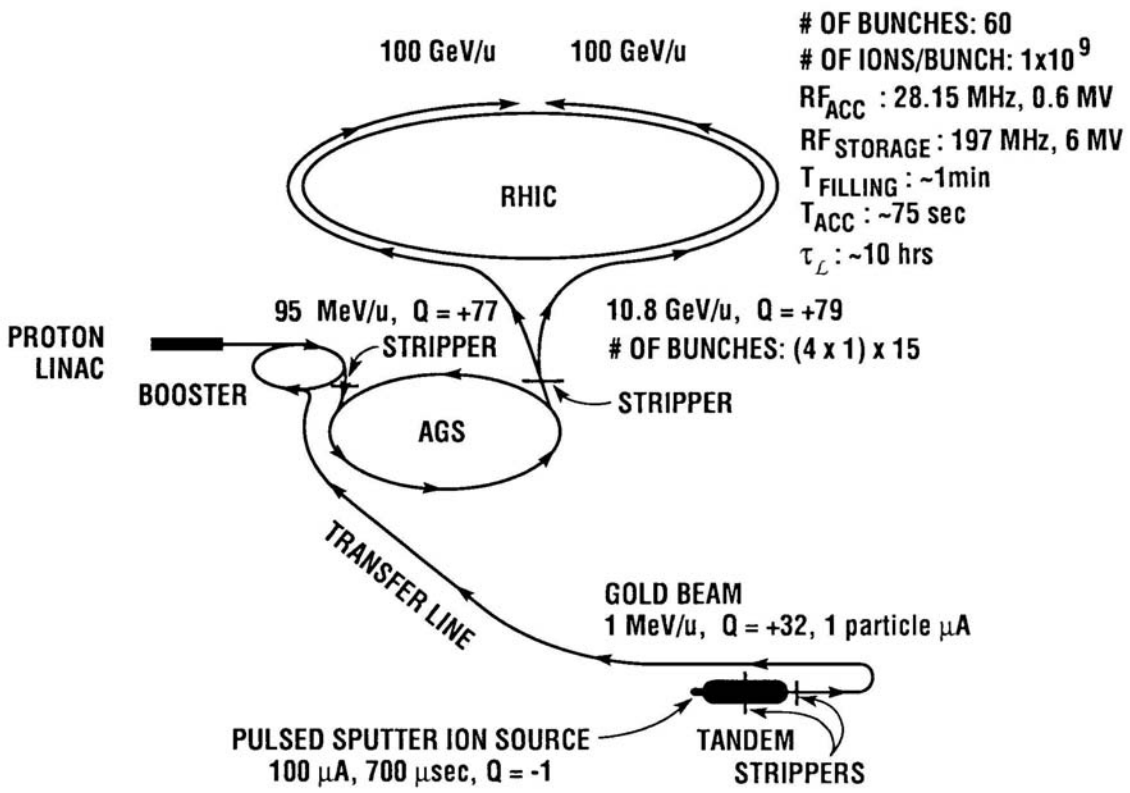

Figure 3.1: RHIC acceleration scenario for Au beams. The Tandem Van de Graaff accelerator serves for the initial ion acceleration. The ions (with kinetic energy of ~ 1 MeV/u) will then traverse an ~ 850 m long heavy ion transfer line to the Booster synchrotron and exit the Booster with kinetic energy of ~ 95 MeV/u. They will be further accelerated in the AGS. At the exit of the AGS they are full stripped and transported in the AGS to RHIC beam line to RHIC storage rings where they will be accelerated to the energy required. Figure from [75].

Parameter	For Au-Au	For p-p
Beam energy	$100 \rightarrow 30$ GeV/u	$250 \rightarrow 30$ GeV
Luminosity	$2 \times 10^{26}\ cm^{-2}s^{-1}$	$1.4 \times 10^{31}\ cm^{-2}s^{-1}$
Number of bunches/ring	60	60
Luminosity lifetime	~ 10 h	> 10 h
β^* at collision points	10 m	10 m

Table 3.1: Physical parameters and performance specifications for RHIC, data from [74, 75].

are installed in a tunnel of 3.8 km circumference. Having these two rings completely independent, collisions of unequal ion species can also be studied at RHIC.

Three accelerators in the injector chain will successively boost the energy of ions and strip electrons from the atoms. The schematic overview of RHIC complex with the acceleration scenario for Au ion beams is shown in Fig. 3.1. More details can be found at [74, 75].

The location of the 4 currently operating detectors are arranged as shown in Fig. 3.2. Two of the six interaction regions are not currently in use. If RHIC's ring is thought of as a clock face, the four current experiments are at 6 o'clock (STAR), 8 o'clock (PHENIX), 10 o'clock (PHOBOS) and 2 o'clock (BRAHMS). There are two additional intersection points at 12 and 4 o'clock where future experiments may be placed. The data presented in this thesis was taken by STAR detector. More detail about the STAR detector will be described in the following sections.

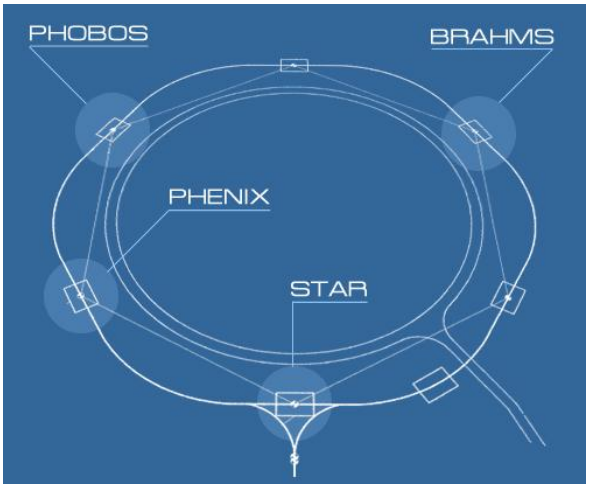

Figure 3.2: Location of the four detectors at RHIC. Figure from http://www.bnl.gov/RHIC

3.2 The Zero Degree Calorimeters

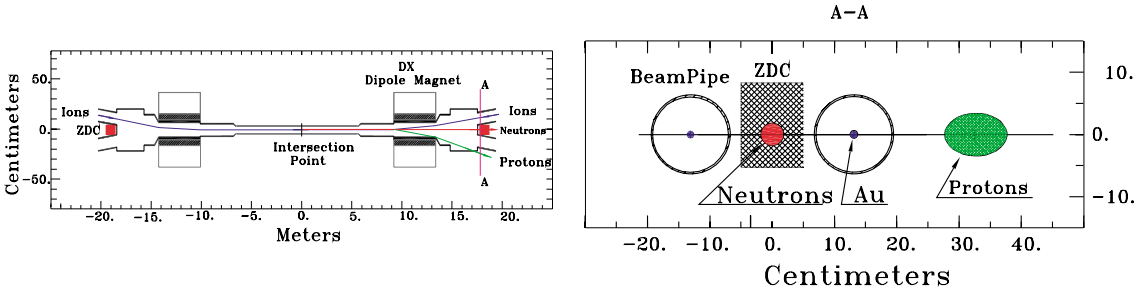

Figure 3.3: Plan view of the collision region and (section A-A) "beam's eye" view of the ZDC location indicating deflection of protons and charged fragments with $Z = A \sim 1$ downstream of the "DX" Dipole magnet, figures from [77].

In order to provide universal characterization of heavy ion collisions for all the RHIC experiments, all the four detectors have one common detector subsystem, namely a pair of ZDCs [76, 77] that are located behind the beam splitting point outside the DX magnets(~ 18 m away from the interaction point, $\theta < 2\ mrad$, so comes the name Zero Degree, see Fig. 3.3). Each ZDC module is a hadron calorimeter consisting of tungsten plates alternating with layers of undoped optical fibers, sampling the energy of spectator neutrons deposit through Cherenkov light produced by shower electrons in the fibers. The energy is known to be well correlated with the event geometry (impact parameter) of the collision. The ZDC

pair at each crossing point is also used as a luminosity monitor in steering the beams to collide. Thus, having identical sets of these detectors for all the RHIC experiments has proved to be invaluable both for machine operation, providing a ready means of monitoring and tuning the collision rate at each experimental area, and for physics analysis, providing a comparable measure of the impact parameter among the experiments for heavy-ion collisions.

3.3 The STAR Detector

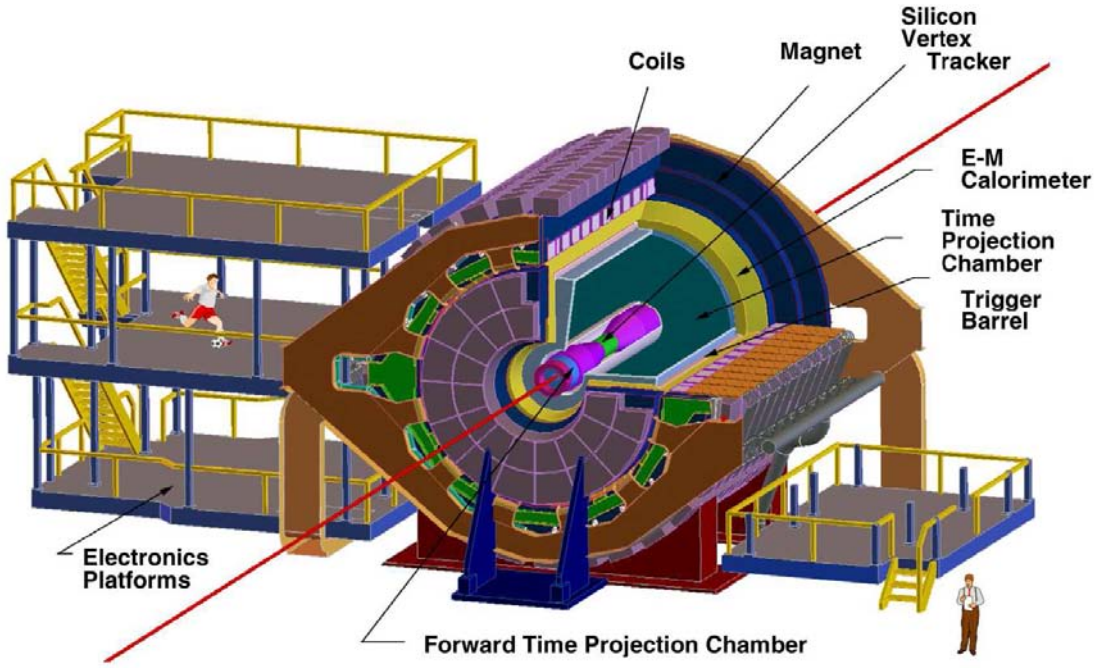

Figure 3.4: Perspective view of the STAR detector, with a cutaway for viewing inner detector systems.

STAR is located at 6 o'clock direction at the RHIC ring. To accomplish the physics goals, STAR was designed for measurements of hadron production over a large solid angle, featuring detector systems for high precision tracking, momentum analysis and particle identification at the middle rapidity.

The perspective view of the detector is shown in Fig. 3.4.

The STAR detector consists of several sub systems. A room temperature solenoidal magnet [81] with a uniform magnetic field of maximum value 0.5 T provides for charge particle momentum analysis. A Time Projection Chamber (TPC) [82] is the main tracking device. A Silicon Vertex Tracker(SVT) [83] and a Silicon Strip Detectors (SSD) [84] makes the charged particle tracking close to the interaction region possible. A radial-drift TPC (FTPC) [86] is available to extend the tracking to the forward region. To extend the particle identification capabilities to high transverse momenta, a full time-of-flight (TOF) detector will cover the outer

surface of TPC. A electromagnetic calorimeter (EMC) [87, 88] is used to measure and trigger on the total (E_t) and local $(d^2E_t/d\eta d\phi)$ transverse energy deposition. In year 2001 running period, the TPC, the FTPCs, the SVT and part of the EMC was available. A small TOF patch (TOFp) [95] was installed for test of the detector system too. The schematic side view of the detector configured for year 2001 is shown in Fig. 3.5.

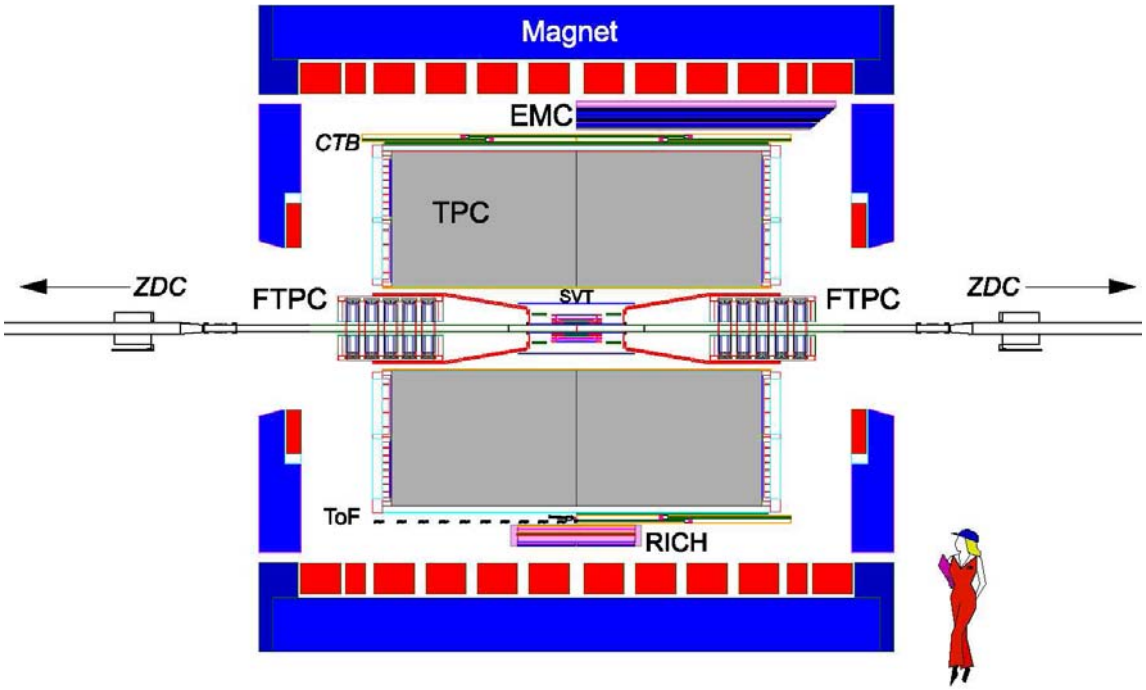

Figure 3.5: Cutaway side view of the STAR detector as configured in 2001.

The results shown in this dissertation are obtained by using STAR TPC. Also, the author has done some work for the TOFp Data Acquisition (DAQ) system [98]. So, in the following sections, I'll focus on the TPC detector, the trigger and DAQ system, the TOFp detector and the TOFp local DAQ system.

3.4 The Time Projection Chamber

TPC is the main tracking detector of STAR. It measures tracks and momenta of charged particles and provides particle identification by detecting the ionization energy loss dE/dx along the particle trajectory. The acceptance covers ± 1.8 units of pseudo-rapidity through the full azimuthal angle and over the full range of multiplicities. Particles are identified over a momentum range from 100 MeV/c to greater than 1 GeV/c, and momenta are measured over a range of from 100 MeV/c to 30 GeV/c. One can consider the TPC as a large 3D digital camera with a corresponding number of 70 million pixels which records the very detailed picture of the heavy-ion collisions.

The TPC is shown schematically in Fig. 3.6. It sits in a large solenoidal magnet that operates at 0.5 T axial magnetic field. The TPC is 4.2 m long and 4 m (1 m)

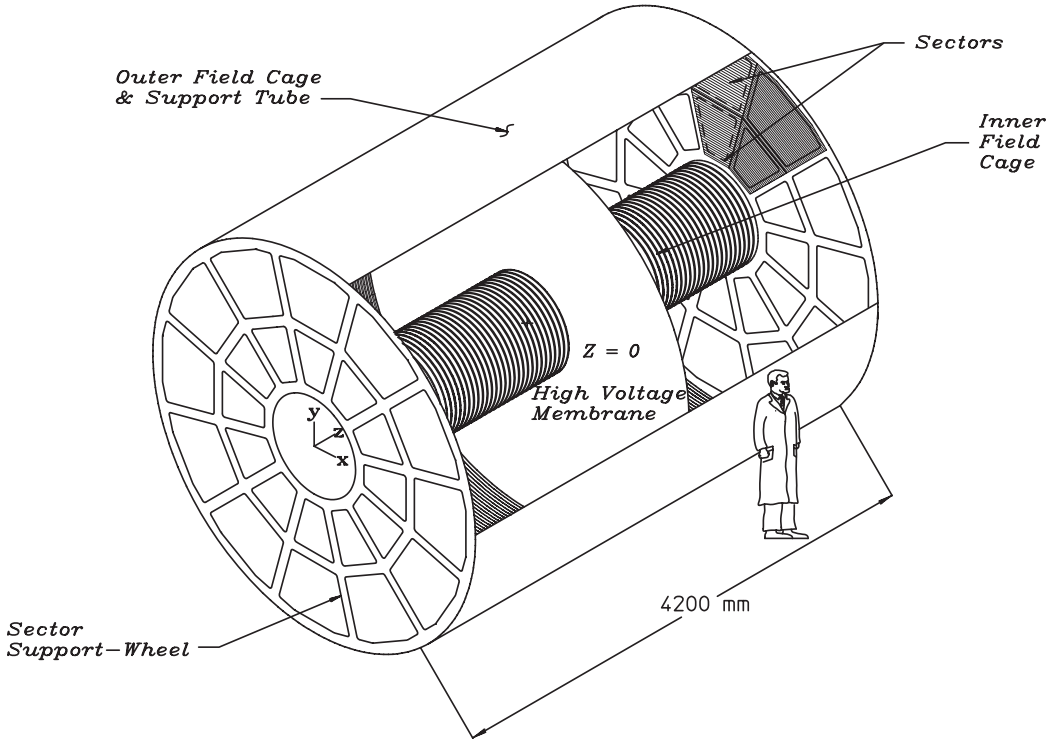

Figure 3.6: The Time Projection Chamber of the STAR Detector.

in outer (inner) diameter. The central membrane separates the detector into two parts. Each half is then divided into 12 sectors.

The TPC is an empty cylindric shaper filled with P10 gas (10% methane, 90% argon) [94] regulated at 2mbar above atmospheric pressure in a well-defined, uniform, electric field of ≈ 135 V/cm. Charged particles passing through here will ionize the gas molecules. The secondary electrons drift in the electrical field to the readout end caps at the ends of the chamber. The drift paths are up to 2.1 m. So the electric field uniformity is critical. The electric field is generated by the central membrane which is operated at -28 kV. The two end caps are grounded. The field cage cylinders provide a series of equi-potential rings that divide the space between the central membrane and the anode planes into 182 equally spaced segments. The rings are biased by resistor chains of 193 precision 2 $M\Omega$ resistors which provide a uniform gradient between the central membrane and the grounded end caps. The laser system [85] is used to measure the drift velocity with $\sim 0.02\%$ accuracy. The velocity was measured as 5.45 cm/μs.

The readout is based on a Multi Wire Proportional Chamber (MWPC) with read-out pads. Fig. 3.7 is the schematic view of the readout system. There are three wire planes. The first plane is the so-called "Gating Grid" which can control the electron in or not. Set all the wires to the same potential (typically 110 V), the drifting electron is able to enter the read-out system. Setting the wires to alternat-

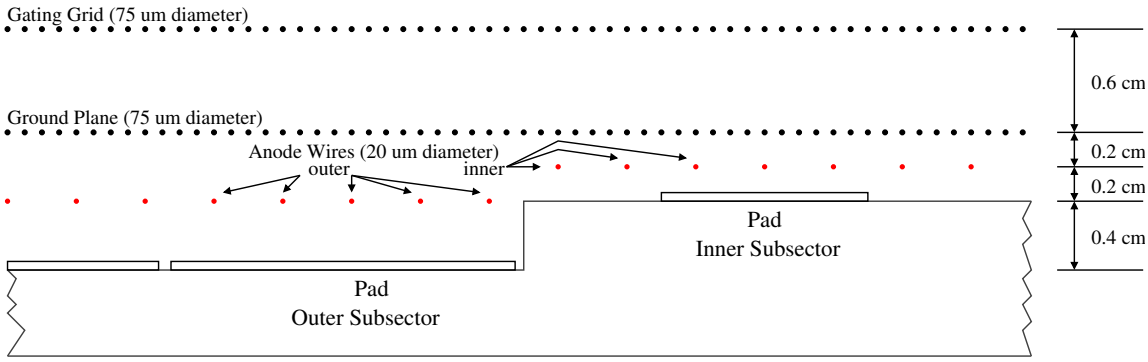

Figure 3.7: Schematic cross-section view of the TPC read-out plane.

ing ± 75 V of the nominal value will disable the electron in and clean the read-out plane for the next event. The next two wire planes and the pad plane construct the MWPC. The electric signal is amplified by the anode wire and a temporary image charge is induced on the pads. This image charge is then measured by a pre-amplifier/shaper/waveform digitizer system with a sampling rate of 100 MHz, binned into 512 time buckets. The signal location in the pad plane gives the position in x,y plane. The z position can be located with the drift time of the signal and the known drift velocity. Thus the 3D picture of a particle track is reconstructed.

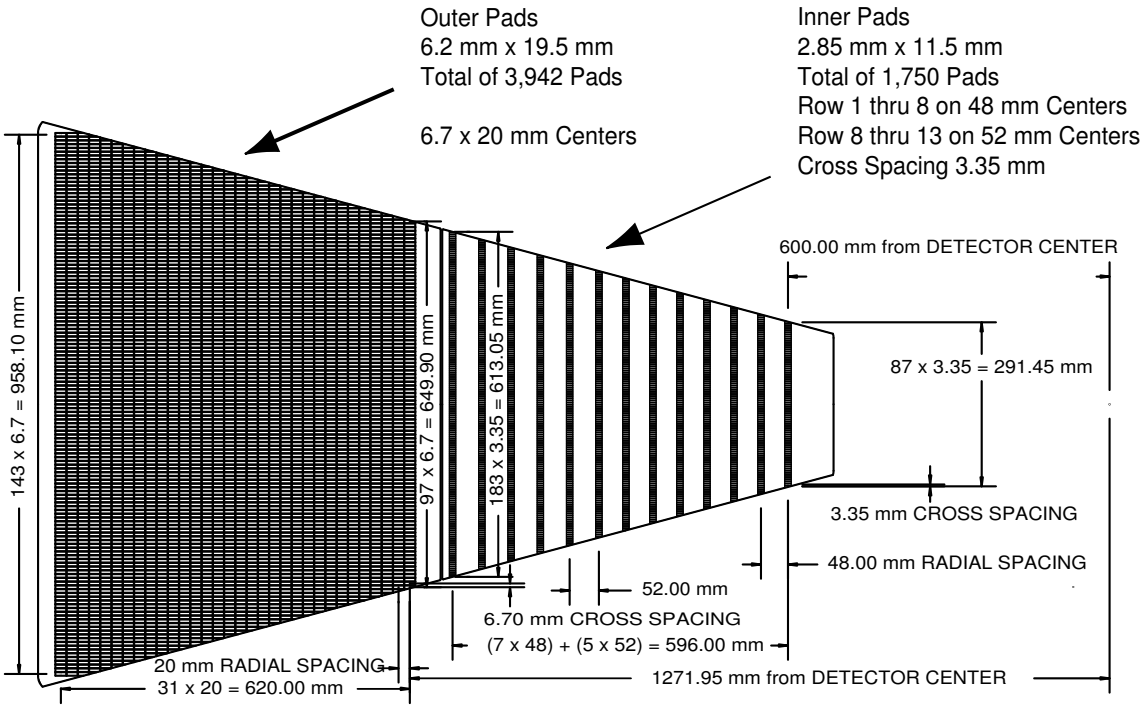

Figure 3.8: The anode pad plane with one full sector of STAR TPC.

The pad plane layout for one sector is show in Fig. 3.8. This layout is separated into an outer part with full pad coverage, optimized for the dE/dx resolution, and an inner part with smaller pad size to improve two-track and momentum resolution for low momentum tracks. There are 13 padrows in the inner subsector and

32 in the outer subsector. A particle track can be sampled with up to 45 points. There are total 5692 pads in the 24 sectors.

3.5 The Trigger and DAQ

3.5.1 The Trigger

The STAR trigger system [90] is a pipelined system in which digitized signals from the fast trigger detectors are examined at the RHIC crossing rate[5]. Data flow through the system is shown in Fig. 3.9.

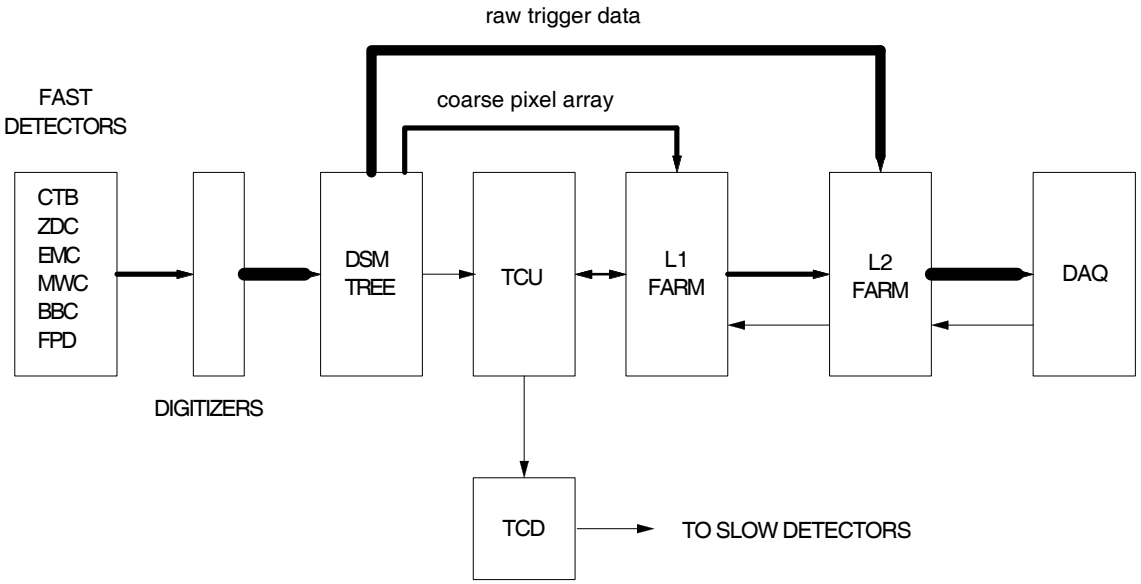

Figure 3.9: DAQ Flow through the trigger.

The system is divided into 4 layers. Level 0 is the fastest level and is used to trigger on the collision geometry and interaction vertex. The next level (Level 1 and Level 2) will apply more sophisticated constraints on the event selection. STAR has a Level 3 trigger system [91] which issues a trigger decision upon a complete online reconstruction of the collisions on a dedicated farm. An online display is included in the level 3 trigger system. Individual events can be visually inspected in real time. Fig. 1.2 shows two such plots of the first Au+Au collisions at $\sqrt{s_{NN}} = 200$ GeV.

The fast detectors that provide input to the trigger system are the Central Trigger Barrel (CTB) which covers the outer shell of the TPC and two Zero Degree Calorimeters (ZDCs). The CTB is a scintillator array with 240 scintillator arrays and measures the charged particle multiplicity with pseudorapidity $|\eta| < 1$ and azimuth in 2π. In run 2001, one of the CTB trays was removed and replaced with a TOFp tray. The ZDCs measure the neutron multiplicity in a small solid angle near zero degree with respect to the RHIC beam axis. The correlation between

[5]Typically 9.37 MHz

the sum of the ZDC pulse heights and that of the CTB is shows in Fig. 3.10 for AuAu events with successfully reconstructed primary TPC tracks. A minimum bias trigger requires the pulse height is larger than that of one neutron in each of the ZDCs. The central trigger is implemented by selecting events with less energy in the forward ZDCs but with sufficient CTB sum signal.

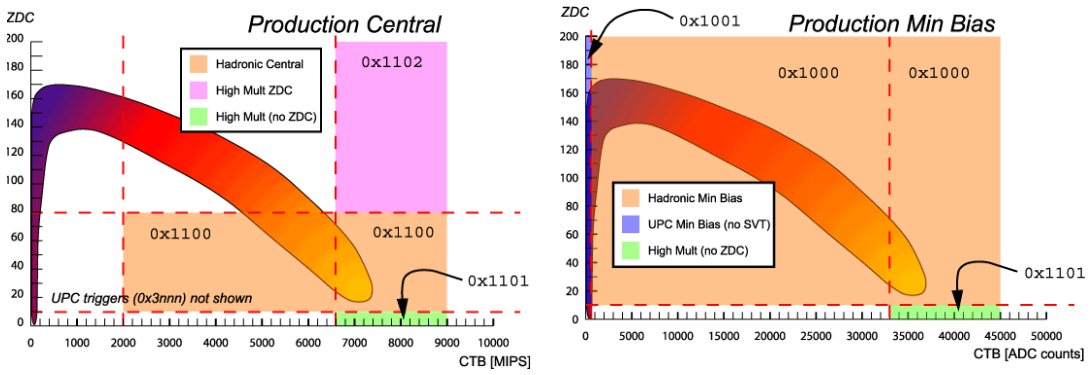

Figure 3.10: STAR trigger scheme for central (left) and minimum-bias (right) triggers. Figures from http://www.star.bnl.gov/STAR/html/all_l/trigger2001/index.html.

Besides CTB(which will be completely replaced by TOF) and ZDC, there are many other detectors can be used in trigger system to select particular physics events. Such as EMC, TOF, etc. Indeed, during year 2002, the TOFr (one TOF tray based on multiple resistive plate chambers technology) [96, 97] is added to trigger system to select events with enough hits on the tof detector system, and many important physics results have been obtained.

3.5.2 The DAQ

The STAR DAQ system [89] is driven by the characteristics of STAR's main detectors, TPC, and to a lesser degree two smaller FTPCs and a SVT. These detectors produce 80 MB of data per event and are able to read out events at 100 Hz. The storage of raw data is managed by RCF (RHIC Computing Facility)[6] using HPSS[7], the limit for STAR is 30MB/s. So the task of DAQ is then to read data from the detectors at rates up to 8,000 MB/s to reduce the data rate to 30MB/s, and to store the data in the HPSS facility. There are many other detectors that need to be read out too, but all with smaller data volumes. Thus, STAR DAQ system is a modular design.

The large input data is processed parallel at the DAQ front end. Multiple receiver boards (RBs) receive data in parallel on separate optical fibers from the detectors. The RBs are grouped together in VME crates. Each crate is controlled by a Detector Broker CPU (DET). Two strategies (zero-suppress and l3 for physical filter) are used to reduce the data volume. Events from small detectors are read into MVME processors over private, point-to-point 100MB/s ethernet. The internal implementation of the detector broker is different for each detector. The detector

[6] http://www.rhic.bnl.gov/RCF

[7] http://www4.clearlake.ibm.com/hpss/index.jsp

brokers present a detector-independent interface to the DAQ network. After all the events are read into the DETs, the Global Broker (GB) assigns these events to L3 and wait for an event decision. If the event is rejected, GB instructs the DETs to release the buffers associated with this event. If the event is accepted by L3, the event is transferred to the Event Builder (EVB). The EVB collects and formats all of the data, then instructs the DETs to release the buffers associated with the event and passes the event to a Spooler which handles the writing of the event to RCF. The spooler will transfer the data to RCF. A fraction of the data is written to a event pool for online monitoring too.

3.6 The Time of Flight patch

Charged particle identification (PID) of the TPC only covers a small range of particle momenta. The range for kaons (protons) is $0.1 \lesssim p \lesssim 0.7$ GeV/c ($0.1 \lesssim p \lesssim 1.0$ GeV/c). Thus, a time-of-flight patch is proposed to extend the STAR PID capabilities to higher momentum range, a small acceptance Time-Of-Flight(TOF) system is added to the STAR detector.

A TOF system in STAR at the cylindrical radius of the TPC with a total time interval resolution of 100 ps has the PID capabilities as indicated in Fig. 3.11.

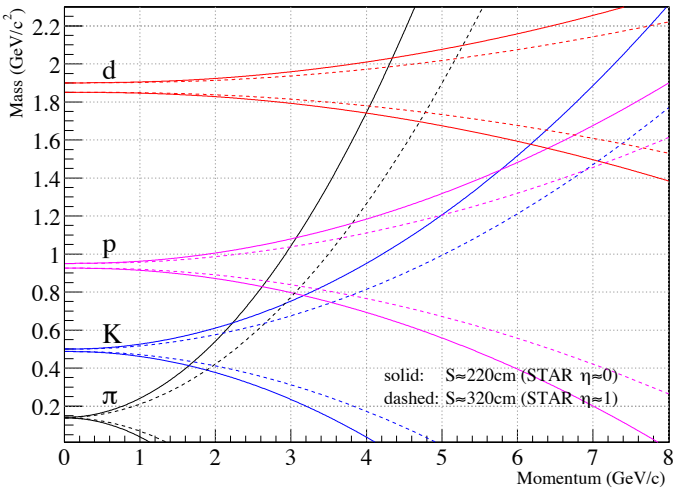

Figure 3.11: The momentum dependence of the particle identification capabilities of a TOF system with a timing resolution of 100 ps in the STAR geometry and with the STAR TPC's resolution on the track momentum and path length.

The detectors consist of two separate STAR subsystems. The electronic signals from these detectors define the time intervals of interest for particle Time of Flight measurements - the Pseudo Vertex Position Detector (pVPD) is the start detector and the Time-Of-Flight Patch (TOFp) is the stop detector. The arrangement of these systems with respect to the STAR TPC and the RHIC beam pipe is shown in Figure 3.12. The pVPD consists of two identical detector assemblies that are positioned very close to the beam pipe and outside the STAR magnet. The TOFp sits inside the STAR magnet immediately outside the TPC. The signals from these detectors are carried to electronics racks on the so-called South Platform next to STAR for digitization and interfacing with the STAR data stream.

In RHIC full-energy Au+Au collisions, large numbers of very forward, very high energy, photons are produced which travel away from the collision vertex effectively as a prompt pulse. Measuring the times when these very forward particle

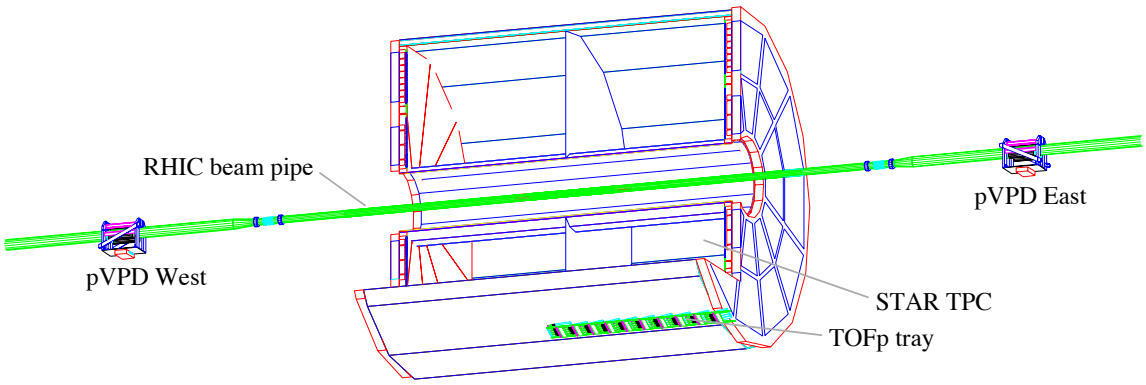

Figure 3.12: A scale drawing of the locations of pVPD and TOFp detectors in relation to the STAR TPC and the RHIC beam pipe. For clarity, the TPC is cut away, while the STAR magnet and other subsystems are not drawn.

pulses arrive at equally spaced detectors on each side of STAR provides the location of the collision vertex along the beam pipe. The average of these two arrival times is the event start time, which with the TOFp stop times provides the time interval measurements of interest. To perform this function we implemented another new detector for STAR called the Pseudo Vertex Position Detector (pVPD). The design of this detector is based on the conventional technology of plastic scintillator read-out by photomultiplier tubes. There are three pVPD detector elements on each side of STAR at a distance of approximately 5 m from the intersection region.

The detector measuring the particles of interest - the stop detector - is the Time of Flight Patch (TOFp). The goal of the system is to provide direct particle identification for the formation of the rates and spectra of charged hadrons produced in RHIC in a small acceptance but over many events. The detector design is also based on the conventional technology. A total of forty-one detector assemblies are arranged as one row of five slats and nine rows of four slats inside the TOFp tray, which in total cover approximately one unit of pseudorapidity and $\sim$1/60 of the full azimuth of the STAR TPC.

The signal processing of the system is following: starting from the outputs of the PMT bases on the detectors, the signal will pass the Front-End Electronics (FEE), the platform discriminators, and the signal cabling, finally to the inputs of the digitizers which are the ADCs and TDCs on the platform.

The STAR trigger system will issue a Level-0 trigger which is issued no later than 1.5 μs after the collision. However, the signals from the TOFp and pVPD detectors are available on the platform $\sim$240ns after the collision, and it is not practical to delay the digitization of these signals for the additional $\sim 1.3\mu$s needed to check if this event is later accepted by the STAR Level-0 trigger. Thus, the digitization of the TOFp and pVPD data is begun earlier, after a local decision based on the information from the pVPD itself. As the pVPD, CTB, and ZDC detectors cover different non-overlapping pseudorapidity regions, and as there may be gates placed on the CTB and ZDC information for Level-0 decisions by the trigger system, it is possible that collision events that fire the pVPD may not be later accepted by the Level-0 trigger, and *vice versa*. In order to properly interface with the STAR trigger and DAQ systems, despite these possibilities, a "Local Trigger" system for

the TOFp and pVPD digitization was implemented in NIM logic. The schematic of the TOFp/pVPD Local Trigger system is shown in Fig. 3.14 on Page 28. The DAQ software used to locally read out the resulting TOFp and pVPD data and properly transmit it to the STAR DAQ system is described in next section.

3.6.1 TOFp DAQ

The local DAQ system controls the digitization hardware and reads out the detector data, reformats the data and sends it properly to the STAR DAQ system, controls I/O modules to properly communicate with the TOFp Local Trigger and the STAR Trigger, and visualizes the raw data. It is a conventional approach based on front-end electronics that are NIM and CAMAC modules with control by a PC running the Linux operating system. An overview of the local DAQ system is shown in Figure 3.13.

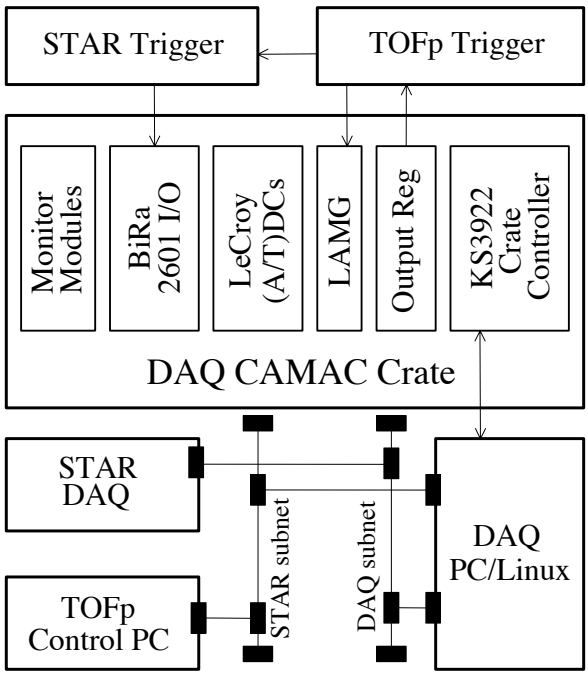

Figure 3.13: The schematic of the hardware components of the TOFp DAQ system. The arrows denote the direction of the signals or directives.

There are four LeCroy 2249A ADCs and six LeCroy 2228A TDCs in the CAMAC crate. A Kinetics Systems 3922 parallel bus crate controller communicates with a Kinetics 2915 PCI Interface in the PC's PCI bus. The local DAQ system also needs to communicate with both the local trigger system and the STAR trigger. A Bira model 2601 24-bit I/O register accepts the token and other control information from the STAR Trigger, while a Jorway 41 output register and a custom "LAMG" module handle the communication with the local trigger system. The LAMG module is a single width CAMAC module which can accept a trigger signal and generate a LAM signal on the CAMAC bus after a preset delay. The detector and cable path temperatures, as well as the read-back values of the remote threshold system, are read out using a Kinetics model 3516 32-channel scanning A/D converter. A spare ADC channel is also used as a 60 Hz clock as described in Ref. [99].

The data readout and transfer is done by the PC with a Kinetics model 2915 PCI card (the daq pc is running with a Linux 2.2 kernel, so the driver been developed at KEK [100] and JNAL for 2.0 kernel has been ported to 2.2 kernel) and two network interface cards (NIC). The function of the KS2915 is to communicate with the CAMAC crate and read out all the data on the CAMAC backplane. One of the NICs is used to communicate with the STAR DAQ system on DAQ's private subnet, while the other is used for monitoring and operator control via the general STAR subnet.

Custom software written in C performs the functions outlined in Figure 3.15. There are five programs running on the PC. To simplify the operate procedure, they are spawned by one program called TOFPMOTHER. The five programs are RUNCONTROL, GETDATA, SENDDATA, STARDAQMONITOR and LOCALDAQMONITOR. RUNCONTROL communicates with STAR DAQ, gets the DAQ command, and notifies the other programs, then returns the execute status to STAR DAQ. It also updates generic status information for the system. GETDATA reads out the data and saves it in a shared buffer (let's say the total physical RAM of the PC is 128 M, by append "mem=120M" to the kernel boot parameter will let the operating system see only the first 120 M RAM, so the rest about 8 M RAM can be used for the event buffer by a *mmap* system call to /dev/mem. The actual size is related to the hardware, for the PC share video memory with the system memory, the size will smaller, so one need to check how much actual size available before use it.), so SENDDATA can send it to the STAR DAQ. GETDATA communicates with both the STAR Trigger and the TOFp local trigger system. In case the event buffer becomes full, GETDATA will keep and hold the system busy, so the STAR Trigger won't send further trigger information to TOFp. Each time an event arrives or is sent out, GETDATA and SENDDATA update the information stored in the shared memory segments. A round-robin scheduling algorithm[8] is applied, so these programs have a higher priority than all other programs. STARDAQMONITOR sends run-time status information of the TOFp DAQ system to the STAR DAQ run-time system. LOCALDAQMONITOR sends a fraction of the raw data, typically every tenth event, to the local monitoring system. This allows the display of histograms of the raw data as it is arriving for diagnostics. The LOCALDAQMONITOR system is running on another PC in the STAR control room called the ControlPC. A local monitor server program runs as a daemon and receives the data from the local DAQ system, and saves it into histograms in a shared mapped ROOT [111] file. Another program called local monitor display displays these histograms.

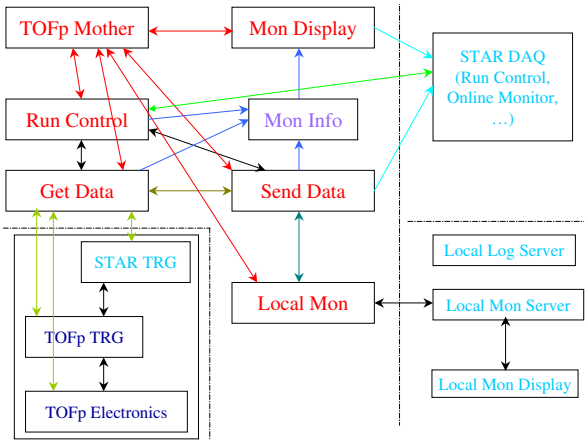

Figure 3.15: The schematic of the software components of the local TOFp DAQ system. The arrows denote the direction of the signals or directives or data transfer.

There are only one CAMAC crate for TOFp. In 2002, another TOFr tray was added in which has more readout channels. The system is upgraded with 3 CAMAC crates. The 2915 PCI card can support up to 8 CAMAC crates. The software can been easily ported to cope with this situation after modify the readout part of program GETDATA. Indeed the TOFr detector has been success running which provide a very food foundation for the barrel Time-of-Flight detector [101].

[8] *man sched_setscheduler* on Linux system

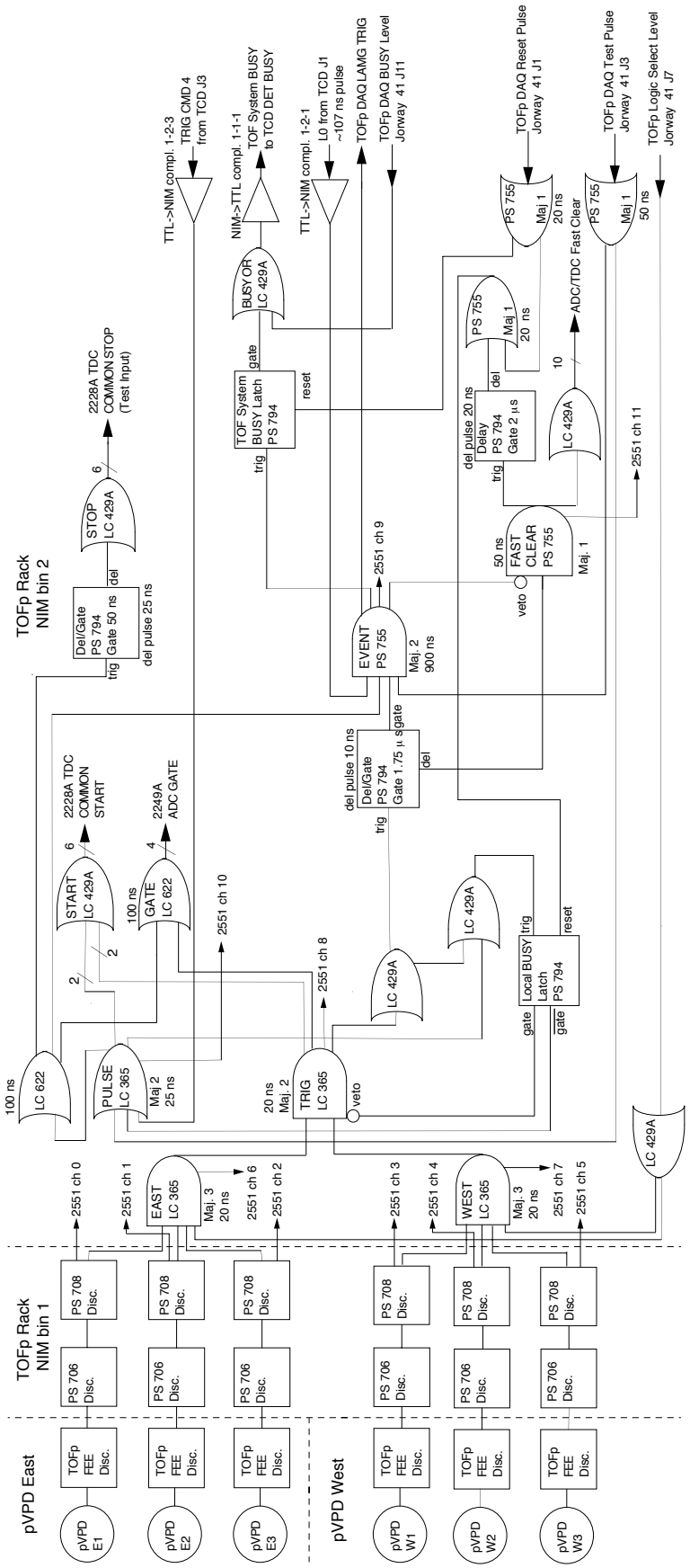

Figure 3.14: The Schematic of the TOFp/pVPD Local Trigger system.

Chapter 4

Data Analysis and Results

In this chapter, the data analysis processes and results are presented. We start from a quick view of the offline simulation and reconstruction software, then go to the analysis of proton and anti-proton, the correction to the spectra is discussed too, and finally, the results of this analysis are presented.

4.1 Offline Simulation and Reconstruction Software

Offline simulation and reconstruction software is the major component of STAR experiment. The offline simulation software will simulate the physical and electronic response of each active detector in STAR to all types of particle production processes anticipated during the development and operation of STAR. We'll discuss them in following sections. The offline reconstruction software will convert the raw input pixel data from either simulation or the real experiment into a reconstructed version of the particle production which is a list of particles corresponding to the triggered event and includes the momentum, energy, charge and/or particle identification (PID) of the individually identified tracks. By combining the simulation and reconstruction software, we can get the physical results, evaluate and visualize the results to check the adequacy and correctness, get the acceptance and efficiency tables, and do many other things. All the sub-detectors are included in the offline software. Only TPC is used in this analysis, thus we'll focus on the reconstruction and simulation processes in the TPC. Other detectors such RICH, SVT, FTPC, TOFp were included in the run too. You may find the detail of their offline software from the STAR web page. The design for the STAR offline simulation and analysis software is given in [118].

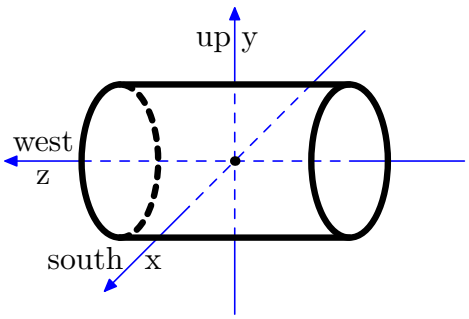

Figure 4.1: STAR Coordinate System.

Before discussing the following procedure, we first introduce the standard

STAR coordinate system [120]. As show in Fig. 4.1, it's a right-handed Cartesian system. The origin of the coordinate system is located at the center of the solenoid (iron).

4.1.1 Event Reconstruction in the TPC

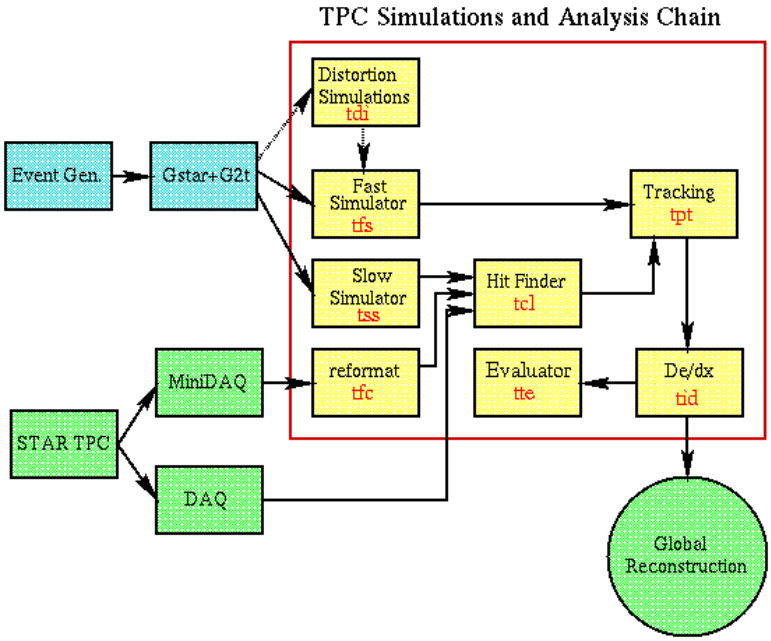

Figure 4.2: Schematic of the STAR TPC Software Chain.

TPC is the main track detector of STAR. The goal of TPC tracking software is to associate the raw space points (nearly 7 million) taken in an event to form geometrical tracks and fit the points on a track with a track model to extract information such as the particle momentum. The flow chart of different TPC offline software modules is shown in Fig. 4.2. The chain is designed to cope with both simulated data and real data. There are no differences for the reconstruction part. The software starts from the pixel information.

Cluster/Hit Finder

The cluster/hitfinder [119] is designed to extract the raw data pad-row crossing positions ("hits") for charged particles that traverse the active volume of the TPC. It is the first offline analysis (non-calibration) software that will process the TPC data. Almost all the other offline software are built on the output of cluster/hitfinder. During this stage, the local x-y positions are obtained by looking for ionization on adjacent pads rows with similar drift times, and the z position is found by looking for ionization in adjacent time bins (time buckets) on the same pad. The ionization of two crossed tracks will form a merged cluster and is divided evenly between them. This cluster is used only for tracking. Once all the local x-y and z positions are found, they will be transformed into TPC space points with the drift velocity. These space points contain the information about the hits in the STAR global coordinates and the energy deposited by the particle.

Fig. 4.3 shows a typical TPC event at hit level. During this stage, the gain corrections are applied, the channels tagged by DAQ or previous offline runs as bad, noisy or dead are removed too. The relative timing corrections between pads are also applied. It is likely that two particles will hit the padrows with very close distance. Thus, a pass is made to find single hits and multiple hits in a cluster too. The multiple hit finder may deconvolve the cluster into individual hits. Finally, the hits will be transformed into TPC space points. With drift velocity, trigger time offsets, sector geometry and electronic shaper response, the space points contain information of the position and the energy deposited by the track.

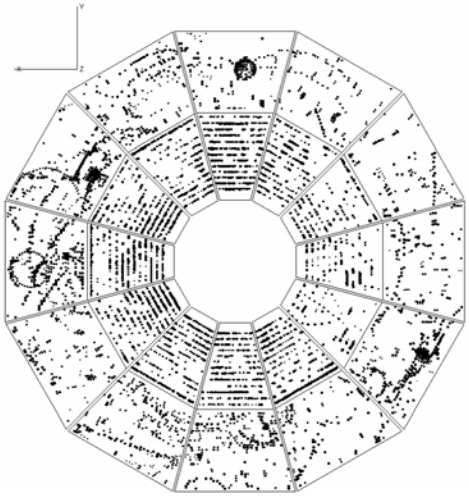

Figure 4.3: A TPC Event at hit level.

Track Finding and Global Event Reconstruction

After get all the space points information, the tracking finding algorithm is employed to reconstruct the space points into particle tracks and determine the 3-momentum.

The track model is a helix include the energy loss in the gas which causes a particle trajectory to deviate slightly from the helix [123]. Kalman Filter method [121] is used for tracking. The tracking efficiency depends on the acceptance of the detector, the electronics detection capability and the two-hit separation capability.

TPC is the main tracking detector in STAR. However, many other tracking detectors are added to the system too. It is the task of the global tracking to match the track and hit information from all the different sub-detectors.

Primary Vertex Finding

Immediately after get all the track information, it is necessary to find out the collision vertex of the event. By knowing the primary vertex we can find where a track is a primary track or a secondary track (tracks resulting from decays of primary particles, interactions with detectors, etc...), we can also refit the track with this vertex included to improve the momentum resolution. In STAR, this is done by the event vertex reconstruction package [122]. A Least Squares Method (LSM) is used.

Primary Track Fit

Once the primary vertex is found, the global tracks with the 3-dimensional distance of closest approach (*dca*) less than 3 cm are chosen for a refit by including the vertex as a additional space points. The new tracks are called *primary* tracks. This procedure increase the momentum resolution of the tracks because of the

error assigned to the primary vertex is much smaller than those associated with TPC space points.

4.1.2 Particle Identification with dE/dx

The charge collected for each hit on a track is proportional to the energy loss of the charge particle which pass through the gas in the TPC. For a particle with charge z (in units of e) and speed $\beta = v/c$ passing through a medium with density ρ, the mean energy loss it suffers can be described by the Bethe-Bloch formula:

$$\left\langle \frac{dE}{dx} \right\rangle = 2\pi N_0 r_e^2 m_e c^2 \rho \frac{Z z^2}{A\beta^2} \left[\ln \frac{2m_e\gamma^2 v^2 E_M}{I^2} - 2\beta^2 \right] \tag{4.1}$$

where N_0 is Avogadro's number, m_e is the electron mass, r_e $(= \frac{e^2}{m_e})$ is the classical electron radius, c is the speed of light, Z is the atomic number of the absorbing material, A is the atomic weight of the absorbing material, $\gamma = 1/\sqrt{1-\beta^2}$, I is the mean excitation energy, and E_M $(= 2m_e c^2\beta^2/(1-\beta^2))$ is the maximum transferable energy in a single collision [124]. From this formula, we can see that the different charge particle (different mass) with the same momentum p pass through the TPC gas can result in different energy loss. Fig. 4.4 shows the energy loss for particles in the TPC as a function of the particle momentum for both primary and secondary particles. From this figure, we can also see that as the particle energy rise, the energy loss becomes less mass dependent. Pion and kaon can be identified up to 0.75 GeV/c, proton and anti-proton can be identified up to 1.1 GeV/c.

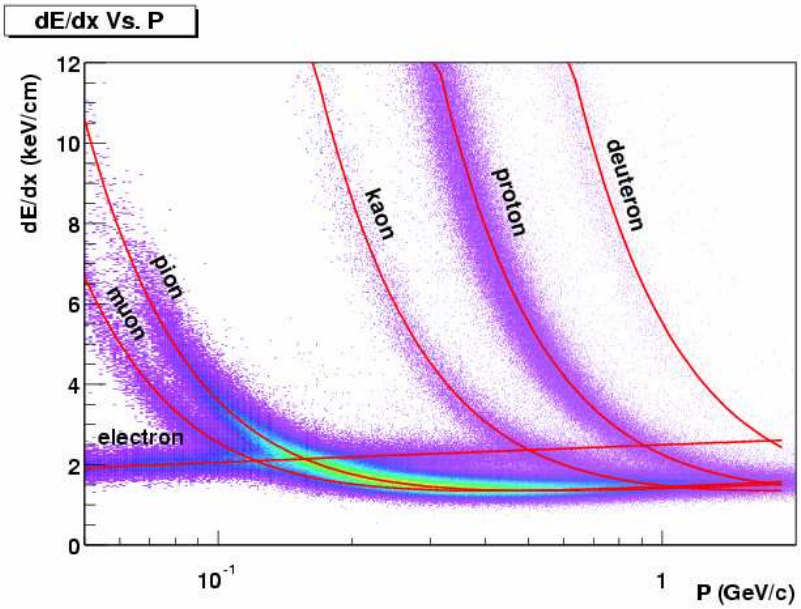

Figure 4.4: The energy loss distribution for primary and secondary particles in the STAR TPC as a function of the p_t of the primary particle. Figure from [75].

4.2 Raw Yield of Proton and Anti-Proton

In this section, the analysis procedure of raw yield of proton and anti-proton will be presented. I'll start with the event selection and centrality definition, then

discuss the cuts condition used, followed by the particle identification using energy loss in TPC, finally, the procedure of how to extract proton background is explained.

4.2.1 Centrality Definition

For this analysis, both minimum bias (minbias) data and central trigger data set taken from Au+Au collisions at 2001 are used. The collision centrality is defined by the impact parameter b (see Fig. 4.5). Smaller b corresponds to more central collisions. However, we cannot measure the impact parameter experimentally, so we must rely on some other experimental observable that correlates with the impact parameter. For this analysis, we chose the number of uncorrected charged particle (multiplicity)[1]. These are the primary tracks which were reconstructed in TPC, have at least 10 hits and pass through following cut: $dca < 3$ cm, $-0.5 < \eta < 0.5$. The events are then divided into 9 centrality bins which are defined by the percentage of the total multiplicity. Fig. 4.6 shows the multiplicity distribution with the centrality bins used in this analysis.

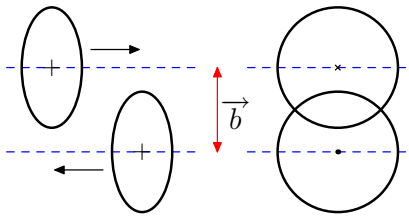

Figure 4.5: Illustration of impact parameter $\vec{b}$. Left is side view and right is end view.

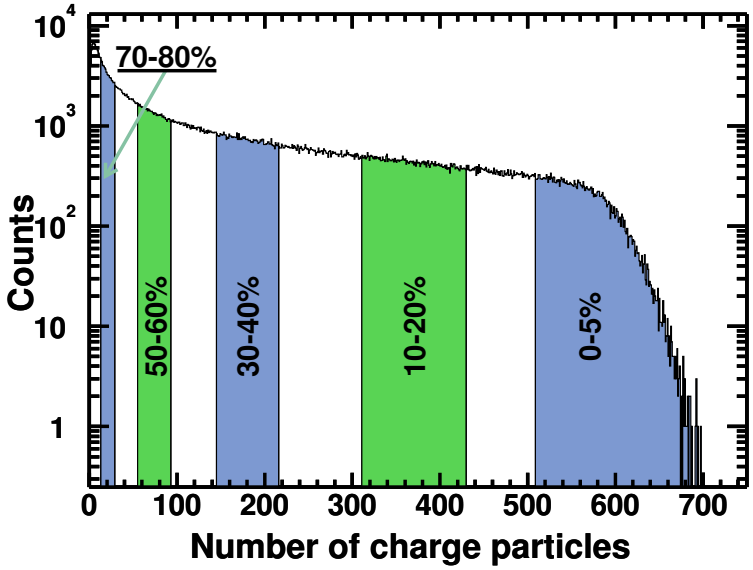

Figure 4.6: Charged multiplicity distribution for Au+Au collisions @ $\sqrt{s_{NN}} = 200$ GeV. The 9 centrality bins used in this analysis are illustrated too.

Let's image during the collision process, each of the nucleons in the nuclei that participate in the collision process produces (on average) a certain number of particles, then we can calculate the average number of nucleons that participants in the collision ($\langle N_{part} \rangle$) at a given impact parameter b with a geometrical model (Glauber Model). Thus, there is a statistical mapping of $\langle N_{charge} \rangle \rightarrow \langle N_{part} \rangle \rightarrow \langle b \rangle$ [125, 126]. The particle productions are found to be proportional to the number of elementary nucleon-nucleon collisions (number of binary collisions: N_{coll}), especially for large

[1] http://www.star.bnl.gov/protected/common/common2002/centrality/

Centrality	(%)	N_{charge} (>)	$dN_{ch}/d\eta$	N_{part}	N_{bin}	$\langle b \rangle$ (fm)
1	70−80	14	22.	$14.0^{+4.0}_{-5.2}$	$12.3^{+4.8}_{-5.1}$	$12.9^{+0.6}_{-0.6}$
2	60−70	30	45.	$26.9^{+6.6}_{-5.5}$	$29.1^{+9.6}_{-8.6}$	$12.0^{+0.5}_{-0.6}$
3	50−60	56	78.	$47.3^{+8.1}_{-7.5}$	$62.4^{+16.3}_{-15.7}$	$11.1^{+0.5}_{-0.5}$
4	40−50	94	126.	$76.2^{+9.0}_{-9.1}$	$120.6^{+25.1}_{-24.5}$	$10.0^{+0.5}_{-0.4}$
5	30−40	146	195.	$114.5^{+10.7}_{-8.6}$	$214.3^{+36.2}_{-33.2}$	$8.8^{+0.4}_{-0.4}$
6	20−30	217	287.	$165.7^{+10.0}_{-8.3}$	$358.4^{+46.3}_{-43.6}$	$7.5^{+0.3}_{-0.3}$
7	10−20	312	421.	$233.6^{+7.4}_{-8.4}$	$575.8^{+54.5}_{-58.1}$	$5.8^{+0.3}_{-0.2}$
8	5−10	431	558.	$298.3^{+5.2}_{-7.1}$	$804.6^{+65.4}_{-64.0}$	$4.1^{+0.2}_{-0.2}$
9	0−5	510	691.	$351.5^{+3.4}_{-3.8}$	$1020.3^{+73.2}_{-68.0}$	$2.2^{+0.2}_{-0.2}$

Table 4.1: Listed for $\sqrt{s_{NN}} = 200$ GeV for each Centrality bin are the rage of the % most central of the hadronic cross section, $dN_{ch}/d\eta$, the estimated mean number of participants, the estimated number of binary collisions, and the estimated mean impact parameter. Data from [126].

momentum transfer (hard) processes. Table 4.1 shows the corresponding value for these parameters in different centrality.

4.2.2 Event Selection

In order to have a good quality control to the analysis results presented here, several cut conditions were applied to this analysis. These include both event-wise variables and track related variables.

Primary Vertex

Normally, collisions will take place over a wide range of values along the *z-axis*. However, if the collisions take place around the center of TPC $(x = y = z = 0)$, most of the particles will travel the greatest distance inside the TPC, the event shape will be symmetric and have maximum coverage on pseudo-rapidity range $|\eta| < 1$. The reason is that TPC is a symmetric detector around the central. For $\sqrt{s_{NN}} = 200$ GeV Au+Au run in 2001, a vertex cut was already applied to some of the trigger type, considerate that the supporting structure of the SVT starting at ± 25 cm, we choose a primary vertex cut of $|Z| < 25$ cm. Also, $|X| < 3.5$ cm and $|Y| < 3.5$ cm were applied to the data.

Track Selection

For this analysis, we require there are at least 23 hits out of maximum 45 hits in the TPC for each track used. Also, we require that all the primary tracks pass

within 3 cm of the primary vertex, *i.e.*, $dca < 3$ cm. Other kinds of *dca* cut was applied to extract the systematic error.

4.2.3 Extract the Raw Yield of Proton and Anti-proton with Energy Loss in TPC

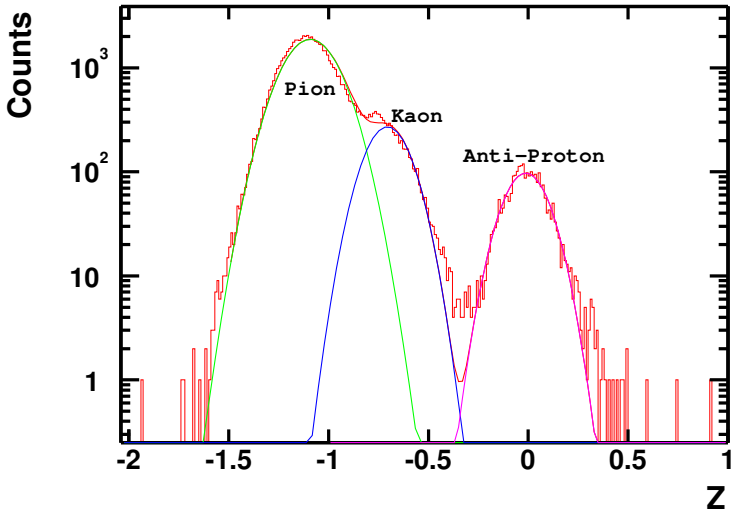

Figure 4.7: Z distribution for a, 50 MeV wide, p_t and, 0.1 unit wide, rapidity bin. Three particle species are labelled. Each peak can be fit with a Gaussian function. The plot is fit with a 3-Gaussian function.

Z Position Correction

As has been discussed before, the energy loss of charge particle when pass through TPC can be used for particle identification. However, it's not possible to do this identification on a track-by-track basis in the full p_t range. As can be seen in Fig. 4.4, different particles have similar energy loss around $p_t \approx 1$ GeV. We use a fitting process over many events in the same class to extract the yield of the proton and anti-proton. We construct a quantity $Z = \log\left(\left[\frac{dE}{dx}\right]_{\rm exp} / \left[\frac{dE}{dx}\right]_{BB(proton\ mass)}\right)$, where $\left[\frac{dE}{dx}\right]_{BB(proton\ mass)}$ is the expected ionization for proton and anti-proton from the Bethe-Bloch formula. For a pure sample of proton, this quantity should be well described by a Gaussian centered at zero. However, there are many different particle species such as pions, kaons etc in the sample. These particles will be seen as Gaussian shapes offset from zero. Fig. 4.7 shows an example Z distribution for one transverse momentum and rapidity bin. So we can use a multi-Gaussian fit to extract the raw yield of proton and anti-proton.

The statements above are based on that the Bethe-Bloch formula we used can describe the energy loss in the experiment well, *i.e.*, the parameters are perfect. However, this is unlikely to happen, reflect on the results of Z distribution, we see the mean value of the particle to be identified is not zero, *i.e.*, the central position of Gaussian shape is shifted away from zero. Fig. 4.8 shows such shift for pion, we can see the shift is dependent on the number of fit points too. A parabola fit is employed to fit this dependence, then the parameters from the fit are applied into

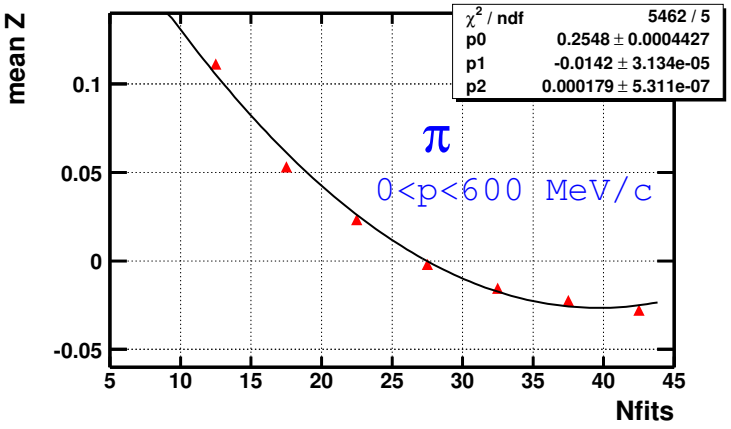

Figure 4.8: The shift away from zero vs number of fit points for pion Z distribution, Line represents parabola fit.

the corrected Z variable formula:

$$Z = \log\left(\frac{\left[\frac{dE}{dx}\right]_{exp}}{\left[\frac{dE}{dx}\right]_{BB(proton\ mass)} * (a_0 + a_1 * fitpts + a_2 * fitpts^2)}\right) \tag{4.2}$$

where a_0, a_1, a_2 are parameters from the parabola fit, $fitpts$ are the number of fit points of the track.

Energy Loss Correction

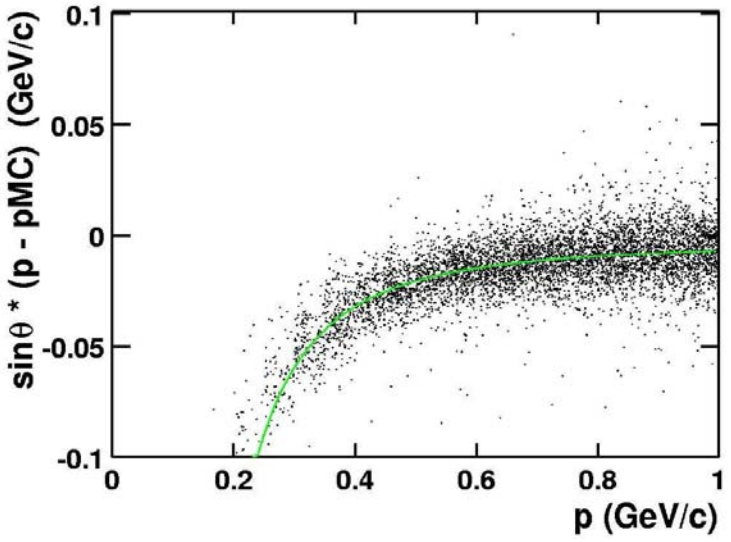

Figure 4.9: Difference (times sine of the dip angle θ) of the reconstructed momentum (p) and the initial momentum (p_{MC}) due to energy loss in detector materials, versus momentum (p). Determined using a GEANT simulation.

When a particle traverses through the detector material, it must have energy loss. Due to this effect, the momentum recorded by the detector is less than the initial momentum when the particle freeze-out. A GEANT [102] simulation with Anti-protons and protons is done to study this effect. The momentum difference (Δp) between the reconstructed momentum (p) and the initial momentum (p_{MC}) due to energy loss is shown in Fig. 4.9. The dependence of the momentum difference is fit by

$$\Delta p = p - p_{MC} = a/\beta^c \cdot \frac{1}{\sin\theta} \tag{4.3}$$

where β is the relativistic velocity of (anti-)protons, θ is the dip angle between beam axis and particle trajectory. The fit parameter are $\alpha = -0.0032888$ and $c = 2.43938$. The energy loss correction is applied to the reconstructed global tracks used in this analysis.

Multi-Gaussian Fit

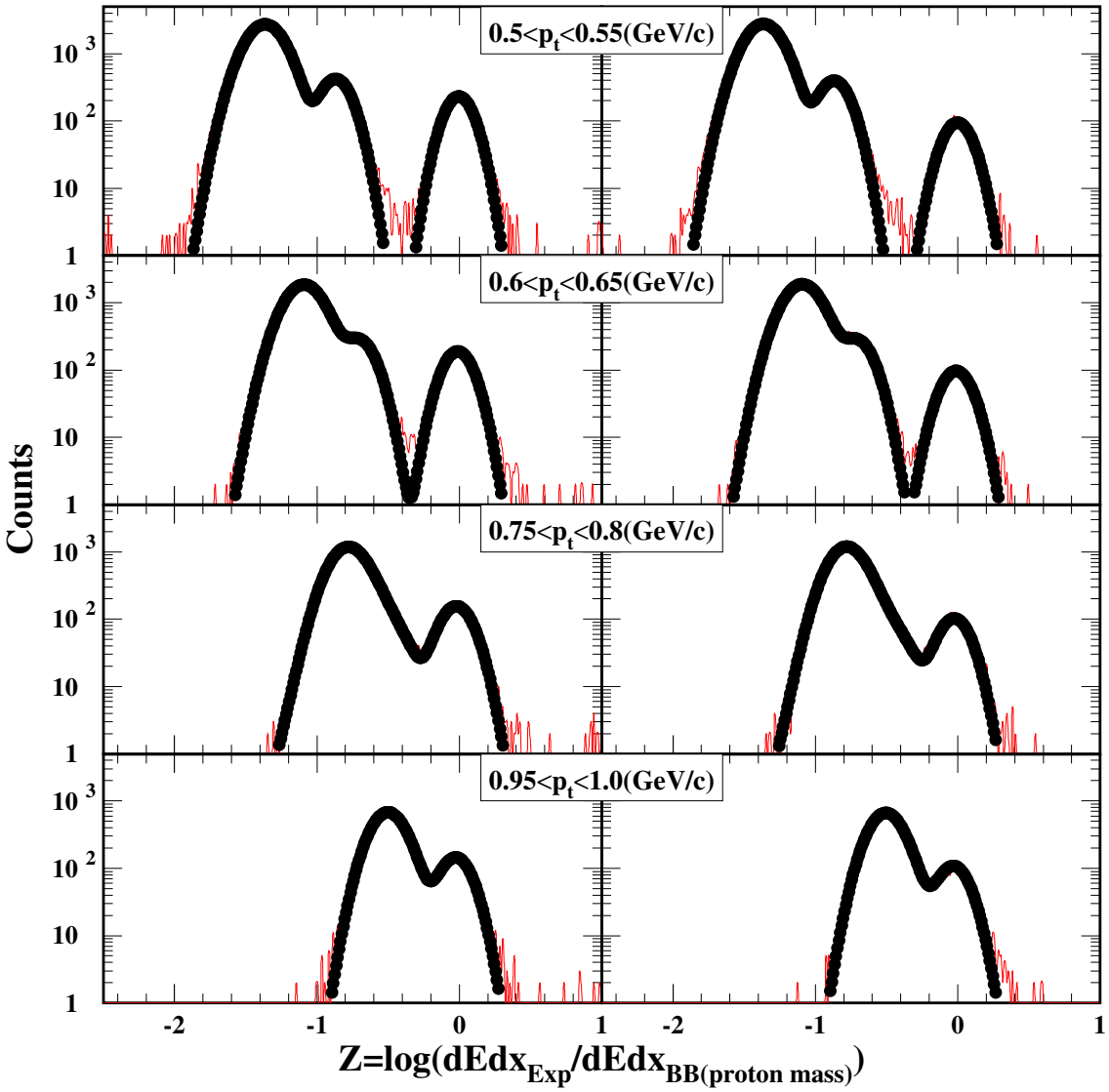

Figure 4.10: Middle-rapidity particle yields as a function of $Z = \log\{\left[\frac{dE}{dx}\right]_{\rm exp} / \left[\frac{dE}{dx}\right]_{BB(proton\ mass)}\}$, left plots and right plots are for protons and anti-protons, respectively. Black points are the multi-Gaussian fits to the measured distributions.

For this analysis, we have 9 centrality bins. Each centrality bin is further divided into 50 MeV/c per transverse momentum from 0.4 GeV/c to 1.05 GeV/c and 0.1 unit wide per rapidity bin from -1.0 to 1.0. Thus we have a Z distribution for each bin. A multi-Gaussian fit was applied to this distribution then. From Fig. 4.4

Particle	Name	Parameter	Range	Initial Value
	Area	$par[0]$	$1, 10^4$	n/a
Pion	Mean	$par[1]$	$dEdxPion \pm 0.1$	$dEdxPion$
	Width	$par[2]$	$0.05, 0.2$	n/a
	Area	$par[6]$	$1, 10^4$	n/a
Proton	Mean	$par[7]$	$-0.08, 0.05$	0
	Width	$par[8]$	$0.05, 0.1$	n/a

Table 4.2: Limit of Initial Fit Parameter for Pion and Proton, where $dEdxPion = \left[\frac{dE}{dx}\right]_{BB(pion\ mass)} / \left[\frac{dE}{dx}\right]_{BB(proton\ mass)}$, n/a means no initialization

	Range	Initial Value		Range	Initial Value
[0]	$1, 10^4$	$par[0]/2$	[0]	$1, 10^4$	$par[0]/2$
[1]	$dEdxPion \pm 0.1$	$par[1]$	[1]	$dEdxPion \pm 0.1$	$par[1]$
[2]	$par[2] \pm 0.1$	$par[2]$	[2]	see [1]	$par[2]$
[3]	$1, par[0]$	$par[0]/2$	[3]	$1, 10^4$	$par[0]/2$
[4]	see [2]	$dEdxKaon$	[4]	see [3]	$dEdxKaon$
[5]	$par[2] \pm 0.1$	$par[2]$	[5]	$1, 10^4$	$par[6]$
[6]	$1, 10^4$	$par[6]$	[6]	± 0.05	$par[7]$
[7]	$-0.08, 0.05$	$par[7]$	[7]	$0.06, 0.1$	$par[8]$
[8]	$0.06, 0.15$	$par[8]$			

[1] $0.11 - 0.12$ for top 2 centrality bins (more central collisions), $0.1 - 0.12$ for other centrality bins

[2] $par[1], dEdxKaon+0.1$

[3] $dEdxKaon, dEdxKaon+0.1$

Table 4.3: Limit of Fit Parameter for multi-Gaussian fit, left: $p_t < 600$ MeV/c, right: $p_t > 600$ MeV/c, $dEdxPion = \left[\frac{dE}{dx}\right]_{BB(kaon\ mass)} / \left[\frac{dE}{dx}\right]_{BB(proton\ mass)}$

we can see as the momentum increases, the energy loss becomes less sensitive to the particle species. Reflecting on the Z plots, the peak of pion, kaon and proton will merge. See Fig. 4.10. So we need to apply different limits on the fit parameter. We can also see for higher momentum bin, it's hard to tell the peak position and width of pion and kaon, so we let pion and kaon have the same width for the multi-Gaussian function when $p_t > 600$ MeV/c. In brief, the multi-Gaussian functions we

used for fit are:

$$\begin{aligned}
&\frac{[0]}{[2]\times\sqrt{2\pi}}e^{\frac{-(x-[1])^2}{2\,[2]^2}}+\frac{[3]}{[5]\times\sqrt{2\pi}}e^{\frac{-(x-[4])^2}{2\,[5]^2}}+\frac{[6]}{[8]\times\sqrt{2\pi}}e^{\frac{-(x-[7])^2}{2\,[8]^2}} \quad for\ p_t<600\ \mathrm{MeV}/c\\
&\frac{[0]}{[2]\times\sqrt{2\pi}}e^{\frac{-(x-[1])^2}{2\,[2]^2}}+\frac{[3]}{[2]\times\sqrt{2\pi}}e^{\frac{-(x-[4])^2}{2\,[2]^2}}+\frac{[5]}{[7]\times\sqrt{2\pi}}e^{\frac{-(x-[6])^2}{2\,[7]^2}} \quad for\ p_t>600\ \mathrm{MeV}/c
\end{aligned} \tag{4.4}$$

where $[0]$, $[1]$, $\cdots$ are the parameters to be fit, the first Gaussian denotes Z distribution for pion and the second for kaon, the third for proton. Before the multi-Gaussian fit, we also apply two Gaussian fits (with equation 4.5,

$$\frac{[0]}{[2]\times\sqrt{2\pi}}e^{\frac{-(x-[1])^2}{2[2]^2}} \tag{4.5}$$

where [0],[1],[2] denotes the area, mean and width of Gaussian function) to the spectra around the expected Z value for pion and proton to get a rough estimate for the initial value of multi-Gaussian fit. These initial values were then applied to the multi-Gaussian fit. For discussion purpose, we refer these initial values for pion as $par[0], par[1], par[2]$ and for proton as $par[6], par[7], par[8]$. The limits of the parameters for this initial fit are listed in Table 4.2.

Finally, all the limits applied to the multi-Gaussian fits are listed in Table 4.3. We can see the major concern for the limit is the mean and width of the Gaussian function. For some particular bins (most in high pt region), the fit will be sensitive to the limit used and will fail. Fine-tuning is needed in this case.

Fig. 4.10 shows the multi-Gaussian fit results to the Z distributions. The area of the third Gaussian function in equation 4.4 is the raw yield of (anti-)protons.

4.2.4 Extract the proton background

Before the particles produced in a collision are detected by TPC, they must traverse the beam pipe and different kinds of detector material, they will have hadronic interactions with beam pipe and the detector materials, thus produce secondary particles (including secondary protons). Primary protons have a small *dca* since they are produced from the event vertex, while this is not true for the secondary protons since they are not produced at the main event vertex. The *dca* distribution of proton and anti-proton for different p_t bin is shown in Fig. 4.11. The distribution is peaked at small *dca* and has a flat tail from secondary production.

Since the background shape of the *dca* distribution at small *dca* (≤ 3 cm) is not known, a Monte Carlo simulation (GEANT) was employed by using the particles generated by both HIJING and RQMD models as input. An empirical form was found for the background:

$$background(dca) \propto \left(1+\exp\left(\frac{-dca}{a}\right)\right)^{-1} \tag{4.6}$$

where a is a parameter to be determined which is both momentum and rapidity dependent. We have the same binning when extract the raw yield of (anti-)proton. The *dca* distributions of proton and anti-proton for each bin are plotted. We can

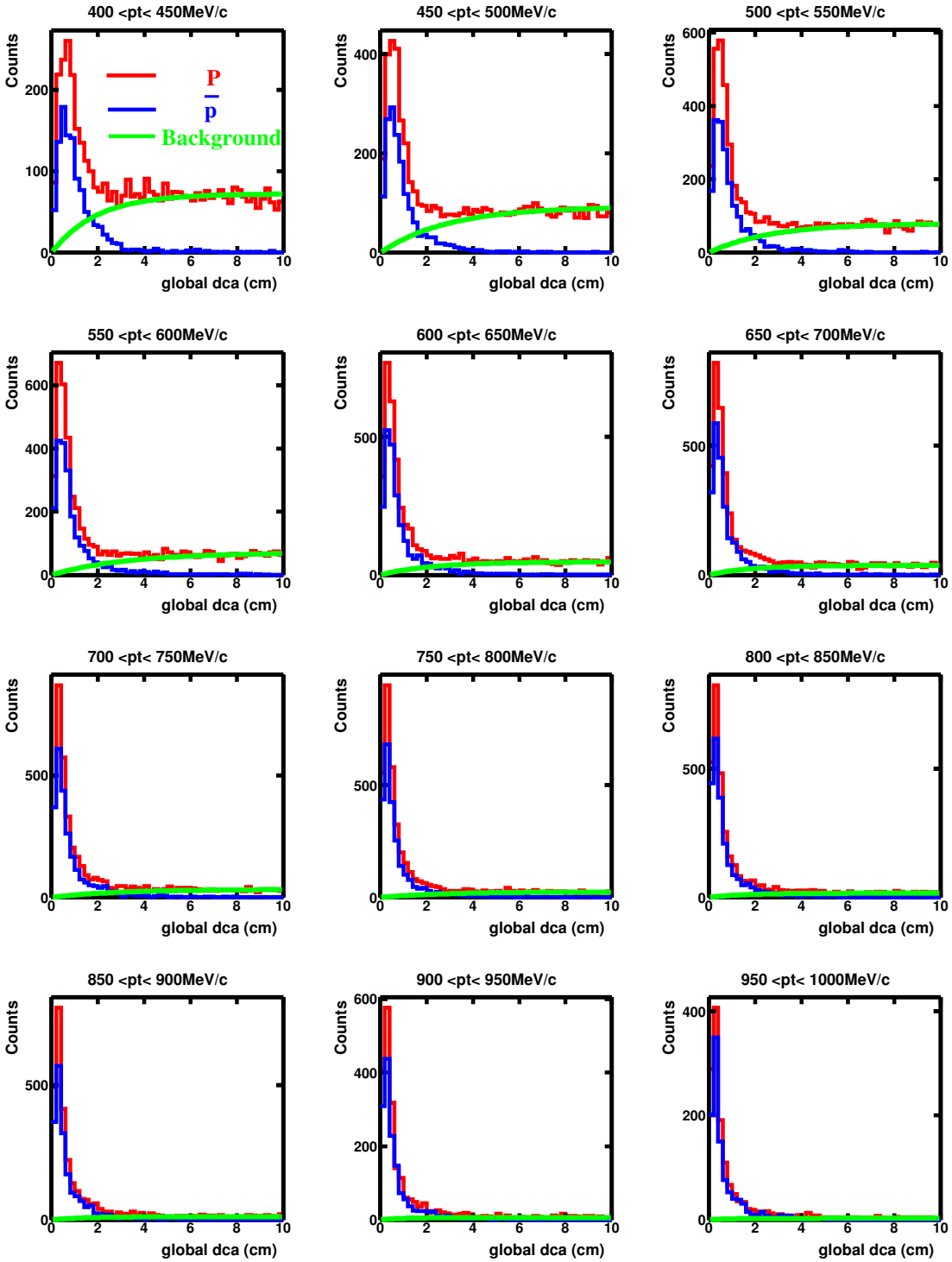

Figure 4.11: Proton and anti-proton *dca* distributions for different p_t bin, the background (line start from the origin) is strongly dependent on the transverse momentum.

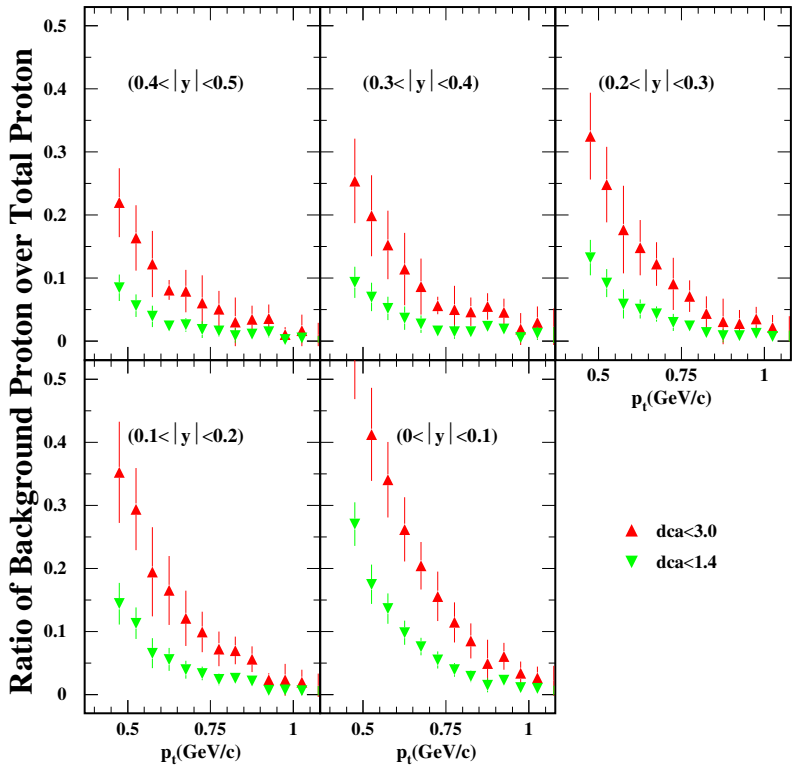

Figure 4.12: The ratio of background proton over total proton vs p_t for different rapidity bin.

see from equation 4.6, there is a scale factor which is dependent on the *dca* distribution of the non-background proton. We assume the non-background proton and anti-proton have similar *dca* distribution, then fit the proton *dca* distribution by using

$$P(dca) = N_1 * \left(1 + \exp\left(\frac{-dca}{a}\right)\right)^{-1} + N_0 * \bar{P}(dca) \tag{4.7}$$

where N_1 and N_0 are scale factors. The background protons (line start from the origin) distributions, shown in Fig. 4.11, are gotten from above fit procedure. We can also see that a large amount of background protons are concentrated at low p_t region. This can be seen from Fig. 4.12 where the ratios of background protons over total protons vs p_t are shown at different rapidity bins.

The net-proton then was obtained by multiplying the total proton a factor $\big(1-ratio(y,p_t)\big)$.

4.3 Efficiency Correction

If the detector and the reconstruction software are perfect, *i.e.*, the detector has full acceptance and can record everything correctly, the software can reconstruct the 3D image from the hit point information with 100% accuracy, the analysis is done with the procedures in previous sections. However, nothing can be perfect. First, the detector have no full acceptance, *i.e.*, some of the particles may hit the dead region (such as the support structure, ...) of the detector, thus can't be detected. Second, the particle will suffer energy loss when travel through the detector or annihilate (such as anti-proton will annihilate with proton in the detector

material or beam pipe). And at last, it's not possible for the software to reconstruct the full 3 dimensional image of the event correctly from the hit point information.

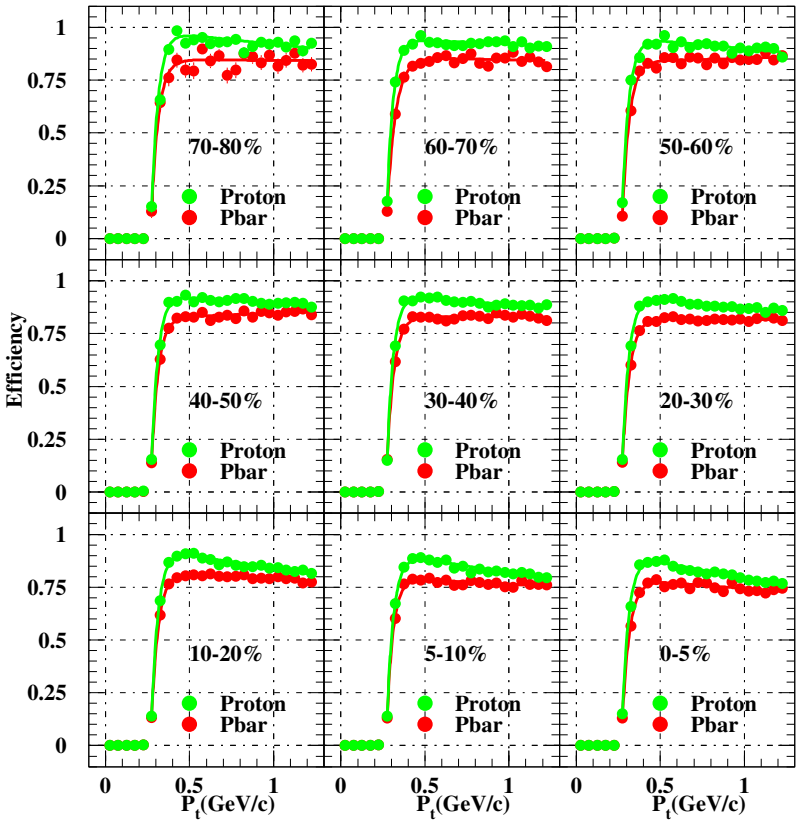

Figure 4.13: Efficiencies for protons and anti-protons as a function of transverse momentum from the 9 centrality bins used in this analysis. Line represent the fit to the data points.

So, in order to get the corrected yield of proton and anti-proton, it's necessary to include the correction of these factors. They are determined by a procedure called *embedding*. The idea is to take a real event and embed into the raw data file the signal from a few simulated tracks at the level of ADC counts. The simulated signal is obtained via a GEANT Monte Carlo simulation of the detector response as been detailedly described in [125]. The acceptance, energy loss, particle (anti-proton, for this analysis) annihilation etc. are all be simulated during this process. The final simulated ADC signal is then merged into the raw data from the real event and then processed by the STAR reconstruction software chain. Since we have the full information of the embed tracks, we can then associate the reconstructed tracks to the corresponding Monte Carlo track. This association is done at the hit level.

The efficiency then can be obtained by comparing the reconstructed Monte Carlo tracks to the embedded Monte Carlo tracks. Fig. 4.13 shows the transverse momentum dependence of efficiency for the most central and peripheral collisions. For $p_t > 400$ MeV/c, the efficiency tends to be a constant. We use function

$$Effi(p_t) = (a_0 - a_1 \times p_t) \times \left(1 - exp\left(-\frac{p_t - a_2}{a_3}\right)\right) \tag{4.8}$$

to fit the data points where a_0, a_1, a_2, a_3 are the parameters. The results from this function are used for the correction in this analysis to remove unnecessary fluctuations.

4.4 Proton and Anti-Proton yields

Now we can calculate the proton and anti-proton yields with following equations:

$$\begin{aligned} Yield_{\bar{p}}(y,p_t) &= \frac{RawYield_{\bar{p}}(y,p_t)}{Effi(y,p_t) * N_{Event}} \\ Yield_{p}(y,p_t) &= \frac{RawYield_{p}(y,p_t) * \big(1 - RatioOfBackground(y,p_t)\big)}{Effi(y,p_t) * N_{Event}} \end{aligned} \tag{4.9}$$

where N_{Event} is the number of events.

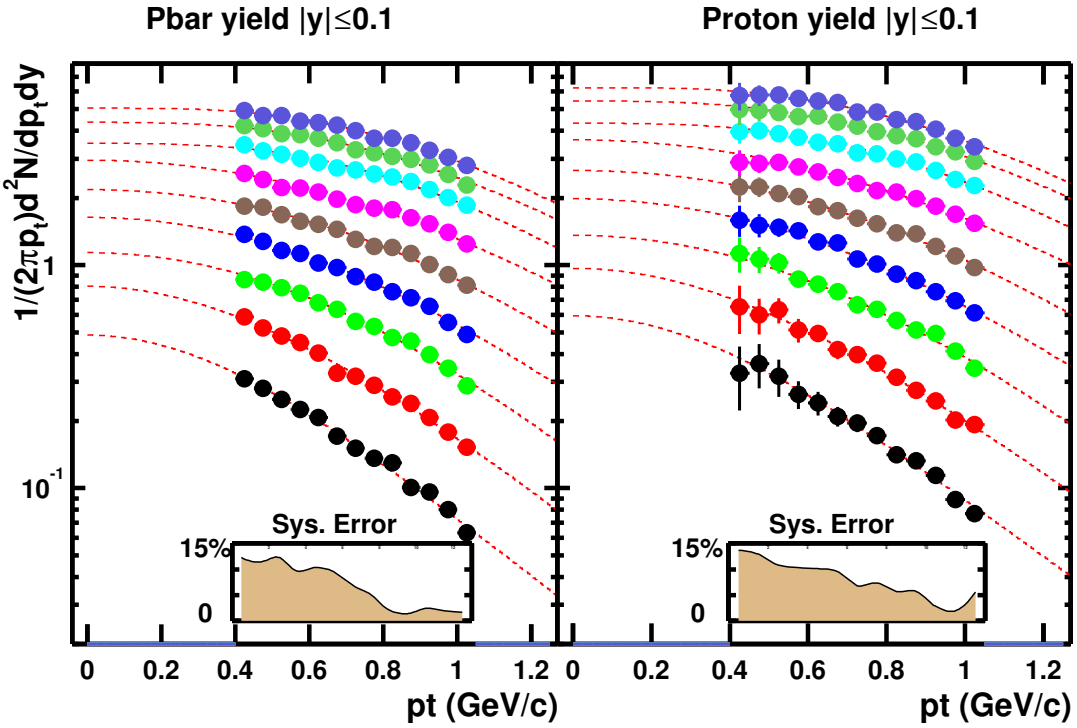

Figure 4.14: Mid-rapidity ($|y| \leq 0.1$) proton (right) and anti-proton (left) transverse momentum distributions for 9 centrality bins. From bottom to top, the centrality increase. Inner histograms are the systematic errors for the most central collision. Dashed line represent the thermal fit results.

4.4.1 Transverse Momentum Distribution

The invariant yields $d^2N/(2\pi p_t\, dp_t\, dy)$ (see App. B.4) of proton and anti-proton are shown in Fig. 4.14. The plots are arranged in the way that from bottom to top, the collision centrality increases: the top and bottom distributions correspond to top 5% and $(70-80)\%$ of the measured cross section, respectively. It is evident that for both proton (right panel) and anti-proton (left panel) distributions become more

concave from peripheral to central collisions indicating an increase in transverse radial flow. We'll come back to this issue in chapter 6.

STAR has published the spectra of π/K/P in Au + Au and pp collisions on Phys. Rev. Lett. [129]. We did a comparison by dividing our results by the PRL results, see Fig. 4.15. We can see our results are consistent with the published results within 10% errors.

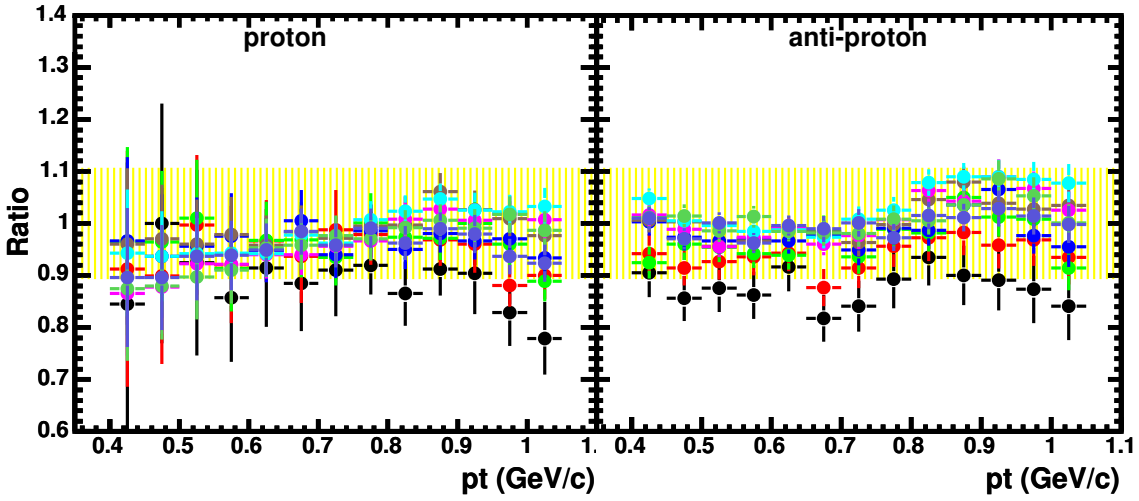

Figure 4.15: Ratio of invariance yield compare to STAR published results in [129]. Our results are consistent with the published results. The different colors denote different centrality bin.

4.4.2 Systematic Uncertainty

The bin to bin systematic uncertainties on the spectra are estimated by varying the event and track selection and analysis cuts. The estimated uncertainties are less than 15%. An additional systematic error on the proton spectra due to background subtraction is estimated to 5% at low p_t and negligible at high p_t [128]. The two inner histograms in Fig. 4.14 show the systematic errors for the most central collisions.

Chapter 5

RQMD Simulation and Results

The interactions between nucleus nucleus collisions are complex processes that involve strong and electro-weak phenomena. Although we have QCD, however, "knowing the equation is not the same as having the solutions" [103]. By employ the effective theory such as perturbative QCD and electro-weak theory, we can describe some exotic parts of the processes such as the production of high p_t jets or W, Z particles involving a large mass scale. However, the bulk of the event structure is non-perturbative in nature and cannot yet be calculated from the first principles. Thus, we have to seek for help from phenomenological models, such as the string model. The Monte Carlo implementations of such models are particularly useful for us to test various theoretical ideas. They are also invaluable to the implementations of an actual experiments from the initial design (help choose detector material, ...) to the final data analysis (comparison between the experiment and Monte Carlo results).

There are many good Monte Carlo event generators available for relativistic heavy ion collisions, such as HIJING [105], RQMD [71], UrQMD [106], AMPT [107], EPOS (formerly NEXUS) [108], etc. Each of them can describe part of the experiment results well and help us to understand the underly mechanism of the collision. For a review, see Ref. [109]. In this chapter, I will focus on the RQMD model.

5.1 RQMD Introduction

Relativistic Quantum Molecular Dynamics (RQMD) is a semiclassical microscopic model which combines classical propagation with stochastic interactions. Within the framework of RQMD, a typical heavy ion collision may be schematically divided into three stages, $i.e.$pre-hadronic stage, hadronic pre-equilibrium stage and the stage from hadronic kinetic equilibrium to freeze-out. The pre-hadronic stage is determined by the initial excitation and fragmentation of color strings and ropes. This stage lasts about 1.5 fm/c and the effective transverse pressure is rather soft. During the late hadronic stage, the hadronic system reaches local kinetic equilibrium followed by a break-down of equilibrium due to dilution of the hadronic gas and finite size of the system [110, 115]. A more detail description of

the model can be found at Ref. [71]. RQMD is not a partonic-based model. However, it's believed that there are partonic interactions at RHIC energy. The reason we select this hadronic-based model is to study only the effects of the hadronic processes which will show the difference to partonic processes. We use RQMD version 2.4 in our analysis.

5.2 Analysis of RQMD Data

The raw output of RQMD is a text-based file. In this file, each event is recorded by some event-wise variables following with each particle's PID, charge, 4-vector, 4-momentum, mass etc. in this event. Several events are stored in one file orderly. The first procedure to analysis the RQMD data is to read this file. However, sometimes we only need to read the selected (not all) variables for each event. This is not possible with this text-based file because of no pointer in this file to locate the variables. ROOT [111] based file has pointer. It provides a TTree class which can be used to organize the events into a tree-like structure. One can access only the interested data members. Also, reading the root-based file is more convenient and faster than reading the text-based file. Programs[1] have been developed for this purpose. This idea (programs) can be easily ported to other Monte-Carlo event generators (depends on the output is a text based file).

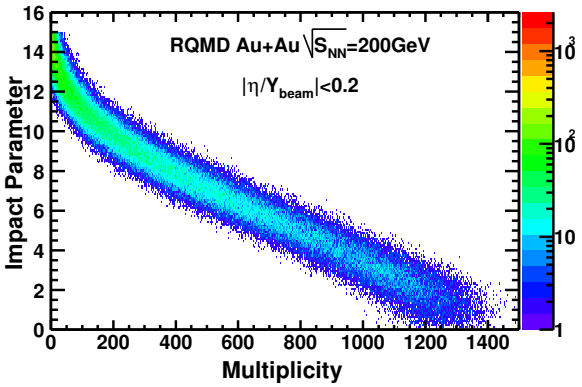

Figure 5.1: Impact parameter vs. charged particle $(\bar{p}, K^+, K^-, \pi^+, \pi^-)$ multiplicity in $|\eta/Y_{beam}| < 0.2$.

The impact parameter in a Monte Carlo event generator is known. In experiment, we're using the charged particle multiplicity as an estimate of the impact parameter since there are no ways to measure it. Fig. 5.1 shows the scatter plot of impact parameter vs. multiplicity in $|\eta/Y_{beam}| < 0.2$. An approximate linear relation exists between them. This relation also proves that the method we define the centrality with multiplicity in experiment is reasonable. In the analysis, we use the same method in the analysis of RQMD data. The centrality definition is same as in experiment, *i.e.*, we divide the multiplicity by top 0-5%, 5-10%, 10-20%, 20-30%, 30-40%, 40-50%, 50-60%, 60-70%, 70-80%, 80-100%, corresponding to total 10 centrality bins. Top 0-5% is the most central collisions.

In this analysis, we've generated several data sets for different CMS energy($\sqrt{s_{NN}}$ =): 5 GeV, 10 GeV, 20 GeV, 60 GeV, 130 GeV, 200 GeV. In order

[1] Contact me if interested.

to study the effect of rescattering, events with both rescattering on and off are generated for each energy.

5.3 Particle Spectra

Fig. 5.2 shows the mid-rapidity ($|y| < 1.0$) invariant cross section distribution for charged pions, kaons and protons as a function of transverse mass for the most central Au + Au collisions at $\sqrt{s_{NN}} = 200$ GeV. As for the case of without rescatterings, the invariant cross sections for different particles have similar shapes. This behavior is often called "m_t *scaling*" [27]. Please note, the original meaning of m_t scaling is that identified particle spectra can be described by a "universal" parameterization of the form shown in Eq. 5.1:

$$E\frac{d\sigma}{d^3p} = A\frac{e^{-m_t/T}}{m_t^{\lambda}} \tag{5.1}$$

Here the spectra of different particles have been scaled by arbitrary factors to achieve the best overlap. However, for collision with rescattering on, the scaling is broken! This is a clear evidence for collective transverse expansion.

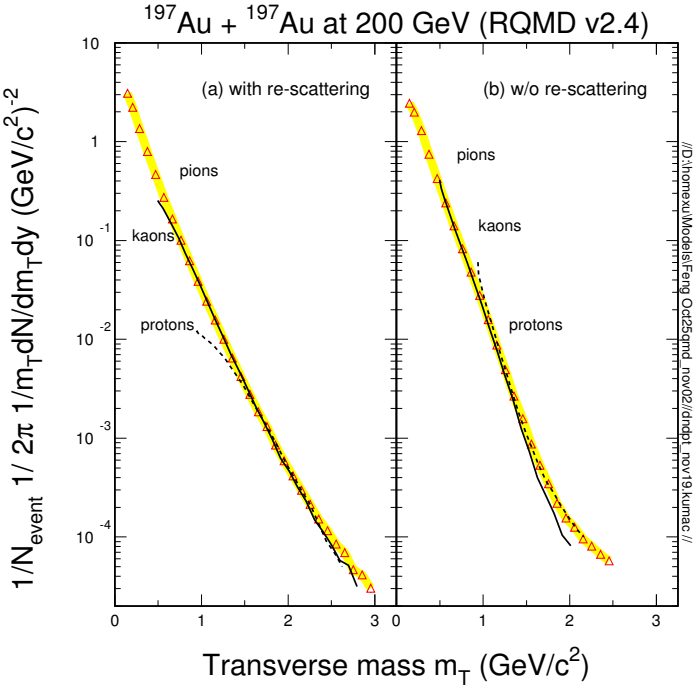

Figure 5.2: Invariant cross section of charged pions, kaons and protons as a function of transverse mass m_t for the most central Au + Au collisions at $\sqrt{s_{NN}} = 200$ GeV with RQMD model. Data are extracted from mid-rapidity only $|y| < 1.0$. Plots (a) and (b), respectively, represent results with and without rescatterings. The normalization of the distributions is arbitrary.

More clear evidence can be seen from the mass dependence of the mean transverse momentum $\langle p_t \rangle$. Fig. 5.3 shows the mid-rapidity mean p_t of charged pions, charged kaons and protons as a function of collision centrality for Au + Au collisions at $\sqrt{s_{NN}} = 200$ GeV. Data from the PHENIX Collaboration [113] are given by the symbols and RQMD results are shown as hatched bands. With increasing centrality the values of $\langle p_t \rangle$ increase and the difference between particles also increases, indicating the development of stronger collective motion in more central collisions. The RQMD model reproduces this trend although it underestimates the

absolute values for kaons throughout the whole centrality range. Again, switching off rescattering among produced particles in RQMD results in flat distributions of $\langle p_t \rangle$ as a function of centrality for pions and kaons. The variation for (anti-)protons is less than 10%. All values correspond to the most peripheral collisions, *i.e.*, $\langle p_t \rangle \approx 0.38,\ 0.47,\ 0.58$ GeV/c for charged pions, charged kaons, and (anti-)protons, respectively. These results demonstrate the importance of rescattering in high energy nuclear collisions. The RQMD model does not include partonic degrees of freedom. However, at RHIC energies the rescattering needed to describe the $\langle p_t \rangle$ and ratios of particles might occur at an earlier stage. The fact that RQMD underpredicts [44, 45] the value of $\langle v_2 \rangle$ suggests that interactions among partons at the early stage of the collision are important at RHIC.

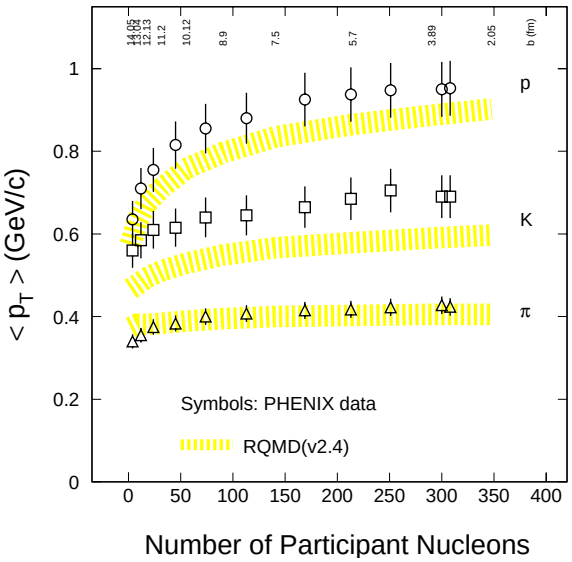

Figure 5.3: Midrapidity mean transverse momentum $\langle p_t \rangle$ of charged pions, charged kaons and protons vs collision centrality for Au + Au collisions at $\sqrt{s_{NN}} = 200$ GeV. The symbol shows data from the PHENIX collaboration [113] ($|y| \leq 0.35$) and the errors are statistical only. The dashed bands represent the results from RQMD ($|y| \leq 0.5$). The top part of the figure list the values of impact parameters from the model.

As shown in right of Fig. 2.8, a new observations at the RHIC is that the mid-rapidity yields of protons are approaching or are equal to that of negatively charged pions at moderately high transverse momentum $p_t \sim 2 - 3$ GeV/c [131]. This observation has been interpreted as the result of either baryon junction [46] or parton coalescence [51, 52]. In the former case, the novel mechanism of baryon transport, the existence of topological gluon field configurations in high energy collisions, is invoked. The junction model predicts long-range baryon number transport over rapidity and considerable transverse momentum p_t enhancement. In the latter case, the observed strong enhancement in the proton to pion ratio is discussed in the framework of quark coalescence. As a consequence, collectivity at the partonic level becomes important. Fig.5.4 shows several particle ratios as a function of p_t from calculations with RQMD. The solid lines and dashed lines represent the baryon over pion and meson over pion ratios, respectively. All ratios increase as p_t increases, but the ratios from protons reach much higher values than those of ϕ mesons. In RQMD, the enhancement is mainly due to multiple rescattering among produced particles. In the limit of frequent rescattering, the hydrodynamical behavior is expected to appear [54].

In the calculations, the strong enhancement of protons over pions as a function of transverse momentum comes from the rescattering at the late hadronic stage. On the other hand, the collectivity may have developed at the early partonic

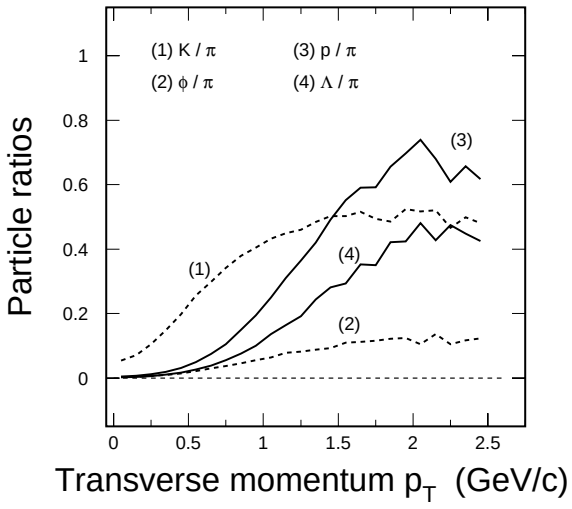

Figure 5.4: Transverse momentum dependence of the mid-rapidity particle ratios of charged kaons over charged pions (K/π), ϕ mesons over charged pions (ϕ/π), (anti)protons over charged pions (p/π), and (anti)lambdas over charged pions (Λ/π), from Au + Au collisions at $\sqrt{s_{NN}} = 200$ GeV by RQMD. The results are from the 10% most central ($b \leq 3$ fm) collisions.

stage in high energy collisions at the RHIC. Pions and protons might dominantly participate in rescattering at the late hadronic stage. Since collectivity is cumulative, one cannot unambiguously identify the dominant origin of the collectivity from the measurement of pions and protons only. The study of other particle species with much smaller hadronic cross sections will allow us to identify and characterize collectivity at the partonic stage.

As shown in Fig. 5.4, the ratio of ϕ mesons over charged pions (ϕ/π) is much lower than that of either (anti)protons over charged pions (p/π) or (anti)lambdas over charged pions (Λ/π). This is due to the small hadronic cross section of ϕ mesons as implemented in RQMD. The ϕ-meson shows only little interaction in the hadron gas leading to an early freeze-out time at small transverse radius, as can be seen in Fig. 5.5. The ϕ meson might freeze-out as soon as it formed. Therefore, eventual collective motion of the ϕ meson might have been dominantly built up during the prehadronic, or in other words, partonic stage. At the maximum SPS energy ($\sqrt{s_{NN}} \approx 17.2$ GeV), the multistrange baryon Ω might be less sensitive to hadronic rescattering [115]. It seems that multistrange particles freeze-out earlier compared with nonstrange ones. So in order to identify and study partonic collectivity, a systematic study of the distributions of ϕ mesons and other multistrange particles, including both elliptical and radial flow, is essential.

5.4 Net baryon in RQMD

As discussed in Ref. [117], the mid-rapidity $\bar{p}/p$ ratio is increasing as collision energy increasing which means the system in the middle rapidity is approaching to net-baryon free. This can be seen more clear from the net baryon rapidity distribution for different CMS energy as shown in Fig. 5.6. The net baryon is calculated as $(P + \Lambda) - (\bar{P} + \bar{\Lambda})$. Please note that in order to have a clear picture with the results from different CMS energy, the abscissa in Fig. 5.6 has been scaled by $1/y_{beam}$. In the full stopping limit, the projectiles and target baryons will lose all the memory of their initial state. The produced particles will then be spherical distribution. In the case of nuclear transparent, the two colliding nuclei will just pass through each other and leave the trail of energy between the

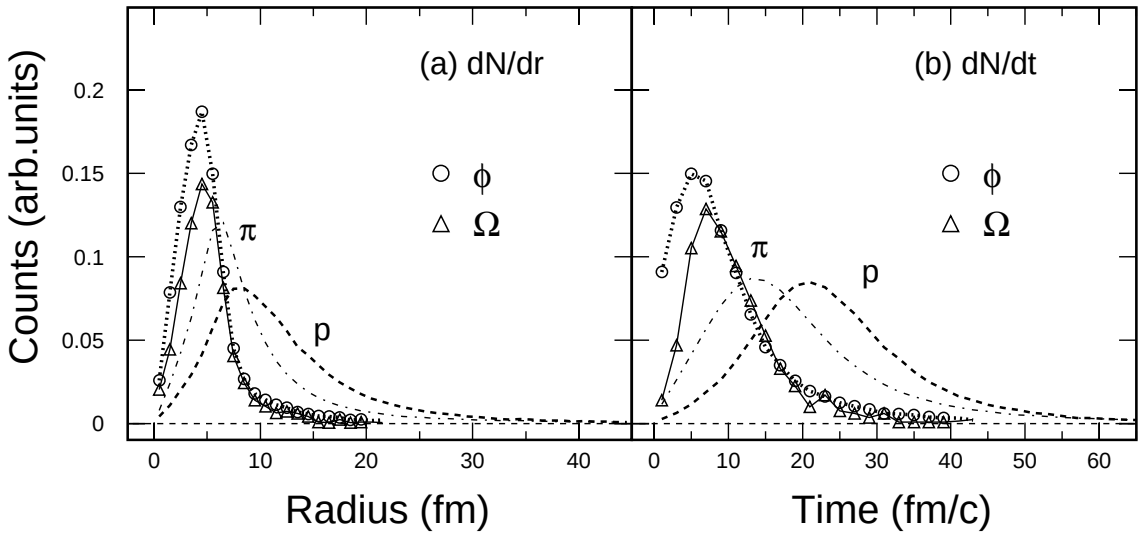

Figure 5.5: The RQMD transverse freeze-out radius (a) and freeze-out time (b) for charged pions (π), (anti)protons (p), ϕ mesons (ϕ), and the multistrange baryon Ω. The results shown are from 10% most central ($b<3fm$) $^{197}Au + ^{197}Au$ collisions at $\sqrt{s_{NN}}=200$ GeV. The normalization of the distributions is arbitrary.

projectile and target rapidity. Particles will be produced in this region and the net baryon number in this region should be zero. However, the actual situation is not so simple but a mixture of these two extreme cases! In middle rapidity, we can see from the figure, as the energy increasing, the net baryon number is decreasing. Also, the rapidity distribution becomes flatter, thus a central rapidity plateau is formed.

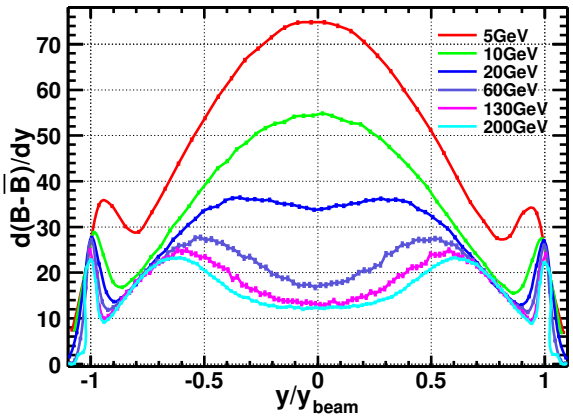

Figure 5.6: Rapidity spectra of net baryons $\langle B - \bar{B} \rangle$ in most central (top 5%) collisions calculated by RQMD. At middle rapidity, from top to bottom, the curve corresponding to CMS energy ($\sqrt{s_{NN}}$) 5 GeV, 10 GeV, 20 GeV, 60 GeV, 130 GeV, 200 GeV, respectively. The abscissa has been scaled by $1/y_{beam}$.

Chapter 6

Discussion

6.1 Kinetic Freeze-out Conditions

A thermal + transverse radial flow model [56] is often used to extract the kinetic freeze-out conditions of the system. The model assumes the system is local thermal equilibrated and boost the thermal source in both longitudinal and transverse direction, thus the invariant momentum spectrum of the particle can be described by

$$\frac{dN}{m_t\, dm_t} \propto \int_0^R r\, dr\, m_t\, K_1\Big(\frac{m_t \cosh\rho}{T_{fo}}\Big)\, I_0\Big(\frac{p_t \sinh\rho}{T_{fo}}\Big) \tag{6.1}$$

where I_0 and K_1 are modified Bessel functions, T_{fo} is interpreted as the kinetic freeze-out temperature, and $\rho = \tanh^{-1}\beta_r(r)$ is the boost rapidity. $\beta_r(r)$ is the transverse velocity distribution in the region $0 \le r \le R$ by a self-similar profile, which is parameterized by the surface radial velocity β_S:

$$\beta_r(r) = \beta_S \left(\frac{r}{R}\right)^{\alpha} \tag{6.2}$$

The exponent α describes the evolution of the flow velocity (flow profile).

By fitting the transverse spectrum of one particle one can extract β_S and T_{fo}. The mean transverse velocity $\langle\beta\rangle$ can be calculated by [114]:

$$\langle\beta\rangle = \frac{\int_0^R r\, dr\, \beta_r(r)}{\int_0^R r\, dr} = \Big(\frac{2}{2+\alpha}\Big)\beta_S \tag{6.3}$$

However, as already discussed in Ref. [114], a strong anticorrelation exist between these two parameters, thus several possible combinations of β_S and T_{fo} may describe the data well. By simultaneously fitting the transverse spectra of different particles may help to remove this ambiguity.

Fig. 6.1(a) shows the fit results of the spectra of π, K, proton and anti-proton from $\sqrt{s_{NN}} = 200$ GeV Au + Au collisions. The spectra of π and K are taken from Ref. [129], (anti-)proton are from this analysis. The top plot shows the kinetic freeze-out temperature. The yellow dashed band is the chemical freeze-out temperature extracted by a chemical-equilibrium (statistical) model. As centrality increase, the temperature T_{fo} decrease, while the chemical freeze-out temperature

T_{ch} is independent of the collision centrality. This can be understood as following: although the Au + Au collisions in different centrality might have different initial conditions, they all evolve to the same chemical freeze-out condition and then expand because of elastic collision. However, the system in central collision have more particles than in peripheral collision, they will require more time to reach kinetic freeze-out, thus the temperature at this stage must be smaller than in peripheral collision. Also, the expansion of the system in central collision is stronger than in peripheral collision, this will lead to larger collective flow. This can be seen in the middle plot of Fig. 6.1(a). The mean transverse velocity increase with centrality. Fig. 6.1(b) shows the χ^2 contours of the kinetic freeze-out temperature parameter and transverse velocity parameter.

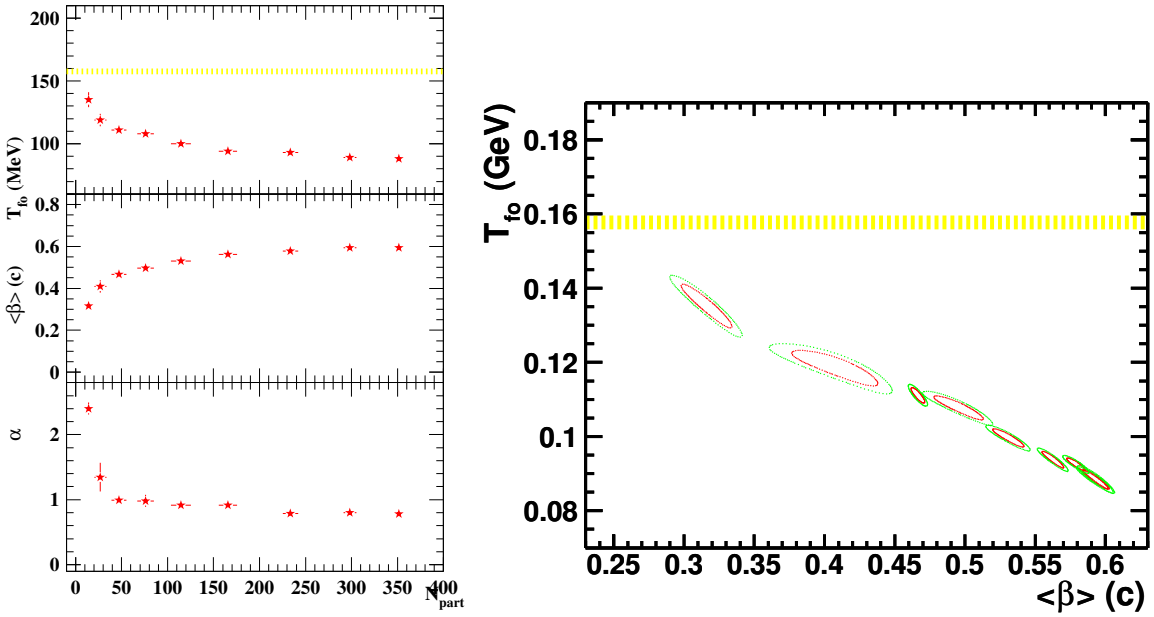

(a) (b)

Figure 6.1: (a): Kinetic freeze-out temperature T_{fo}, mean transverse flow velocity $\langle\beta\rangle$ and the velocity profile α as a function of number of participants (N_{part}) extracted from a simultaneous fit to $\pi^{\pm}$, $K^{\pm}$, p and $\bar{p}$ spectra from $\sqrt{s_{NN}} = 200$ GeV Au + Au collisions. (b): The χ^2 contours for π, K and p. The yellow dashed band denotes the chemical freeze-out temperature [129].

The bottom plot of Fig. 6.1(a) shows the centrality dependence of the velocity profile parameter α. We can see α decrease as centrality increase, the value is larger than 1 for peripheral collision and less than 1 for central collision. From Eq. 6.2, the differential of $\beta_r(r)$ is $d\beta_r(r) = \alpha\beta_S r^{\alpha-1} dr/R^{\alpha}$. $\alpha = 1$ means the acceleration respect to the radius is a constant, while $\alpha > 1$ means the acceleration is increase, $\alpha < 1$ means decrease. While the velocity profile extracted from RQMD (Fig. 1 of Ref. [114]) shows a mixture of these three components. The acceleration respect to the radius at first increase, then constant, and decrease as the radius increase. So the profile used in our fit is an average of these three stages. The system size in different centrality then will determine this final average results. The system size

is small in peripheral collision compared to in central collision, thus the velocity profile parameter α will be larger. As we can see that in the bottom plot of Fig. 6.1(a).

Also, because of many of the detected particles are not originate from the thermal source but from resonance decays, it is suggested in Ref. [56], we must be careful when interpreting the spectrum fits made without feed-down correction from resonance decay. We did some model study by employing the RQMD model. We first get the spectra of π, K, P, Λ, Ξ, Ω, ϕ (all the corresponding anti-particles are included too), then apply the thermal model fit to these particles. We classify the particles into two groups when applying the fit. π, K, P and Λ belong to one group; the multi-strange particles Ξ, Ω and ϕ belong to the other group. It's believed the particles in the later group will freeze-out earlier [115, 116], thus have different kinetic freeze-out condition. Then we extract all the resonance particles out from RQMD, and simulate the decay of these particles by using the PYTHIA [104] event generator. The branch ratio of the different decay channel is already considered in PYTHIA. The decay products are merged into the initial produced particle. Then we fit the spectra again. The results of the both fits are shown in Fig. 6.2. As can be seen from the plot, RQMD results have similar trend as seen in data although the absolute value is larger than data. Also the effect on the extracted fit parameters after applying feed-down correction is small under the framework of RQMD.

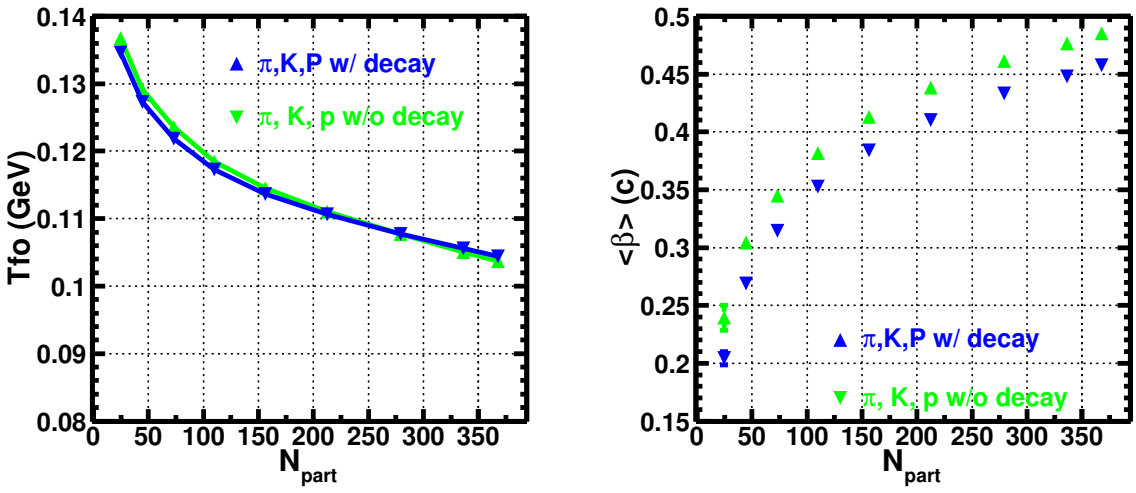

Figure 6.2: The kinetic freeze-out parameters T_{fo} (left) and $\langle\beta\rangle$ (right) extracted from the RQMD model. The plot shows the results without resonance decay and after resonance decay. The resonance decay has less effect on the kinetic freeze-out conditions.

6.1.1 dN/dy and $\langle p_t \rangle$

We only measured the yield in p_t range $0.45 - 1.05$ GeV/c. The yield not covered in this range was extracted from the thermal model fit. The fiducial yields are shown in table A.6 and A.7, while the integrated yields are shown in table A.8 and A.9. We can see from the table that about 50% of the integrated yields are measured. The proton and anti-proton rapidity distributions for different central-

ity bin are shown in Fig. 6.3. For both proton and anti-proton, dN/dy is found to be uniform as a function of rapidity within $|y| < 0.5$. This indicating that a boost invariant region of at least one unit of rapidity has developed for all the centrality. Also, it's interesting to study the rapidity distribution (or other characteristic parameters, such as v_2) of different mass hadrons at higher rapidity regions to test the validity of the boost invariant region.

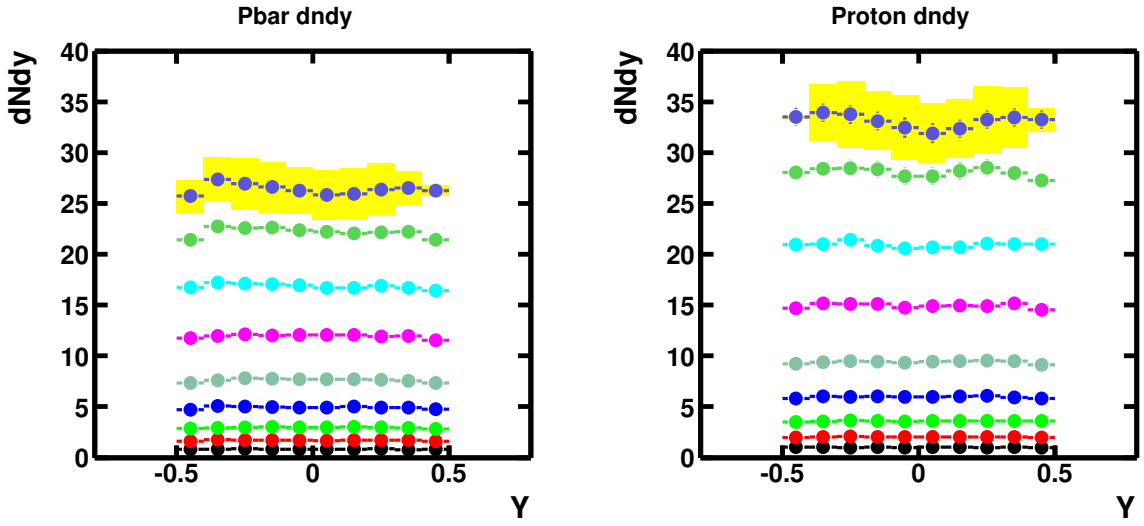

Figure 6.3: Rapidity distributions of the integrated yields for anti-proton (left) and proton (right) from most peripheral (bottom) to most central (top) collisions in $\sqrt{s_{NN}} = 200$ GeV Au + Au collisions at RHIC. The bands denote the systematic error.

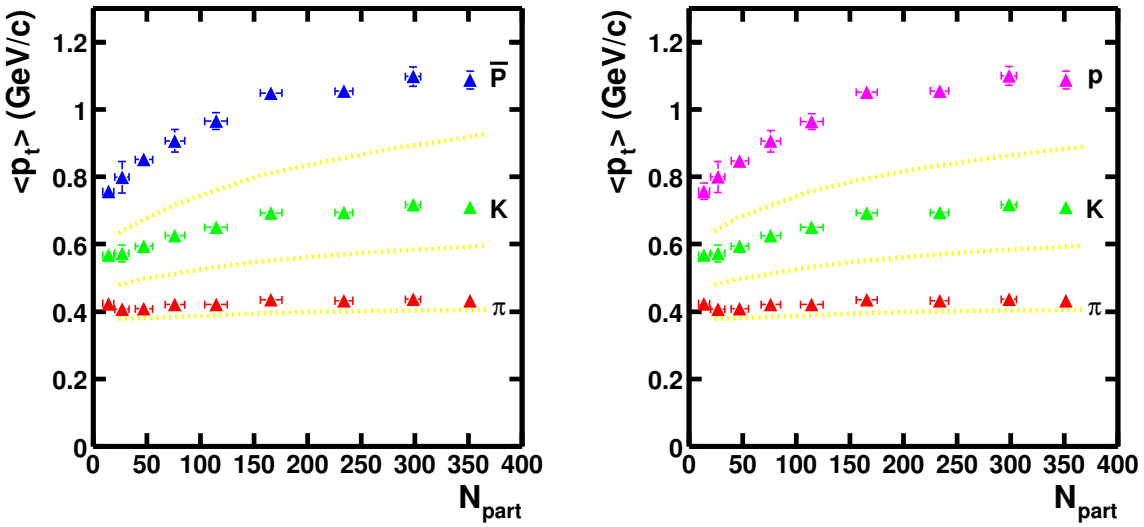

Figure 6.4: Midrapidity $\langle p_t \rangle$ of the anti-proton (left) and proton (right) as a function of the number of participants in the collision from $\sqrt{s_{NN}} = 200$ GeV Au + Au collisions at RHIC. The bands denote the results from RQMD with same collision energy and species.

The $\langle p_t \rangle$ of proton and anti-proton are also extracted by extrapolating the mea-

sured yields with thermal fit. The centrality dependence of $\langle p_t \rangle$ within $|y| < 0.1$ is shown in Fig. 6.4. RQMD results are shown in the plot too. Our results are consistent with the PHENIX results, so the discussion in chapter 5 can be applied to our data too. Also, as discussed in [116], the increase of $\langle p_t \rangle$ for different particles as the function of collision centrality is reflected by the development of the collective flow, or more specific, in the values of the mean transverse velocity $\langle \beta \rangle$.

6.2 $\bar{p}/p$ ratio and Energy Dependence

Fig. 6.5 shows the $\bar{p}/p$ ratio as a function of rapidity and collision centrality. For the rapidity distribution, the plot is for most central collision. The ratio is about 0.8 and is constant within the measured rapidity region. The centrality dependence of the $\bar{p}/p$ ratio is integrated over rapidity region $|y| < 0.1$ and p_t region $0.45-1.05$ GeV/c. The ratio is almost a constant within the error bar. However, there is a trend of a systematic drop from peripheral collisions to central collisions. This is consistent with that more annihilation of protons and anti-protons in central collisions relative to peripheral collisions. The results from RQMD shows the same trend, however, RQMD underpredicts the absolute value of the $\bar{p}/p$ ratio which may be due to too much final stage rescattering in the model.

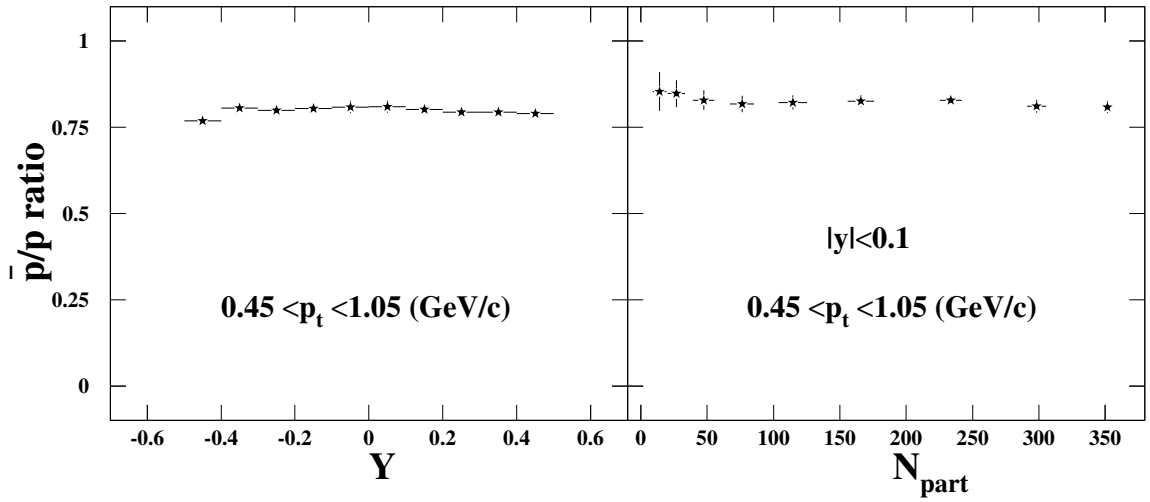

Figure 6.5: $\bar{p}/p$ as a function of rapidity within $0.45 < p_t < 1.05$ GeV/c (left) and as a function of centrality within $|y| < 0.1$ and $0.45 < p_t < 1.05$ GeV/c (right). The left plot is for most central collision.

Finally, Fig. 6.6 shows the energy dependence of $\bar{p}/p$ ratio for both central heavy-ion collisions and elementary p + p collisions. We can see that there is a dramatic increase of the $\bar{p}/p$ ratio from AGS to SPS and to RHIC. It means the middle rapidity region is approaching to net baryon free, but not at RHIC.

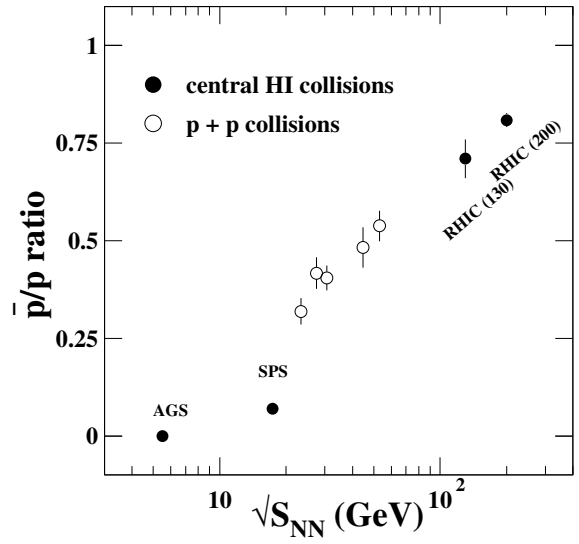

Figure 6.6: Midrapidity $\bar{p}/p$ ratio in central heavy-ion collisions (filled symbols) and elementary p + p collisions (open symbols).

Chapter 7

Summary

In summary, the mid-rapidity proton and anti-proton yields are presented for the $\sqrt{s_{NN}} = 200$ GeV Au+Au data sets which were taken by the STAR detector in 2001 run. The results are from transverse momentum range $0.4 < p_t < 1.05$ GeV/c and rapidity range $|y| < 0.5$. The transverse momentum distributions of both proton and anti-proton become more convex from peripheral to central collisions implying the strong collective expansion at the early stage of the collision. The measured rapidity distribution are flat within $|y| < 0.5$ indicating a boost invariant region around mid-rapidity. $\bar{p}/p$ is independent of rapidity region $|y| < 0.5$, and decreases slightly from peripheral collision (≈ 0.85) to central collision (≈ 0.80). It's still not yet net baryon free at RHIC energy. The slight decrease in the $\bar{p}/p$ ratio reflects the rich collision dynamics at RHIC: both initial baryon transfer and final stage hadronic rescatterings are important for the observation.

By applying a thermal + radial flow fit to the proton data, the kinetic freeze-out condition are extracted. $\langle p_t \rangle$ are calculated by extrapolating the measured spectra with thermal model. The kinetic freeze-out temperature decreases from peripheral ($\approx$ 135 MeV) to most central collision ($\approx$ 89 MeV). They are all smaller than the chemical freeze-out temperature($\approx 160 \pm 5$ MeV) indicating an additional hadronic rescattering phase after the chemical freeze-out in Au + Au collisions at RHIC. The transverse flow velocity increase from peripheral to central collision. The centrality dependence of $\langle p_t \rangle$ for different particles (π, K, P) confirm this conclusion.

The same results are also calculated by employing a transport model Relativistic Quantum Molecular Dynamics (RQMD). The spectra of different particles (π, K, P) are not following the so called m_t scaling. While the $\langle p_t \rangle$ of them show similar trend with the experiment data despite of the underestimation of the absolute value. The fact that multi-strange particles (ϕ, Ξ, Ω) freeze-out earlier is demonstrated with this model from the freeze-out time and radius distribution. The measurement of these particles are necessary to confirm this conclusion. By applying thermal model fit to the spectra from this model, the same trend of kinetic freeze-out condition as in data is observed. While after switch off the rescattering in this model, the violation of m_t scaling and the centrality dependence of $\langle p_t \rangle$ disappear. This indicates the importance of rescattering in heavy-ion collisions. However, only hadronic interactions are included in RQMD. Such hadronic interaction does not generate enough collective flow comparing to data. This demonstrates that

partonic collectivity is needed in the heavy ion collisions at RHIC. The realization of the partonic collectivity is important toward the understanding of the partonic equation of state in high-energy nuclear collisions.

Appendix A

Data Table

Cent. bin	T_{fo} (MeV)	$\langle\beta_t\rangle$ (c)	$\bar{p}$ $\langle p_t\rangle$ (GeV/c)	p $\langle p_t\rangle$ (GeV/c)
70-80%	135 ± 6	0.316 ± 0.018	0.756 ± 0.023	0.757 ± 0.024
60-70%	119 ± 5	0.410 ± 0.030	0.799 ± 0.047	0.800 ± 0.046
50-60%	111 ± 2	0.467 ± 0.005	0.851 ± 0.006	0.847 ± 0.007
40-50%	108 ± 3	0.496 ± 0.019	0.907 ± 0.034	0.906 ± 0.032
30-40%	100 ± 2	0.531 ± 0.011	0.965 ± 0.025	0.964 ± 0.024
20-30%	94 ± 2	0.563 ± 0.008	1.049 ± 0.022	1.051 ± 0.021
10-20%	93 ± 2	0.579 ± 0.007	1.054 ± 0.018	1.055 ± 0.017
5-10%	89 ± 3	0.593 ± 0.009	1.098 ± 0.029	1.100 ± 0.028
0-5%	88 ± 2	0.593 ± 0.009	1.087 ± 0.027	1.087 ± 0.026

Table A.1: The parameters from the thermal + transverse radial flow fit. T_{fo} and $\langle\beta_t\rangle$ are the extracted temperature and mean collective transverse velocity parameters, respectively. The value of $\langle p_t\rangle$ is extracted from the full distribution and its error is based on a 68% confidence level. For this fit, the spectra of charged pions, kaons and (anti-)protons were used.

p_t	$70-80\%$	$60-70\%$	$50-60\%$	$40-50\%$
0.425	$0.309 \pm 0.013 \pm 0.048$	$0.587 \pm 0.019 \pm 0.069$	$0.861 \pm 0.023 \pm 0.112$	$1.374 \pm 0.029 \pm 0.165$
0.475	$0.280 \pm 0.012 \pm 0.031$	$0.523 \pm 0.016 \pm 0.047$	$0.839 \pm 0.021 \pm 0.072$	$1.276 \pm 0.026 \pm 0.130$
0.525	$0.250 \pm 0.011 \pm 0.014$	$0.481 \pm 0.015 \pm 0.046$	$0.794 \pm 0.019 \pm 0.082$	$1.166 \pm 0.024 \pm 0.092$
0.575	$0.225 \pm 0.010 \pm 0.012$	$0.449 \pm 0.014 \pm 0.040$	$0.749 \pm 0.018 \pm 0.071$	$1.126 \pm 0.022 \pm 0.107$
0.625	$0.208 \pm 0.009 \pm 0.016$	$0.403 \pm 0.012 \pm 0.028$	$0.678 \pm 0.016 \pm 0.056$	$1.022 \pm 0.020 \pm 0.088$
0.675	$0.171 \pm 0.008 \pm 0.005$	$0.327 \pm 0.011 \pm 0.031$	$0.633 \pm 0.015 \pm 0.055$	$0.973 \pm 0.019 \pm 0.074$
0.725	$0.151 \pm 0.007 \pm 0.012$	$0.318 \pm 0.010 \pm 0.027$	$0.559 \pm 0.014 \pm 0.038$	$0.888 \pm 0.018 \pm 0.069$
0.775	$0.136 \pm 0.007 \pm 0.007$	$0.290 \pm 0.009 \pm 0.017$	$0.531 \pm 0.013 \pm 0.048$	$0.839 \pm 0.017 \pm 0.063$
0.825	$0.130 \pm 0.006 \pm 0.006$	$0.257 \pm 0.009 \pm 0.022$	$0.474 \pm 0.012 \pm 0.034$	$0.762 \pm 0.015 \pm 0.050$
0.875	$0.101 \pm 0.005 \pm 0.013$	$0.240 \pm 0.008 \pm 0.018$	$0.457 \pm 0.011 \pm 0.033$	$0.716 \pm 0.014 \pm 0.055$
0.925	$0.096 \pm 0.005 \pm 0.003$	$0.207 \pm 0.007 \pm 0.011$	$0.397 \pm 0.010 \pm 0.016$	$0.654 \pm 0.013 \pm 0.036$
0.975	$0.080 \pm 0.005 \pm 0.002$	$0.178 \pm 0.007 \pm 0.008$	$0.345 \pm 0.009 \pm 0.016$	$0.554 \pm 0.012 \pm 0.023$
1.025	$0.063 \pm 0.004 \pm 0.005$	$0.153 \pm 0.006 \pm 0.008$	$0.288 \pm 0.009 \pm 0.010$	$0.489 \pm 0.011 \pm 0.008$

Table A.2: Anti-proton spectra in 70-80%, 60-70%, 50-60%, 40-50% Au+Au collisions. The unit of p_t is GeV/c.

p_t	$30-40\%$	$20-30\%$	$10-20\%$	$5-10\%$	$0-5\%$
0.425	$1.842 \pm 0.033 \pm 0.274$	$2.579 \pm 0.039 \pm 0.344$	$3.468 \pm 0.046 \pm 0.430$	$4.213 \pm 0.070 \pm 0.622$	$4.929 \pm 0.080 \pm 0.605$
0.475	$1.818 \pm 0.031 \pm 0.244$	$2.423 \pm 0.035 \pm 0.315$	$3.247 \pm 0.042 \pm 0.360$	$4.097 \pm 0.066 \pm 0.516$	$4.694 \pm 0.073 \pm 0.535$
0.525	$1.679 \pm 0.028 \pm 0.166$	$2.231 \pm 0.032 \pm 0.235$	$3.140 \pm 0.039 \pm 0.346$	$3.891 \pm 0.061 \pm 0.422$	$4.690 \pm 0.070 \pm 0.579$
0.575	$1.571 \pm 0.026 \pm 0.165$	$2.214 \pm 0.031 \pm 0.218$	$3.013 \pm 0.037 \pm 0.325$	$3.836 \pm 0.058 \pm 0.374$	$4.434 \pm 0.065 \pm 0.429$
0.625	$1.527 \pm 0.025 \pm 0.111$	$2.131 \pm 0.029 \pm 0.193$	$2.896 \pm 0.034 \pm 0.270$	$3.714 \pm 0.055 \pm 0.356$	$4.351 \pm 0.060 \pm 0.450$
0.675	$1.445 \pm 0.023 \pm 0.117$	$1.982 \pm 0.027 \pm 0.188$	$2.726 \pm 0.032 \pm 0.254$	$3.538 \pm 0.051 \pm 0.285$	$4.249 \pm 0.059 \pm 0.409$
0.725	$1.306 \pm 0.021 \pm 0.116$	$1.868 \pm 0.025 \pm 0.152$	$2.676 \pm 0.031 \pm 0.215$	$3.282 \pm 0.048 \pm 0.263$	$4.013 \pm 0.058 \pm 0.281$
0.775	$1.216 \pm 0.020 \pm 0.100$	$1.805 \pm 0.024 \pm 0.132$	$2.564 \pm 0.030 \pm 0.203$	$3.185 \pm 0.048 \pm 0.224$	$3.714 \pm 0.056 \pm 0.191$
0.825	$1.202 \pm 0.020 \pm 0.103$	$1.776 \pm 0.024 \pm 0.157$	$2.484 \pm 0.028 \pm 0.228$	$3.075 \pm 0.046 \pm 0.208$	$3.716 \pm 0.053 \pm 0.079$
0.875	$1.128 \pm 0.018 \pm 0.080$	$1.628 \pm 0.022 \pm 0.138$	$2.375 \pm 0.027 \pm 0.203$	$2.984 \pm 0.042 \pm 0.179$	$3.543 \pm 0.050 \pm 0.028$
0.925	$1.008 \pm 0.016 \pm 0.070$	$1.534 \pm 0.021 \pm 0.135$	$2.184 \pm 0.026 \pm 0.177$	$2.822 \pm 0.041 \pm 0.177$	$3.265 \pm 0.048 \pm 0.079$
0.975	$0.905 \pm 0.015 \pm 0.044$	$1.405 \pm 0.019 \pm 0.115$	$2.012 \pm 0.026 \pm 0.144$	$2.549 \pm 0.038 \pm 0.139$	$3.038 \pm 0.051 \pm 0.061$
1.025	$0.813 \pm 0.014 \pm 0.044$	$1.243 \pm 0.018 \pm 0.100$	$1.854 \pm 0.025 \pm 0.205$	$2.286 \pm 0.036 \pm 0.083$	$2.806 \pm 0.046 \pm 0.021$

Table A.3: Anti-proton spectra in 30-40%, 20-30%, 10-20%, 5-10%, 0-5% Au+Au collisions. The unit of p_t is GeV/c.

p_t	$70-80\%$	$60-70\%$	$50-60\%$	$40-50\%$
0.425	$0.327 \pm 0.104 \pm 0.048$	$0.650 \pm 0.158 \pm 0.091$	$1.129 \pm 0.204 \pm 0.163$	$1.591 \pm 0.253 \pm 0.167$
0.475	$0.362 \pm 0.082 \pm 0.051$	$0.598 \pm 0.110 \pm 0.046$	$1.066 \pm 0.144 \pm 0.117$	$1.511 \pm 0.182 \pm 0.166$
0.525	$0.317 \pm 0.060 \pm 0.031$	$0.629 \pm 0.082 \pm 0.076$	$1.025 \pm 0.109 \pm 0.132$	$1.477 \pm 0.135 \pm 0.142$
0.575	$0.264 \pm 0.037 \pm 0.025$	$0.512 \pm 0.061 \pm 0.031$	$0.864 \pm 0.074 \pm 0.079$	$1.426 \pm 0.115 \pm 0.167$
0.625	$0.241 \pm 0.029 \pm 0.026$	$0.493 \pm 0.038 \pm 0.044$	$0.822 \pm 0.061 \pm 0.078$	$1.269 \pm 0.077 \pm 0.120$
0.675	$0.210 \pm 0.021 \pm 0.019$	$0.418 \pm 0.039 \pm 0.041$	$0.760 \pm 0.054 \pm 0.062$	$1.256 \pm 0.068 \pm 0.128$
0.725	$0.196 \pm 0.018 \pm 0.015$	$0.398 \pm 0.029 \pm 0.032$	$0.665 \pm 0.035 \pm 0.058$	$1.066 \pm 0.044 \pm 0.093$
0.775	$0.172 \pm 0.009 \pm 0.019$	$0.363 \pm 0.019 \pm 0.033$	$0.635 \pm 0.032 \pm 0.055$	$1.012 \pm 0.047 \pm 0.090$
0.825	$0.141 \pm 0.009 \pm 0.004$	$0.315 \pm 0.016 \pm 0.022$	$0.564 \pm 0.020 \pm 0.046$	$0.914 \pm 0.029 \pm 0.070$
0.875	$0.133 \pm 0.006 \pm 0.009$	$0.275 \pm 0.012 \pm 0.024$	$0.513 \pm 0.018 \pm 0.041$	$0.854 \pm 0.025 \pm 0.061$
0.925	$0.114 \pm 0.009 \pm 0.010$	$0.246 \pm 0.012 \pm 0.021$	$0.493 \pm 0.016 \pm 0.036$	$0.760 \pm 0.020 \pm 0.058$
0.975	$0.089 \pm 0.006 \pm 0.005$	$0.202 \pm 0.007 \pm 0.011$	$0.411 \pm 0.013 \pm 0.032$	$0.691 \pm 0.018 \pm 0.036$
1.025	$0.077 \pm 0.006 \pm 0.004$	$0.193 \pm 0.007 \pm 0.006$	$0.346 \pm 0.010 \pm 0.015$	$0.610 \pm 0.015 \pm 0.029$

Table A.4: Proton spectra in 70-80%, 60-70%, 50-60%, 40-50% Au+Au collisions. The unit of p_t is GeV/c.

p_t	$30-40\%$	$20-30\%$	$10-20\%$	$5-10\%$	$0-5\%$
0.425	$2.237 \pm 0.323 \pm 0.281$	$2.890 \pm 0.374 \pm 0.314$	$3.972 \pm 0.475 \pm 0.404$	$4.986 \pm 0.749 \pm 0.684$	$5.752 \pm 0.810 \pm 0.784$
0.475	$2.244 \pm 0.226 \pm 0.319$	$2.860 \pm 0.268 \pm 0.332$	$4.012 \pm 0.335 \pm 0.505$	$4.944 \pm 0.543 \pm 0.701$	$5.781 \pm 0.610 \pm 0.749$
0.525	$2.089 \pm 0.174 \pm 0.235$	$2.889 \pm 0.206 \pm 0.355$	$3.879 \pm 0.256 \pm 0.461$	$4.824 \pm 0.407 \pm 0.636$	$5.791 \pm 0.492 \pm 0.628$
0.575	$2.028 \pm 0.139 \pm 0.215$	$2.756 \pm 0.153 \pm 0.294$	$3.744 \pm 0.189 \pm 0.392$	$4.634 \pm 0.304 \pm 0.497$	$5.595 \pm 0.368 \pm 0.580$
0.625	$1.831 \pm 0.101 \pm 0.162$	$2.620 \pm 0.115 \pm 0.272$	$3.550 \pm 0.147 \pm 0.360$	$4.661 \pm 0.251 \pm 0.554$	$5.456 \pm 0.267 \pm 0.554$
0.675	$1.756 \pm 0.081 \pm 0.170$	$2.471 \pm 0.086 \pm 0.231$	$3.500 \pm 0.128 \pm 0.349$	$4.372 \pm 0.191 \pm 0.423$	$5.355 \pm 0.207 \pm 0.515$
0.725	$1.623 \pm 0.058 \pm 0.148$	$2.318 \pm 0.069 \pm 0.206$	$3.192 \pm 0.089 \pm 0.293$	$4.198 \pm 0.137 \pm 0.364$	$4.858 \pm 0.181 \pm 0.331$
0.775	$1.535 \pm 0.046 \pm 0.115$	$2.161 \pm 0.056 \pm 0.180$	$3.154 \pm 0.086 \pm 0.266$	$3.973 \pm 0.148 \pm 0.312$	$4.846 \pm 0.149 \pm 0.357$
0.825	$1.393 \pm 0.037 \pm 0.133$	$2.131 \pm 0.051 \pm 0.185$	$3.001 \pm 0.062 \pm 0.257$	$3.797 \pm 0.097 \pm 0.298$	$4.496 \pm 0.119 \pm 0.257$
0.875	$1.383 \pm 0.034 \pm 0.127$	$1.992 \pm 0.040 \pm 0.171$	$2.905 \pm 0.053 \pm 0.236$	$3.687 \pm 0.080 \pm 0.296$	$4.391 \pm 0.105 \pm 0.251$
0.925	$1.215 \pm 0.029 \pm 0.098$	$1.834 \pm 0.034 \pm 0.145$	$2.653 \pm 0.045 \pm 0.216$	$3.389 \pm 0.074 \pm 0.224$	$4.075 \pm 0.086 \pm 0.114$
0.975	$1.102 \pm 0.022 \pm 0.058$	$1.695 \pm 0.034 \pm 0.118$	$2.427 \pm 0.039 \pm 0.199$	$3.228 \pm 0.058 \pm 0.193$	$3.699 \pm 0.074 \pm 0.018$
1.025	$0.974 \pm 0.020 \pm 0.051$	$1.537 \pm 0.028 \pm 0.105$	$2.280 \pm 0.035 \pm 0.175$	$2.914 \pm 0.057 \pm 0.125$	$3.399 \pm 0.069 \pm 0.191$

Table A.5: Proton spectra in 30-40%, 20-30%, 10-20%, 5-10%, 0-5% Au+Au collisions. The unit of p_t is GeV/c.

Rapidity	$70-80\%$	$60-70\%$	$50-60\%$	$40-50\%$
-0.45	$0.443 \pm 0.009 \pm 0.006$	$0.868 \pm 0.013 \pm 0.007$	$1.516 \pm 0.020 \pm 0.035$	$2.398 \pm 0.022 \pm 0.072$
-0.35	$0.437 \pm 0.008 \pm 0.013$	$0.938 \pm 0.012 \pm 0.040$	$1.563 \pm 0.016 \pm 0.070$	$2.574 \pm 0.022 \pm 0.125$
-0.25	$0.452 \pm 0.008 \pm 0.023$	$0.914 \pm 0.012 \pm 0.061$	$1.582 \pm 0.016 \pm 0.111$	$2.565 \pm 0.020 \pm 0.154$
-0.15	$0.425 \pm 0.008 \pm 0.030$	$0.915 \pm 0.012 \pm 0.064$	$1.620 \pm 0.016 \pm 0.132$	$2.538 \pm 0.020 \pm 0.197$
-0.05	$0.450 \pm 0.008 \pm 0.026$	$0.922 \pm 0.012 \pm 0.079$	$1.587 \pm 0.016 \pm 0.118$	$2.494 \pm 0.020 \pm 0.187$
0.05	$0.437 \pm 0.008 \pm 0.030$	$0.887 \pm 0.012 \pm 0.065$	$1.598 \pm 0.016 \pm 0.128$	$2.496 \pm 0.020 \pm 0.189$
0.15	$0.433 \pm 0.008 \pm 0.027$	$0.906 \pm 0.012 \pm 0.078$	$1.617 \pm 0.016 \pm 0.112$	$2.546 \pm 0.020 \pm 0.205$
0.25	$0.453 \pm 0.008 \pm 0.021$	$0.921 \pm 0.012 \pm 0.060$	$1.589 \pm 0.016 \pm 0.102$	$2.502 \pm 0.020 \pm 0.180$
0.35	$0.417 \pm 0.008 \pm 0.010$	$0.923 \pm 0.012 \pm 0.042$	$1.561 \pm 0.018 \pm 0.061$	$2.491 \pm 0.021 \pm 0.100$
0.45	$0.446 \pm 0.037 \pm 0.006$	$0.860 \pm 0.015 \pm 0.004$	$1.491 \pm 0.017 \pm 0.044$	$2.408 \pm 0.022 \pm 0.056$
-0.45	$0.536 \pm 0.014 \pm 0.001$	$1.053 \pm 0.020 \pm 0.022$	$1.875 \pm 0.039 \pm 0.017$	$2.975 \pm 0.048 \pm 0.009$
-0.35	$0.539 \pm 0.020 \pm 0.016$	$1.085 \pm 0.032 \pm 0.076$	$1.910 \pm 0.042 \pm 0.114$	$3.077 \pm 0.051 \pm 0.195$
-0.25	$0.531 \pm 0.020 \pm 0.047$	$1.118 \pm 0.036 \pm 0.087$	$1.955 \pm 0.049 \pm 0.141$	$3.056 \pm 0.067 \pm 0.242$
-0.15	$0.539 \pm 0.027 \pm 0.038$	$1.094 \pm 0.033 \pm 0.082$	$1.929 \pm 0.048 \pm 0.167$	$3.067 \pm 0.092 \pm 0.247$
-0.05	$0.527 \pm 0.034 \pm 0.047$	$1.088 \pm 0.049 \pm 0.097$	$1.915 \pm 0.064 \pm 0.181$	$3.050 \pm 0.085 \pm 0.274$
0.05	$0.541 \pm 0.035 \pm 0.053$	$1.091 \pm 0.053 \pm 0.090$	$1.947 \pm 0.071 \pm 0.175$	$3.039 \pm 0.087 \pm 0.260$
0.15	$0.542 \pm 0.019 \pm 0.035$	$1.090 \pm 0.042 \pm 0.082$	$1.921 \pm 0.055 \pm 0.166$	$3.075 \pm 0.077 \pm 0.257$
0.25	$0.527 \pm 0.018 \pm 0.035$	$1.094 \pm 0.034 \pm 0.085$	$1.938 \pm 0.047 \pm 0.148$	$3.099 \pm 0.065 \pm 0.260$
0.35	$0.531 \pm 0.021 \pm 0.024$	$1.099 \pm 0.031 \pm 0.070$	$1.921 \pm 0.042 \pm 0.114$	$3.017 \pm 0.068 \pm 0.180$
0.45	$0.505 \pm 0.016 \pm 0.001$	$1.071 \pm 0.023 \pm 0.010$	$1.940 \pm 0.042 \pm 0.029$	$2.966 \pm 0.047 \pm 0.014$

Table A.6: Fiducial ($0.40 < p_t < 1.05$ GeV/c) yield of anti-proton (top) and proton (bottom) for different rapidity bins in 70-80%, 60-70%, 50-60%, 40-50% Au+Au collisions.

Rapidity	$30-40\%$	$20-30\%$	$10-20\%$	$5-10\%$	$0-5\%$
-0.45	$3.567 \pm 0.028 \pm 0.141$	$5.215 \pm 0.036 \pm 0.396$	$7.500 \pm 0.047 \pm 0.432$	$9.092 \pm 0.068 \pm 0.953$	$11.095 \pm 0.081 \pm 1.118$
-0.35	$3.681 \pm 0.025 \pm 0.145$	$5.319 \pm 0.035 \pm 0.284$	$7.724 \pm 0.041 \pm 0.498$	$9.656 \pm 0.066 \pm 0.419$	$11.804 \pm 0.081 \pm 0.585$
-0.25	$3.778 \pm 0.025 \pm 0.287$	$5.391 \pm 0.030 \pm 0.404$	$7.661 \pm 0.038 \pm 0.620$	$9.587 \pm 0.060 \pm 0.762$	$11.627 \pm 0.069 \pm 0.755$
-0.15	$3.753 \pm 0.024 \pm 0.338$	$5.335 \pm 0.029 \pm 0.474$	$7.640 \pm 0.037 \pm 0.675$	$9.607 \pm 0.057 \pm 0.740$	$11.479 \pm 0.067 \pm 0.745$
-0.05	$3.732 \pm 0.024 \pm 0.346$	$5.359 \pm 0.029 \pm 0.495$	$7.600 \pm 0.036 \pm 0.720$	$9.500 \pm 0.056 \pm 0.796$	$11.316 \pm 0.067 \pm 0.615$
0.05	$3.730 \pm 0.024 \pm 0.304$	$5.365 \pm 0.029 \pm 0.506$	$7.471 \pm 0.036 \pm 0.697$	$9.431 \pm 0.056 \pm 0.736$	$11.137 \pm 0.066 \pm 0.703$
0.15	$3.741 \pm 0.024 \pm 0.313$	$5.369 \pm 0.029 \pm 0.469$	$7.471 \pm 0.036 \pm 0.649$	$9.361 \pm 0.057 \pm 0.685$	$11.189 \pm 0.065 \pm 0.744$
0.25	$3.718 \pm 0.025 \pm 0.255$	$5.292 \pm 0.030 \pm 0.409$	$7.568 \pm 0.037 \pm 0.618$	$9.403 \pm 0.060 \pm 0.764$	$11.377 \pm 0.072 \pm 0.783$
0.35	$3.663 \pm 0.039 \pm 0.252$	$5.308 \pm 0.038 \pm 0.303$	$7.490 \pm 0.042 \pm 0.403$	$9.430 \pm 0.065 \pm 0.280$	$11.451 \pm 0.079 \pm 0.353$
0.45	$3.556 \pm 0.027 \pm 0.223$	$5.127 \pm 0.033 \pm 0.329$	$7.365 \pm 0.046 \pm 0.209$	$9.096 \pm 0.078 \pm 0.754$	$11.333 \pm 0.099 \pm 0.590$
-0.45	$4.484 \pm 0.067 \pm 0.039$	$6.471 \pm 0.077 \pm 0.015$	$9.355 \pm 0.117 \pm 0.020$	$11.848 \pm 0.165 \pm 0.666$	$14.442 \pm 0.216 \pm 0.437$
-0.35	$4.562 \pm 0.080 \pm 0.228$	$6.688 \pm 0.101 \pm 0.402$	$9.379 \pm 0.120 \pm 0.634$	$12.019 \pm 0.192 \pm 0.567$	$14.637 \pm 0.220 \pm 0.842$
-0.25	$4.600 \pm 0.088 \pm 0.388$	$6.665 \pm 0.105 \pm 0.589$	$9.561 \pm 0.130 \pm 0.868$	$12.028 \pm 0.233 \pm 0.935$	$14.559 \pm 0.234 \pm 1.058$
-0.15	$4.585 \pm 0.089 \pm 0.385$	$6.655 \pm 0.114 \pm 0.591$	$9.294 \pm 0.137 \pm 0.814$	$11.991 \pm 0.226 \pm 1.026$	$14.279 \pm 0.258 \pm 0.919$
-0.05	$4.539 \pm 0.110 \pm 0.415$	$6.490 \pm 0.125 \pm 0.606$	$9.176 \pm 0.160 \pm 0.852$	$11.712 \pm 0.252 \pm 1.078$	$13.992 \pm 0.293 \pm 1.092$
0.05	$4.591 \pm 0.106 \pm 0.434$	$6.563 \pm 0.126 \pm 0.601$	$9.232 \pm 0.161 \pm 0.875$	$11.712 \pm 0.260 \pm 1.064$	$13.755 \pm 0.291 \pm 0.968$
0.15	$4.606 \pm 0.093 \pm 0.410$	$6.598 \pm 0.112 \pm 0.618$	$9.232 \pm 0.137 \pm 0.849$	$11.915 \pm 0.243 \pm 0.964$	$13.956 \pm 0.237 \pm 0.904$
0.25	$4.646 \pm 0.095 \pm 0.372$	$6.571 \pm 0.108 \pm 0.585$	$9.387 \pm 0.132 \pm 0.823$	$12.057 \pm 0.217 \pm 0.906$	$14.338 \pm 0.229 \pm 1.070$
0.35	$4.598 \pm 0.078 \pm 0.271$	$6.685 \pm 0.101 \pm 0.468$	$9.368 \pm 0.125 \pm 0.649$	$11.846 \pm 0.197 \pm 0.796$	$14.430 \pm 0.218 \pm 0.946$
0.45	$4.432 \pm 0.074 \pm 0.191$	$6.397 \pm 0.087 \pm 0.097$	$9.359 \pm 0.108 \pm 0.136$	$11.528 \pm 0.189 \pm 0.368$	$14.338 \pm 0.207 \pm 0.173$

Table A.7: Fiducial ($0.40 < p_t < 1.05$ GeV/c) yield of anti-proton (top) and proton (bottom) for different rapidity bins in 30-40%, 20-30%, 10-20%, 5-10%, 0-5% Au+Au collisions.

Rapidity	$70-80\%$	$60-70\%$	$50-60\%$	$40-50\%$
-0.45	$0.828 \pm 0.027 \pm 0.000$	$1.613 \pm 0.077 \pm 0.000$	$2.843 \pm 0.040 \pm 1.000$	$4.716 \pm 0.173 \pm 1.000$
-0.35	$0.816 \pm 0.026 \pm 0.006$	$1.743 \pm 0.082 \pm 0.030$	$2.932 \pm 0.034 \pm 0.007$	$5.063 \pm 0.185 \pm 0.065$
-0.25	$0.845 \pm 0.026 \pm 0.000$	$1.699 \pm 0.080 \pm 0.000$	$2.969 \pm 0.033 \pm 1.000$	$5.046 \pm 0.184 \pm 1.000$
-0.15	$0.795 \pm 0.025 \pm 0.013$	$1.701 \pm 0.080 \pm 0.027$	$3.040 \pm 0.034 \pm 0.040$	$4.992 \pm 0.182 \pm 0.078$
-0.05	$0.841 \pm 0.026 \pm 0.000$	$1.715 \pm 0.081 \pm 0.000$	$2.978 \pm 0.033 \pm 1.000$	$4.906 \pm 0.179 \pm 1.000$
0.05	$0.817 \pm 0.026 \pm 0.023$	$1.649 \pm 0.078 \pm 0.021$	$2.998 \pm 0.034 \pm 0.061$	$4.910 \pm 0.179 \pm 0.060$
0.15	$0.809 \pm 0.025 \pm 0.000$	$1.684 \pm 0.079 \pm 0.000$	$3.034 \pm 0.034 \pm 1.000$	$5.009 \pm 0.183 \pm 1.000$
0.25	$0.846 \pm 0.026 \pm 0.030$	$1.713 \pm 0.080 \pm 0.010$	$2.981 \pm 0.033 \pm 0.064$	$4.921 \pm 0.180 \pm 0.042$
0.35	$0.779 \pm 0.025 \pm 0.000$	$1.716 \pm 0.081 \pm 0.000$	$2.928 \pm 0.037 \pm 1.000$	$4.901 \pm 0.179 \pm 1.000$
0.45	$0.833 \pm 0.072 \pm 0.026$	$1.598 \pm 0.077 \pm 0.006$	$2.797 \pm 0.035 \pm 0.079$	$4.736 \pm 0.174 \pm 0.004$
-0.45	$1.009 \pm 0.034 \pm 4.000$	$1.957 \pm 0.065 \pm 5.000$	$3.494 \pm 0.074 \pm 5.000$	$5.834 \pm 0.179 \pm 6.000$
-0.35	$1.014 \pm 0.043 \pm 0.304$	$2.018 \pm 0.081 \pm 0.396$	$3.558 \pm 0.078 \pm 0.506$	$6.033 \pm 0.186 \pm 0.432$
-0.25	$0.999 \pm 0.044 \pm 4.000$	$2.079 \pm 0.087 \pm 5.000$	$3.643 \pm 0.091 \pm 5.000$	$5.994 \pm 0.204 \pm 6.000$
-0.15	$1.015 \pm 0.055 \pm 0.313$	$2.033 \pm 0.083 \pm 0.284$	$3.594 \pm 0.090 \pm 0.469$	$6.015 \pm 0.239 \pm 0.498$
-0.05	$0.992 \pm 0.067 \pm 4.000$	$2.023 \pm 0.106 \pm 5.000$	$3.568 \pm 0.119 \pm 5.000$	$5.981 \pm 0.228 \pm 6.000$
0.05	$1.018 \pm 0.070 \pm 0.255$	$2.029 \pm 0.113 \pm 0.404$	$3.627 \pm 0.133 \pm 0.409$	$5.960 \pm 0.230 \pm 0.620$
0.15	$1.020 \pm 0.042 \pm 4.000$	$2.027 \pm 0.095 \pm 5.000$	$3.579 \pm 0.103 \pm 5.000$	$6.031 \pm 0.218 \pm 6.000$
0.25	$0.992 \pm 0.041 \pm 0.252$	$2.034 \pm 0.083 \pm 0.474$	$3.611 \pm 0.089 \pm 0.303$	$6.077 \pm 0.203 \pm 0.675$
0.35	$1.000 \pm 0.046 \pm 4.000$	$2.044 \pm 0.080 \pm 5.000$	$3.579 \pm 0.078 \pm 5.000$	$5.917 \pm 0.204 \pm 6.000$
0.45	$0.951 \pm 0.037 \pm 0.223$	$1.991 \pm 0.069 \pm 0.495$	$3.614 \pm 0.079 \pm 0.329$	$5.817 \pm 0.177 \pm 0.720$

Table A.8: Integrated yield of anti-proton (top) and proton (bottom) for different rapidity bins in 70-80%, 60-70%, 50-60%, 40-50% Au+Au collisions.

Rapidity	$30-40\%$	$20-30\%$	$10-20\%$	$5-10\%$	$0-5\%$
-0.45	$7.356 \pm 0.198 \pm 2.000$	$11.744 \pm 0.248 \pm 2.000$	$16.740 \pm 0.311 \pm 3.000$	$21.429 \pm 0.569 \pm 3.000$	$25.730 \pm 0.681 \pm 4.000$
-0.35	$7.590 \pm 0.202 \pm 0.035$	$11.979 \pm 0.252 \pm 0.128$	$17.241 \pm 0.315 \pm 0.072$	$22.759 \pm 0.600 \pm 0.189$	$27.372 \pm 0.721 \pm 0.141$
-0.25	$7.790 \pm 0.207 \pm 2.000$	$12.141 \pm 0.252 \pm 2.000$	$17.098 \pm 0.310 \pm 3.000$	$22.597 \pm 0.593 \pm 3.000$	$26.963 \pm 0.704 \pm 4.000$
-0.15	$7.739 \pm 0.205 \pm 0.070$	$12.013 \pm 0.249 \pm 0.112$	$17.053 \pm 0.309 \pm 0.125$	$22.645 \pm 0.592 \pm 0.205$	$26.621 \pm 0.695 \pm 0.145$
-0.05	$7.695 \pm 0.204 \pm 2.000$	$12.068 \pm 0.250 \pm 2.000$	$16.962 \pm 0.307 \pm 3.000$	$22.392 \pm 0.585 \pm 3.000$	$26.243 \pm 0.685 \pm 4.000$
0.05	$7.692 \pm 0.204 \pm 0.111$	$12.082 \pm 0.250 \pm 0.102$	$16.674 \pm 0.302 \pm 0.154$	$22.229 \pm 0.581 \pm 0.180$	$25.826 \pm 0.674 \pm 0.287$
0.15	$7.713 \pm 0.204 \pm 2.000$	$12.091 \pm 0.251 \pm 2.000$	$16.674 \pm 0.302 \pm 3.000$	$22.064 \pm 0.577 \pm 3.000$	$25.947 \pm 0.677 \pm 4.000$
0.25	$7.666 \pm 0.204 \pm 0.132$	$11.917 \pm 0.247 \pm 0.061$	$16.891 \pm 0.307 \pm 0.197$	$22.163 \pm 0.581 \pm 0.100$	$26.383 \pm 0.692 \pm 0.338$
0.35	$7.554 \pm 0.210 \pm 2.000$	$11.953 \pm 0.254 \pm 2.000$	$16.719 \pm 0.307 \pm 3.000$	$22.227 \pm 0.586 \pm 3.000$	$26.555 \pm 0.700 \pm 4.000$
0.45	$7.333 \pm 0.197 \pm 0.118$	$11.545 \pm 0.243 \pm 0.044$	$16.439 \pm 0.305 \pm 0.187$	$21.440 \pm 0.576 \pm 0.056$	$26.281 \pm 0.707 \pm 0.346$
-0.45	$9.232 \pm 0.233 \pm 6.000$	$14.689 \pm 0.312 \pm 7.000$	$20.973 \pm 0.405 \pm 7.000$	$28.032 \pm 0.740 \pm 8.000$	$33.506 \pm 0.890 \pm 8.000$
-0.35	$9.393 \pm 0.252 \pm 0.697$	$15.183 \pm 0.353 \pm 0.953$	$21.028 \pm 0.410 \pm 0.736$	$28.438 \pm 0.782 \pm 1.118$	$33.959 \pm 0.904 \pm 0.703$
-0.25	$9.471 \pm 0.265 \pm 6.000$	$15.130 \pm 0.357 \pm 7.000$	$21.437 \pm 0.430 \pm 7.000$	$28.459 \pm 0.843 \pm 8.000$	$33.776 \pm 0.920 \pm 8.000$
-0.15	$9.440 \pm 0.266 \pm 0.649$	$15.107 \pm 0.372 \pm 0.419$	$20.837 \pm 0.434 \pm 0.685$	$28.370 \pm 0.831 \pm 0.585$	$33.128 \pm 0.942 \pm 0.744$
-0.05	$9.346 \pm 0.296 \pm 6.000$	$14.732 \pm 0.385 \pm 7.000$	$20.574 \pm 0.469 \pm 7.000$	$27.711 \pm 0.861 \pm 8.000$	$32.462 \pm 0.986 \pm 8.000$
0.05	$9.453 \pm 0.291 \pm 0.618$	$14.898 \pm 0.389 \pm 0.762$	$20.699 \pm 0.472 \pm 0.764$	$27.711 \pm 0.874 \pm 0.755$	$31.910 \pm 0.973 \pm 0.783$
0.15	$9.484 \pm 0.272 \pm 6.000$	$14.977 \pm 0.367 \pm 7.000$	$20.697 \pm 0.432 \pm 7.000$	$28.191 \pm 0.853 \pm 8.000$	$32.379 \pm 0.899 \pm 8.000$
0.25	$9.565 \pm 0.276 \pm 0.403$	$14.917 \pm 0.360 \pm 0.740$	$21.045 \pm 0.428 \pm 0.280$	$28.528 \pm 0.820 \pm 0.745$	$33.264 \pm 0.904 \pm 0.353$
0.35	$9.467 \pm 0.251 \pm 6.000$	$15.175 \pm 0.352 \pm 7.000$	$21.003 \pm 0.417 \pm 7.000$	$28.028 \pm 0.782 \pm 8.000$	$33.478 \pm 0.893 \pm 8.000$
0.45	$9.125 \pm 0.240 \pm 0.209$	$14.522 \pm 0.323 \pm 0.796$	$20.983 \pm 0.393 \pm 0.754$	$27.275 \pm 0.758 \pm 0.615$	$33.263 \pm 0.874 \pm 0.590$

Table A.9: Integrated yield of anti-proton (top) and proton (bottom) for different rapidity bins in 30-40%, 20-30%, 10-20%, 5-10%, 0-5% Au+Au collisions.

Appendix B

Relativistic Kinematics

In relativistic heavy-ion collisions and in many other high-energy reaction processes, it is convenient to use kinematic variables which are Lorentz invariant under Lorentz 'boost' (a transformation with one of the three (x, y, z) Cartesian coordinate directions are employed as the reference axis for the transformation).

We use the natural units $c=\hbar=1$.

B.1 Lorentz Transformation

The space-time coordinates of a point x are denoted by a 4-vector: $x^\mu=(t, \overrightarrow{r})$. The 4-momentum of a particle of mass m is $p^\mu=(p^0, \overrightarrow{p})$, where $p^0=\sqrt{(\overrightarrow{p})^2+m^2}$ ($p^0=E$). The square of p^μ is $p^\mu p_\mu=(p^0)^2-(\overrightarrow{p})^2=m^2$. The velocity of the particle is $\beta=\overrightarrow{p}/E$. The 4-momentum viewed from a frame moving with a velocity β are given by

$$\begin{pmatrix} E^* \\ p^*_{/\!/} \end{pmatrix} = \begin{pmatrix} \gamma & \gamma\beta \\ -\gamma\beta & \gamma \end{pmatrix} \begin{pmatrix} E \\ p_{/\!/} \end{pmatrix}, \; p^*_t = p_t \tag{B.1}$$

where $\gamma=1/\sqrt{1-\beta^2}$, and p_t ($p_{/\!/}$) are the components of $\overrightarrow{p}$ perpendicular (parallel) to β. This transformation is called Lorentz transformation. Other 4-vectors can be transformed in the same manner.

B.2 Kinetic Variables

We Define z axis as the direction of the beam.

B.2.1 Transverse Momentum

The transverse momentum of a particle is defined as:

$$p_t = \sqrt{p_x^2 + p_y^2} \tag{B.2}$$

p_t is Lorentz invariant variable since both p_x and p_y are the two components of $p_{/\!/}$ which is unchanged under a Lorentz boost along z axis.

The transverse mass of a particle of mass m is defined as

$$m_t = \sqrt{p_t^2 + m^2} \tag{B.3}$$

and the transverse energy of the particle is given by $E_t = m_t - m$.

B.2.2 Rapidity

As the name implies, rapidity is related to the velocity. It is defined as

$$\begin{aligned} y &\equiv \frac{1}{2}\ln\left(\frac{E+p_z}{E-p_z}\right) \\ &= \ln\left(\frac{E+p_z}{m_t}\right) \\ &= \tanh^{-1}\left(\frac{p_z}{E}\right) \end{aligned} \tag{B.4}$$

where $p_z = p_{/\!/}$ is the longitudinal momentum of the particle. So rapidity is a scalar associated with the z axis.

Under a Lorentz transformation from a reference system S to a system S' moving with velocity β with respect to S in the longitudinal direction, the rapidity $y' = y - y_\beta$, where y' (y) is the rapidity in the S (S') frame and y_β is the rapidity of the moving frame.

$$y_\beta = \frac{1}{2}\ln\left(\frac{1+\beta}{1-\beta}\right) \tag{B.5}$$

B.2.3 Pseudorapidity

In the experiments, the detected particles are often not identified, and we do not know their masses which are required to determine the rapidity. However, the momentum and the dip angle θ of the detected particles relative to the z axis are known. In this case, it is convenient to the pseudorapidity variable as defined as:

$$\begin{aligned} \eta &= -\ln(\tan(\theta/2)) \\ &= \frac{1}{2}\ln\left(\frac{p+p_z}{p-p_z}\right). \end{aligned} \tag{B.6}$$

Compare with Eq. B.4, it is easy to see that η coincides with y when the momentum is large, that is, when $p \approx E$.

B.3 Jacobian Effect

By comparing Eq. B.4 and Eq. B.6, it is easy to see that for massless particles, $y = \eta$, and for particles with large momenta $(\beta \approx 1)$, $y \approx \eta$.

From Eq. B.4 and Eq. B.6, we can also get following relations:

$$p_z = m_t \sinh y, \;\; E = m_t \cosh y \tag{B.7}$$

and

$$p_z = p_t \sinh\eta,\ \ p = p_t \cosh\eta. \tag{B.8}$$

If the particles have a distribution $dN/dy\,dp_t$ in terms of the rapidity, then the distribution in the pseudorapidity is

$$\frac{\mathrm{dN}}{\mathrm{d}\eta\,\mathrm{dp_t}} = \sqrt{1-\frac{m^2}{m_t^2\cosh^2 y}}\,\frac{\mathrm{dN}}{\mathrm{dy\,dp_t}} \tag{B.9}$$

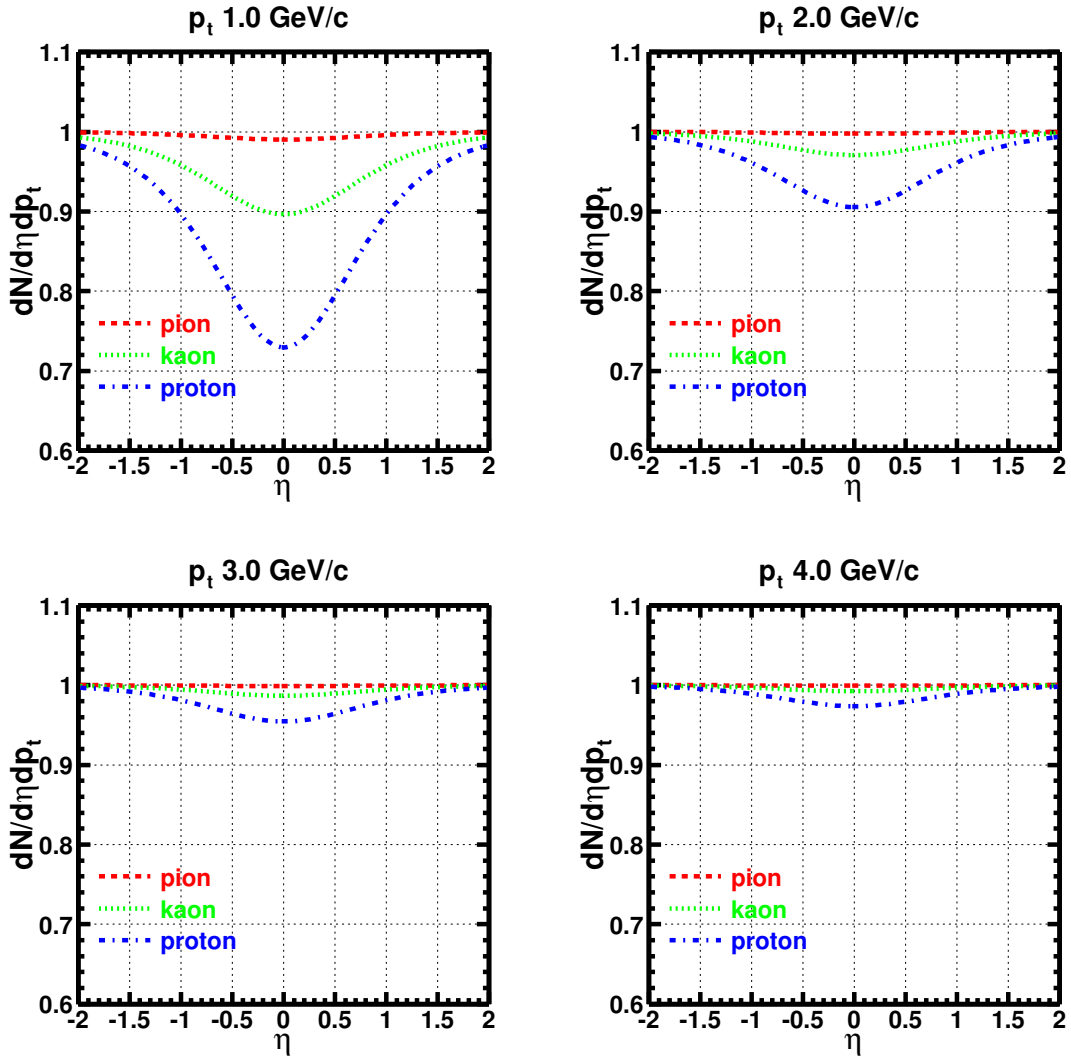

Figure B.1: Effects of the Jacobian transformations from rapidity density distributions to pseudorapidity density distributions for pion, kaon and proton in selected p_t.

The above expression is a Jacobian transformation. From Eq. B.9 we can also see that the Jacobian factor depends on the particle mass and/or p_t. The effects are shown in Fig. B.1. We assume a flat unit $dN/dy\,dp_t$ distributions within $-2 < y < 2$ for particle pion, kaon and proton in selected $p_t = 1, 2, 3, 4$ GeV/c, then compute

the corresponding $dN/d\eta\, dp_t$ distributions as the curves in Fig. B.1. The largest difference occurs in the most central rapidity region, for the heaviest particle, and at the lowest p_t. The effect is less than 10% event for protons when $p_t > 2$ GeV/c.

B.4 Phase Space and Invariant Yield

The differential yields are corresponding to the number of particles emitted into a particular region in momentum space per interaction. It is nature to refer to an object such as d^3N/dp^3. The total yield of a particular particle is the total number of such particles emitted into any point in momentum space per interaction,

$$N = \int \frac{d^3N}{dp^3} d^3p \tag{B.10}$$

which intuitively must be Lorentz invariant. However, the momentum-space volume element, d^3p, is not invariant since the differential momentum element along the direction of a boost between frames transforms as $dp' = \gamma dp$. We must be careful to state the frame in which they are measured when report the differential yields as in Eq. B.10. Also, we would have to explicitly transform the differential yields when comparing the results from different experiments.

Such complexities can be avoided if we can find an expression for the differential yield which is manifestly invariant. Such expression do exist as discussed in Appendix B of [130]. The expression for total yields can be written as:

$$N = \int \frac{d^3N}{2\pi p_t\, dp_t\, dy} 2\pi p_t\, dp_t\, dy, \qquad p_t\, dp_t = m_t\, dm_t \tag{B.11}$$

The integrand of Eq. B.11 is Lorentz invariant for boosts along the collision axis since N is dimensionless and p_t, dp_t, and dy are invariant for such boosts. With y and p_t defined relative to the boost axis, the expression is invariant for boost in any direction.

Appendix C

Mini Computing Farm at IOPP

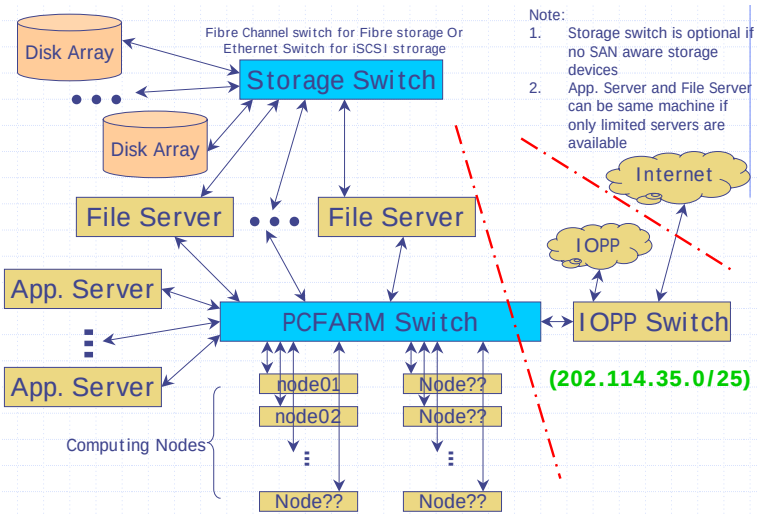

Figure C.1: The schematic diagram of the local computing farm.

Have a local computing environment is very necessary and important! There are several reasons. First, the network speed between China and U.S.A. is too slow to develop programs and check the results via remote connection. Doing the analysis work in local environment is faster. Second, the local computing environment provides a good place for the new students to learn the software and understand the computing details, so they can move to the physics analysis quickly. Have the local computing environment with similar hardware and software configuration as in RCF [92, 93][1] can make the maintenance of the system and especially the synchronization of the software very easy. However, it's not possible to have identical configuration as RCF, we need to cope with the local specific features!

The base line of a good design and implemented farm is running stable. Then the user can use the farm easily and conveniently. The administrators can also easily administrate and maintain the system, locate and solve the problem fast whenever something wrong. In the following two sections I'll describe the details

[1] http://www.rhic.bnl.gov/RCF/

about the design and implementation of the local farm under such requirement. I'll first discuss the hardware briefly and then the software in detail. This farm can be easily adapted to other purpose farm too. For example, the implementation of BESIII[2] online test farm [132] is based on the idea presented here.

The schematic diagram of the farm is show in Fig. C.1.

C.1 Hardware

The hardware subsystem of the local farm can be categorized as network, storage device, file servers, analysis nodes, backup device, etc.

The network fabric of the farm consists of a two-stack ethernet switch (other technology such as Myrinet[3] can be used too, that's depend on the specific computing requirements) with two Gb ports and 48 100Mb ports. Gb ports are connected with the file servers because of the large data transfer from them. The 100Mb ports are connected with the analysis nodes. In general, the network should base on at least Layer-2 switch. Layer-3 switch can be used for large farm, so one can isolate the server and analysis nodes by VLAN (Virtual Local Area Network) division. The selection of the port speed is depend on the services of the computer provided. For file servers, network should not be a bottleneck, so a fast port is best.

All the data files and users' files are stored in the storage devices, generally the disk arrays. Raid 5 is applied to the array to ensure the stability and better performance. Both Directed Attach Storage (DAS) and Network Attach Storage (NAS) are used in this local farm. SAN (Storage Area Network)[4] is another good choice which only available if have enough budget. However, by employing a Fibre Channel array connected with a server with a HBA (Host Bus Adapter) can provide a chance to upgrade to SAN easily later.

All the file servers and analysis nodes are Intel[5] X86 based PC. Other architecture can be used too if there are strong software support. Each PC is equipped with at least 2 processors, 1GB memory, a NIC card (better if w/ PXE[6] boot available) and local disk. One can reach each PC through a KVM (Keyboard/Video/Mouse) switch which is connected with all the PCs. The detail hardware configuration can be varied and can be easily scaled as the requirement change.

A DLT7000 tape driver is connected with one of the file servers. This made the backup and transfer of large important data possible. Again, a tape library (such as HPSS[7]) is possible only with enough budget.

In general, there are less thing can tunable for hardware devices compare to the software. So we should choose stable hardware at the very start. Both the performance of the hardware and the services provided by the vendor should be carefully considered before making decision. Otherwise, it will be the biggest impact to the stabilization of the farm!

[2] http://bes.ihep.ac.cn/bes3/index.html

[3] http://www.myri.com/

[4] http://www.snia.org/

[5] http://www.intel.com

[6] Preboot Execution Environment (PXE) Specification, v2.1, Intel Corporation

[7] http://www4.clearlake.ibm.com/hpss/index.jsp

C.2 Software

The first item on software is the choose of the operating system. The candidates are limited, however. Only Windows[8] or UNIX[9], indeed. Windows is discard because of non-free and the limited software support in HEP field.

Although there are many variants of UNIX, Linux[10] and Solaris[11] are the operating systems supported by most of the high-energy physics experiments. However, Linux is playing more and more important role because of its free of charge and high performance. In this local farm, except a SUNE450 server is running Solaris, all the other PCs are running Linux. Also, there are many free software[12] available.

C.2.1 System Installation

The installation of the operating system for a cluster is boring and tedious. Fortunately, there are many technologies available which can be combined to solve this problem, such as kickstart[13], Intl Preboot Execution Environment (PXE), DHCP[14], SystemImager[15]. Following are the detail procedures used for the installation of this farm. Please note they are based on RedHat[16] distribution, for other distributions, the path location etc. may be different. Also, consult the manual for the details of the software used.

Collect the MAC address

This procedure is only available for the PC which can support PXE boot. So for a bare system, one can reboot the PC w/ PXE boot, then the pc will send out the DHCP query trying to get an ip (The IP addresses for this farm are taken from the three reserved blocks of the addresses as defined by IANA (Internet Assigned Numbers Authority) in RFC[17] 3330: 10.0.0.0/8, 172.16.0.0/12 and 192.168.0.0/16) address from the DHCP server, corresponding, the Media Access Control (MAC) address will show during this stage. For computer w/o PXE available, one can only get the address from a running operating system. Boot the system with the RedHat Linux CD to rescue mode is one possible solution.

Setup the first server

[8] http://www.microsoft.com/windows/
[9] http://www.unix.org/
[10] http://www.kernel.org/
[11] http://www.sun.com/solaris/
[12] http://www.gnu.org/,http://www.sourceforge.net, ...
[13] /usr/share/doc/anaconda-x.x/kickstart-docs.txt
[14] http://www.dhcp.org
[15] http://www.systemimager.org
[16] http://www.redhat.com
[17] http://www.rfc-editors.org

Install Linux on this server with normal procedure. A suggested partition layout is listed in Table C.1. For the partition type, Logical Volume Management (LVM[18]) can be used, so we can change the space of specific partition easily!

All the site specific software will be installed in the AFS area after the AFS server is set up.

Create file */etc/dhcpd.conf* and config the DHCP server to allocate ip address based on MAC address. Then edit */etc/pxe.conf* to add corresponding boot item to the server. Install SystemImager server software on this server too.

Put a copy of the RedHat install CD on the server, and export this directory to NFS clients.

Create kickstart file

Create a kickstart config file with custom configuration, and put it on some place where can be reached by the client, such as the web area. The configuration depends on the type of the machine to be installed.

Setup all the other servers

If there are any other servers, install all of them use the kickstart method. For example, after the install cd or PXE boot the system, a prompt will display and wait for user input. One can type *linux ks=http://xxx/ks.cfg* (where xxx can be ip address or host name of the server where the file is stored in), the rest of the setup will be done automatically.

Setup the first client

Install the first client use the same method as previous step. Install all the necessary software on this system, and configure the client to be a full production system. Set up SystemImager client on this client, and prepare this client available to be fetched as an image.

Prepare the image

Switch to the server with SystemImager server installed, fetch the image from the just configured client.

Setup all the other clients

Boot all other clients from PXE, select the boot item with SystemImager. All the rest will be done automatically. For system without PXE, one can made a bootable floppy disk or cdrom with SystemImager.

With this method, except for the servers which need to configure for different purpose, all the clients can be kept in synch easily.

C.2.2 Base Services Configuration

Domain Name Service (DNS)[19] is installed to provide resolution of the machines' name and ip address. We use the most popular software BIND[20]. To keep

[18] http://sources.redhat.com/lvm2/

[19] http://www.dns.net/dnsrd/

[20] http://www.isc.org/sw/bind/

Mount point	MBytes	comment
swap	1024	first partition if possible
/	512	
/usr	5120	
/var	2048	
/tmp[1]	>1024	
/usr/vice/cache	512	if afs client
/vicepa	>10240	if afs server
/home or /u	limited by disk space	maximum

[1] on client nodes where usage of /tmp might large, /tmp can be set as a symbol link to the free space available.

Table C.1: Suggested partition layout for Linux

the system friendly to user, a DNS alias is setup for all the available interactive nodes. So user only need to remember this name to access the farm.

It's very important to keep the system time in synch for a large cluster, otherwise some software such as make[21] will not work correctly. NTP (Network Time Protocol)[22] service is installed for this purpose.

System log is very useful for the regular maintenance of the system and the diagnosis in case of something wrong. However, it's not wise to login into every PC in the farm to check them. So one of the servers is configured as a log server which can accept log information coming from the network, the other machines will then write the log information to this configured server. Thus, one can get all the log information from only one place!

Email services are provided too. However, it's not necessary to provide a formal email service on this local farm. So this service are configured as all the email message will be passed to the formal email server of the institution and then passed to the user's formal email address.

Web services (provided by Apache[23]) is set up on the farm to provide information such as the system status and usage statistics to the users. Some kind of administer interfaces are provided too. For instance, LDAP and MySQL database can be managed by phpLDAPadmin[24] and phpMyadmin[25] from the web.

The security of the system is another very important topic for today's computer system. Iptables[26] is the built-in firewall in Linux kernel. All the machines in the farm are configured to limit access from outside. Only the specified services

[21] http://www.gnu.org/software/make/
[22] http://www.ntp.org/
[23] http://www.apache.org
[24] http://phpldapadmin.sourceforge.net/
[25] http://www.phpmyadmin.net/home_page/
[26] http://www.netfilter.org/

are opened for outside. For cluster with Layer-3 switch available, one can also configure a firewall on the L3 switch to enforce the security.

NIS is a name service for UNIX directories like the passwd map, ethers map, etc. NIS is easy to setup and administer, scales reasonably well, is supported by nearly all forms of UNIX, and is thus very popular. Unfortunately, it is also completely insecure. Weakly encrypted passwords, as well as everything else, are sent over the network in the clear. NIS is difficult to firewall. Clients have no way to ensure that the server they are talking to is actually an official server. The Lightweight Directory Access Protocol (LDAP)[27] was designed as a way to access directories containing all matter of information. All the information stored in NIS (user ids, group ids, home directories, autofs maps etc.) can be stored in LDAP database. Users with different roles can access the information they needed. All the information are stored in a central database. It support pretty good security through SSL[28] for authentication and transport encryption, fine grained access controls, etc.

Although we can store the encrypted passwords in LDAP and access the databases through SSL, but it's still not a good idea to store the private information into a directory which is designed to hold public data. Kerberos[29] is designed to solve this problem. Kerberos is useful for securing NFS (in NFSv4) too.

In this local farm, LDAP+Kerberos are chosen as the user authentication system.

C.2.3 File Services

All the unused space of the local disk on the computing nodes are used as scratch area. User's can put their temporary data here.

NFS is by far the most widely used file services used in the cluster systems. Generally, large amount of the data and user's files are stored on NFS area. The mount/umount of the NFS file system is controlled by automount.

AFS[30] is another distributed file system. It's not suit for large data transfer, however. But it can be used to store the software, which are accessed and write not so frequently. Another advantage of AFS is that it can make the software for different system version transparent to the user. This is done by a sys variable, which will point to the system used. All the software we used are stored on the AFS server using the same directory structure. From the user's point, there are no difference between this local farm and RCF when using the software.

There are also some other kinds of file system solutions available which are specific to SAN environment, such as Open Global File System (OpenGFS)[31] or GFS[32] from RedHat and GPFS[33] from IBM.

Besides these kind of centralized disk model, STAR is using distributed disk

[27] http://www.openldap.org
[28] http://www.openssl.org/
[29] http://web.mit.edu/kerberos/www/
[30] http://www.openafs.org
[31] http://opengfs.sourceforge.net/
[32] http://sources.redhat.com/cluster/gfs/
[33] http://www.ibm.com/servers/eserver/clusters/software/gpfs.html

model too. By combining with use of the Scheduler[34] software and the FileCatalog database, the files can be accessed from local nodes too. Also, there are many other different kind of object-based storage solution available too, such as Lustre[35], ActiveScale[36]. More investigations and tests are needed before adopting them.

A Samba[37] server is set up on the farm to enable the user of windows operating system access their files directly.

C.2.4 Batch System and Parallel Processing

In the field of high-energy physics experiment, the data volume is very large because of the statistics purpose. In general, there are millions of events to be processed, the procedure to process each event is the same. The difficulty here is just the large scale. Thus, a batch system is appropriate for the farm. LSF[38] from platform computing corporation is a good choice, but the price is too high for the small farm. Fortunately, there are many other open source batch system available. Such as OpenPBS[39]+Maui[40], SGE[41], Condor[42]. For this farm, these three software are installed for comparison. Also, to prepare a possible upgrade to a member of a grid, and to make full use of the available computing resource in the local institutions, Globus[43] is set up for test too.

Parallel processing has emerged as a key enabling technology in modern computing. The main idea is to have many small tasks to solve one large problem. Currently, there are two major developments: massively parallel processors (MPPs) and the widespread use of distributed computing. MPPs are based on the hardware level: a few hundred to a few thousand CPUs were combined in a single large cabinet connected to hundreds of gigabytes of memory. So generally, MPPs cost too much! Distributed computing is the second major development. It is a process whereby a set of computers connected by a network are used collectively to solve a single large problem. As many general-purpose workstations (or MPPs) are connected with the high-speed local area networks, the combined computational resources may exceed the power of a single high-performance computer. Distributed computing is based on software level. PVM[44] (Parallel Virtual Machine) and MPI[45] (Message Passing Interface) are two of the most popular packages used. They are all come with the Linux distribution (RedHat) we used.

[34] http://www.star.bnl.gov/STAR/comp/Grid/scheduler/index.html
[35] http://www.clusterfs.com/
[36] http://www.panasas.com/activescaleos.html
[37] http://www.samba.org/
[38] http://www.platform.com
[39] http://www.openpbs.org
[40] http://www.clusterresources.com/products/maui/
[41] http://gridengine.sunsource.net/
[42] http://www.cs.wisc.edu/condor/
[43] http://www.globus.org/
[44] http://www.csm.ornl.gov/pvm/pvm_home.html
[45] http://www-unix.mcs.anl.gov/mpi/

C.2.5 Monitoring and Administration

To keep the system under control, several monitoring functions are implemented. Both "mon"[46] program and "nagios"[47] can be used to monitor the availability of different kinds of services. Once a failure is detected, an email will be sent out to the administrator. We chosen nagios for this farm.

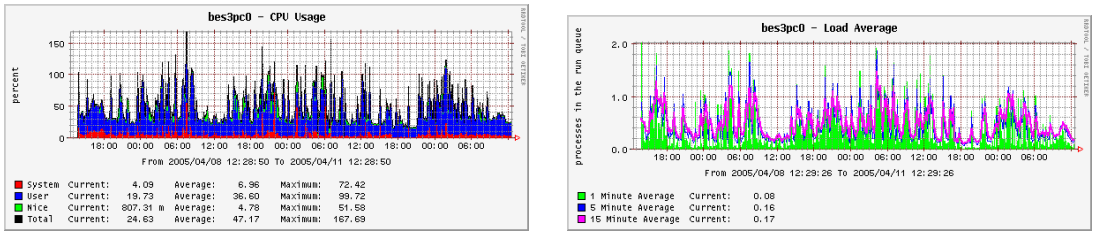

Figure C.2: Farm system status statistics.

Have the whole system's usage and status available can provide a base for further decision on the upgrade of the farm. SNMP+MRTG[48] can provide the usage statistics of the system, such as CPU load, network traffic, memory usage, disk usage etc. Orca[49] can be used to collect more detailed status of the machines too. Ganglia[50] is another open-source tool which have the same function. Recently, we found another software Cacti[51] which can provide more advanced and flexible graphing functionality by using the power of RRDTool[52] and SNMP. We'll finally employ Cacti as the detail usage and statistical interface and Ganglia as a auxiliary interface because of its easy to installed and configured. Awstats[53] is used for the web and email usage statistics, it can be applied to other statistics too. All these statistical data are stored in the web server. Administrators or users can get the status of the system quickly. See Fig. C.2 for an example.

C.2.6 User Support

The discussion of above are all focused on the system administrator's side. To make full use of the farm, it's important to provide training to the user! However, this is not a easy task. We try to implement this by setup a Groupware and Content Management System (CMS) using a Wiki software: tikiwiki[54]. Both system administrators and users can post their experiences of using the farm on the web and clean them up as FAQs (Frenquently Asked Questions). The system also provide a forum where users can discuss conveniently.

[46] http://www.kernel.org/pub/software/admin/mon
[47] http://www.nagios.org
[48] http://www.mrtg.org/
[49] http://www.orcaware.com/orca
[50] http://ganglia.sourceforge.net
[51] http://www.cacti.net
[52] http://www.rrdtool.org/
[53] http://awstats.sourceforge.net/
[54] http://tikiwiki.org

Appendix D

STAR Collaboration

J. Adams[3], M.M. Aggarwal[29], Z. Ahammed[43], J. Amonett[20], B.D. Anderson[20], D. Arkhipkin[13], G.S. Averichev[12], S.K. Badyal[19], Y. Bai[27], J. Balewski[17], O. Barannikova[32], L.S. Barnby[3], J. Baudot[18], S. Bekele[28], V.V. Belaga[12], R. Bellwied[46], J. Berger[14], B.I. Bezverkhny[48], S. Bharadwaj[33], A. Bhasin[19], A.K. Bhati[29], V.S. Bhatia[29], H. Bichsel[45], A. Billmeier[46], L.C. Bland[4], C.O. Blyth[3], B.E. Bonner[34], M. Botje[27], A. Boucham[38], A.V. Brandin[25], A. Bravar[4], M. Bystersky[11], R.V. Cadman[1], X.Z. Cai[37], H. Caines[48], M. Calderón de la Barca Sánchez[17], J. Castillo[21], D. Cebra[7], Z. Chajecki[44], P. Chaloupka[11], S. Chattopdhyay[43], H.F. Chen[36], Y. Chen[8], J. Cheng[41], M. Cherney[10], A. Chikanian[48], W. Christie[4], J.P. Coffin[18], T.M. Cormier[46], J.G. Cramer[45], H.J. Crawford[6], D. Das[43], S. Das[43], M.M. de Moura[35], A.A. Derevschikov[31], L. Didenko[4], T. Dietel[14], S.M. Dogra[19], W.J. Dong[8], X. Dong[36], J.E. Draper[7], F. Du[48], A.K. Dubey[15], V.B. Dunin[12], J.C. Dunlop[4], M.R. Dutta Mazumdar[43], V. Eckardt[23], W.R. Edwards[21], L.G. Efimov[12], V. Emelianov[25], J. Engelage[6], G. Eppley[34], B. Erazmus[38], M. Estienne[38], P. Fachini[4], J. Faivre[18], R. Fatemi[17], J. Fedorisin[12], K. Filimonov[21], P. Filip[11], E. Finch[48], V. Fine[4], Y. Fisyak[4], K. Fomenko[12], J. Fu[41], C.A. Gagliardi[39], J. Gans[48], M.S. Ganti[43], L. Gaudichet[38], F. Geurts[34], V. Ghazikhanian[8], P. Ghosh[43], J.E. Gonzalez[8], O. Grachov[46], O. Grebenyuk[27], D. Grosnick[42], S.M. Guertin[8], Y. Guo[46], A. Gupta[19], T.D. Gutierrez[7], T.J. Hallman[4], A. Hamed[46], D. Hardtke[21], J.W. Harris[48], M. Heinz[2], T.W. Henry[39], S. Hepplemann[30], B. Hippolyte[48], A. Hirsch[32], E. Hjort[21], G.W. Hoffmann[40], H.Z. Huang[8], S.L. Huang[36], E.W. Hughes[5], T.J. Humanic[28], G. Igo[8], A. Ishihara[40], P. Jacobs[21], W.W. Jacobs[17], M. Janik[44], H. Jiang[8], P.G. Jones[3], E.G. Judd[6], S. Kabana[2], K. Kang[41], M. Kaplan[9], D. Keane[20], V.Yu. Khodyrev[31], J. Kiryluk[22], A. Kisiel[44], E.M. Kislov[12], J. Klay[21], S.R. Klein[21], A. Klyachko[17], D.D. Koetke[42], T. Kollegger[14], M. Kopytine[20], L. Kotchenda[25], M. Kramer[26], P. Kravtsov[25], V.I. Kravtsov[31], K. Krueger[1], C. Kuhn[18], A.I. Kulikov[12], A. Kumar[29], C.L. Kunz[9], R.Kh. Kutuev[13], A.A. Kuznetsov[12], M.A.C. Lamont[48], J.M. Landgraf[4], S. Lange[14], F. Laue[4], J. Lauret[4], A. Lebedev[4], R. Lednicky[12], S. Lehocka[12], M.J. LeVine[4], C. Li[36], Q. Li[46], Y. Li[41], S.J. Lindenbaum[26], M.A. Lisa[28], F. Liu[47], L. Liu[47], Q.J. Liu[45], Z. Liu[47], T. Ljubicic[4], W.J. Llope[34], H. Long[8], R.S. Longacre[4], M. Lopez-Noriega[28], W.A. Love[4], Y. Lu[47], T. Ludlam[4], D. Lynn[4], G.L. Ma[37], J.G. Ma[8], Y.G. Ma[37], D. Magestro[28], S. Mahajan[19], D.P. Mahapatra[15], R. Majka[48], L.K. Mangotra[19], R. Manweiler[42], S. Margetis[20], C. Markert[48], L. Martin[38], J.N. Marx[21], H.S. Matis[21], Yu.A. Matulenko[31], C.J. McClain[1], T.S. McShane[10], F. Meissner[21], Yu. Melnick[31], A. Meschanin[31], M.L. Miller[22], Z. Milosevich[9], N.G. Minaev[31], C. Mironov[20], A. Mischke[27], D.K. Mishra[15], J. Mitchell[34], B. Mohanty[43], L. Molnar[32], C.F. Moore[40], D.A. Morozov[31], M.G. Munhoz[35], B.K. Nandi[43], S.K. Nayak[19], T.K. Nayak[43], J.M. Nelson[3], P.K. Netrakanti[43], V.A. Nikitin[13], L.V. Nogach[31], S.B. Nurushev[31], G. Odyniec[21], A. Ogawa[4], V. Okorokov[25], M. Oldenburg[21], D. Olson[21], S.K. Pal[43], Y. Panebratsev[12], S.Y. Panitkin[4], A.I. Pavlinov[46], T. Pawlak[44], T. Peitzmann[27], V. Perevoztchikov[4], C. Perkins[6], W. Peryt[44], V.A. Petrov[13], S.C. Phatak[15], R. Picha[7], M. Planinic[49], J. Pluta[44], N. Porile[32], J. Porter[45], A.M. Poskanzer[21], M. Potekhin[4], E. Potrebenikova[12], B.V.K.S. Potukuchi[19], D. Prindle[45], C. Pruneau[46], J. Putschke[23], G. Rakness[30], R. Raniwala[33], S. Raniwala[33], O. Ravel[38], R.L. Ray[40], S.V. Razin[12], D. Reichhold[32], J.G. Reid[45], G. Renault[38], F. Retiere[21], A. Ridiger[25], H.G. Ritter[21], J.B. Roberts[34], O.V. Rogachevskiy[12], J.L. Romero[7], A. Rose[46], C. Roy[38], L. Ruan[36], R. Sahoo[15], I. Sakrejda[21], S. Salur[48], J. Sandweiss[48], I. Savin[13], P.S. Sazhin[12], J. Schambach[40], R.P. Scharenberg[32], N. Schmitz[23], K. Schweda[21], J. Seger[10], P. Seyboth[23], E. Shahaliev[12], M. Shao[36], W. Shao[5], M. Sharma[29], W.Q. Shen[37], K.E. Shestermanov[31], S.S. Shimanskiy[12], E Sichtermann[21], F. Simon[23], R.N. Singaraju[43], G. Skoro[12], N. Smirnov[48], R. Snellings[27], G. Sood[42], P. Sorensen[21], J. Sowinski[17], J. Speltz[18], H.M. Spinka[1], B. Srivastava[32], A. Stadnik[12], T.D.S. Stanislaus[42], R. Stock[14], A. Stolpovsky[46], M. Strikhanov[25], B. Stringfellow[32], A.A.P. Suaide[35], E. Sugarbaker[28], C. Suire[4], M. Sumbera[11], B. Surrow[22], T.J.M. Symons[21], A. Szanto de Toledo[35], P. Szarwas[44], A. Tai[8], J. Takahashi[35],

A.H. Tang[27], T. Tarnowsky[32], D. Thein[8], J.H. Thomas[21], S. Timoshenko[25], M. Tokarev[12], T.A. Trainor[45], S. Trentalange[8], R.E. Tribble[39], O.D. Tsai[8], J. Ulery[32], T. Ullrich[4], D.G. Underwood[1], A. Urkinbaev[12], G. Van Buren[4], M. van Leeuwen[21], A.M. Vander Molen[24], R. Varma[16], I.M. Vasilevski[13], A.N. Vasiliev[31], R. Vernet[18], S.E. Vigdor[17], Y.P. Viyogi[43], S. Vokal[12], S.A. Voloshin[46], M. Vznuzdaev[25], W.T. Waggoner[10], F. Wang[32], G. Wang[20], G. Wang[5], X.L. Wang[36], Y. Wang[40], Y. Wang[41], Z.M. Wang[36], H. Ward[40], J.W. Watson[20], J.C. Webb[17], R. Wells[28], G.D. Westfall[24], A. Wetzler[21], C. Whitten Jr.[8], H. Wieman[21], S.W. Wissink[17], R. Witt[2], J. Wood[8], J. Wu[36], N. Xu[21], Z. Xu[4], Z.Z. Xu[36], E. Yamamoto[21], P. Yepes[34], V.I. Yurevich[12], Y.V. Zanevsky[12], H. Zhang[4], W.M. Zhang[20], Z.P. Zhang[36], P.A Zolnierczuk[17], R. Zoulkarneev[13], Y. Zoulkarneeva[13], and A.N. Zubarev[12]

[1] *Argonne National Laboratory, Argonne, Illinois 60439*
[2] *University of Bern, 3012 Bern, Switzerland*
[3] *University of Birmingham, Birmingham, United Kingdom*
[4] *Brookhaven National Laboratory, Upton, New York 11973*
[5] *California Institute of Technology, Pasedena, California 91125*
[6] *University of California, Berkeley, California 94720*
[7] *University of California, Davis, California 95616*
[8] *University of California, Los Angeles, California 90095*
[9] *Carnegie Mellon University, Pittsburgh, Pennsylvania 15213*
[10] *Creighton University, Omaha, Nebraska 68178*
[11] *Nuclear Physics Institute AS CR, Řež/Prague, Czech Republic*
[12] *Laboratory for High Energy (JINR), Dubna, Russia*
[13] *Particle Physics Laboratory (JINR), Dubna, Russia*
[14] *University of Frankfurt, Frankfurt, Germany*
[15] *Institute of Physics, Bhubaneswar 751005, India*
[16] *Indian Institute of Technology, Mumbai, India*
[17] *Indiana University, Bloomington, Indiana 47408*
[18] *Institut de Recherches Subatomiques, Strasbourg, France*
[19] *University of Jammu, Jammu 180001, India*
[20] *Kent State University, Kent, Ohio 44242*
[21] *Lawrence Berkeley National Laboratory, Berkeley, California 94720*
[22] *Massachusetts Institute of Technology, Cambridge, MA 02139-4307*
[23] *Max-Planck-Institut für Physik, Munich, Germany*
[24] *Michigan State University, East Lansing, Michigan 48824*
[25] *Moscow Engineering Physics Institute, Moscow Russia*
[26] *City College of New York, New York City, New York 10031*
[27] *NIKHEF, Amsterdam, The Netherlands*
[28] *Ohio State University, Columbus, Ohio 43210*
[29] *Panjab University, Chandigarh 160014, India*
[30] *Pennsylvania State University, University Park, Pennsylvania 16802*
[31] *Institute of High Energy Physics, Protvino, Russia*
[32] *Purdue University, West Lafayette, Indiana 47907*
[33] *University of Rajasthan, Jaipur 302004, India*
[34] *Rice University, Houston, Texas 77251*
[35] *Universidade de Sao Paulo, Sao Paulo, Brazil*
[36] *University of Science & Technology of China, Anhui 230027, China*
[37] *Shanghai Institute of Applied Physics, Shanghai 201800, China*
[38] *SUBATECH, Nantes, France*
[39] *Texas A&M University, College Station, Texas 77843*
[40] *University of Texas, Austin, Texas 78712*
[41] *Tsinghua University, Beijing 100084, China*
[42] *Valparaiso University, Valparaiso, Indiana 46383*
[43] *Variable Energy Cyclotron Centre, Kolkata 700064, India*
[44] *Warsaw University of Technology, Warsaw, Poland*
[45] *University of Washington, Seattle, Washington 98195*
[46] *Wayne State University, Detroit, Michigan 48201*
[47] *Institute of Particle Physics, CCNU (HZNU), Wuhan 430079, China*
[48] *Yale University, New Haven, Connecticut 06520*
[49] *University of Zagreb, Zagreb, HR-10002, Croatia*

Bibliography

[1] J.J. Thomas, Phil. Mag. **44**, 293 (1897).

[2] E. Rutherford, Phil. Mag. **21**, 669 (1911); Phil. Mag. **27**, 488 (1914).

[3] M. Gell-Mann, Phys. Letters **8**, 214 (1964).

[4] G. Zweig, CERN preprints Th. 401 and 412 (1964).

[5] M. Breidenbach *et al.*, Phys. Rev. Lett. **23**, 935 (1969).

[6] R. P. Feynman, Phys. Rev. Lett. **23**, 1415 (1969). in *Proceedings of the III International Conference on High Energy Collisions*, organized by C.N. Yang, J.A. Cole, M. Good, R. Hwa, and J. Lee-Franzini (Gordon and Breach, New York), p. 237.

[7] J.C. Pati *et al.*, Phys. Lett. **59B**, 265 (1975); J.C. Pati *et al.*, Nucl. Phys. B **185**, 416 (1981); C.S. Kalman, Proceedings of beach2004, [arXiv:hep-ph:0411313], and references therein.

[8] H. Harari, Phys. Lett. **86B**, 83 (1979).

[9] Nuclear Physics Panel. *et al.*, Nuclear Physics *(Physics Through the 1990s)*, National Academy Press, Washington D.C. (1986), 中文版：原子核物理学，科学出版社，北京, (1994).

[10] H. Fritzsch, Quarks: the Stuff of matter, Basic Books Inc., New York (1983), 中文版：夸克，物质的基元，高等教育出版社，北京, (1988).

[11] Elementary-Particle Physics Panel. *et al.*, Elementary-Particle Physics *(Physics Through the 1990s)*, National Academy Press, Washington D.C. (1986), 中文版：基本粒子物理学，科学出版社，北京, (1992).

[12] Committee on Elementary-Particle Physics *et al.*, Elementary-Particle Physics *(Revealing the Secrets of Energy and Matter)*, National Academy Press, Washington D.C. (1998).

[13] D. J. Gross and F. Wilczek, Phys. Rev. Lett. **30**, 1343 (1973).

[14] H. D. Politzer, Phys. Rev. Lett. **30**, 1346 (1973).

[15] D. J. Gross, Nucl. Phys. B (Proc. Suppl.) **74**, 426 (1999).

[16] Helmut Satz, Rep. Prog. Phys. **63**, 1511-1574 (2000); [arXiv:hep-ph/0007069].

[17] S. Bethke, J. Phys. G: Nucl. Part. Phys. **26**, R27 (2000); [arXiv:hep-ex/0004021].

[18] PDG group, Phys. Rev. D **66**, 010001 (2002); Phys. Lett. B **592**, 1 (2004).

[19] C. D. DeTar and J. F. Donoghue, Ann. Rev. Nucl. Part. Sci. **33**, 235 (1983); L. Wilets, *Bag Model of Nucleus*, World Scientific, Singapore, (1989).

[20] Frithjof Karsch, Nucl. Phys. A **698**, 199c (2002); [arXiv:hep-ph/0103314].

[21] Zoltán Fodor, Nucl. Phys. A **715**, 319 (2003); [arXiv:hep-lat/0209101].

[22] U. W. Heinz, AIP Conf. Proc. **602**, 281 (2001); [arXiv:hep-ph/0109006].

[23] Simon Hands, Contemp. Phys. **42**, 209 (2001); [arXiv:physics/0105022].

[24] J. D. Bjørken, Phys. Rev. D **27**, 140 (1983).

[25] Jens Berger, Ph.D. Thesis, University of Frankfurt, (2003).

[26] B. Müller, The Physics of the Quark Gluon Plasma, Lecture Notes in Physics, Vol. 225, Springer, Berlin, (1985).

[27] C.Y. Wong, Introduction to High-Energy Heavy-Ion Collisions, World Scientific, Singapore (1994).

[28] Jean Letessier, Johann Rafelski, Hadrons and Quark-Gluon Plasma, Cambridge University Press (2002).

[29] J. W. Harris and B. Müller, Ann. Rev. Nucl. Part. Sci. **46**, 71 (1996), and references therein.

[30] S. A. Bass, M. Gyulassy, and H. Stöcker and W. Greiner, J. Phys. G: Nucl. Part. Phys. **25**, R1 (1999), and references therein; [arXiv:hep-ph/9810281].

[31] M. Marx *et al.*, Proceedings of the 15th Int. Conference on Ultra-Relativistic Nucleus-Nucleus Collisions. (Stony Brook, New York, USA, Nucl. Phys. A **698**, 2002).

[32] H. H. Gutbrod *et al.*, Proceedings of the 16th Int. Conference on Ultra-Relativistic Nucleus-Nucleus Collisions. (Nantes, France, Nucl. Phys. A **715**, 2003).

[33] H. G. Ritter *et al.*, Proceedings of the 17th Int. Conference on Ultra-Relativistic Nucleus-Nucleus Collisions. (Oakland, California, USA, J. Phys. G: Nucl. Part. Phys. **30**, S633, 2004).

[34] STAR WhitePaper, [arXiv:nucl-ex/0501009].

[35] PHENIX WhitePaper, [arXiv:nucl-ex/0410003].

[36] PHOBOS WhitePaper, [arXiv:nucl-ex/0410022].

[37] BRAHMS WhitePaper, [arXiv:nucl-ex/0410020].

[38] L. D. Landau and E. M. Lifshitz, Fluid Mechanics, 2nd ed., World Publishing Corp., (1999).

[39] W. Reisdorf and H. G. Ritter, Ann. Rev. Nucl. Part. Sci. **47**, 663 (1997).

[40] N. Herrmann, J. P. Wessels and T. Wienold, Ann. Rev. Nucl. Part. Sci. **49**, 581 (1999).

[41] P. F. Kolb and U. Heinz, Hydrodynamic description of ultrarelativistic heavy-ion collisions, *Quark Gluon Plasma, 3* edited by R.C. Hwa and X.N. Wang, World Scientific, Singapore (2004); [arXiv:nucl-th/0305084].

[42] P. Huovinen, Hydrodynamic description of collective flow, *Quark Gluon Plasma, 3* edited by R.C. Hwa and X.N. Wang, World Scientific, Singapore (2004); [arXiv:nucl-th/0305064].

[43] D. Teaney, J. Lauret, and E.V. Shuryak, Phys. Rev. Lett. **86**, 4783 (2001); [arXiv:nucl-th/0011058].

[44] R. Snellings *et al.*, STAR Collaboration, Nucl. Phys. A **698**, 193c (2002).

[45] Y. Lu *et al.*, RQMD v_2, in preparation.

[46] I. Vitev and M. Gyulassy, Phys. Rev. C **65**, 041902 (2002).

[47] H. Sorge, Phys. Rev. Lett. **78**, 2309 (1997); Phys. Rev. Lett. **82**, 2048 (1999).

[48] Z. Lin and C.M. Ko, Phys. Rev. Lett. **89**, 202302 (2002).

[49] D. Molnár and S.A. Voloshin, Phys. Rev. Lett. **91**, 092301 (2003).

[50] R.C. Hwa and C.B. Yang, Phys. Rev. C **67**, 064902 (2003).

[51] R.J. Fries, B. Müler, C. Nonaka, and S.A. Bass, Phys. Rev. Lett. **90**, 202303 (2003).

[52] V. Greco, C.M. Ko, and p. Levai, Phys. Rev. Lett. **90**, 202302 (2003).

[53] N. Xu and Z. Xu, Nucl. Phys. A **715**, 587c (2003); [arXiv:nucl-ex/0211012].

[54] D. Teaney, J. Lauret, E.V. Shuryak, Nucl. Phys. A **698**, 479c (2002); [arXiv:nucl-th/0110037].

[55] J. Adams *et al.*, STAR Collaboration, Phys. Rev. Lett. **92**, 052302 (2004); [arXiv:nucl-ex/0306007].

[56] E. Schnedermann, J. Sollfrank and U. Heinz, Phys. Rev. C **48**, 2462 (1993).

[57] X.N. Wang and M. Gyulassy, Phys. Rev. Lett. **68**, 1480 (1992); X.N. Wang, Phys. Rev. C **58**, 2321 (1998).

[58] X.N. Wang, Proceedings of RIKEN BNL Research Center Workshop, Vol. **62**; Nucl. Phys. A **750**, 98 (2005).

[59] J. Adams *et al.*, STAR Collaboration, Phys. Rev. Lett. **90**, 082302 (2003); [arXiv:nucl-ex/0210033].

[60] J. Adams *et al.*, STAR Collaboration, Phys. Rev. Lett. **91**, 072304 (2003); [arXiv:nucl-ex/0306024].

[61] S. S. Adler *et al.*, PHENIX Collaboration, Phys. Rev. Lett. **91**, 072303 (2003).

[62] I. Arsene *et al.*, BRAHMS Collaboration, Phys. Rev. Lett. **91**, 072305 (2003).

[63] B. B. Back *et al.*, PHOBOS Collaboration, Phys. Rev. Lett. **91**, 072302 (2003).

[64] D. Kharzeev, E. Levin, and L. McLerran, Phys. Lett. B **561**, 93 (2003).

[65] N. Xu, Prog. in Part. and Nucl. Phys. **53**, 165 (2004).

[66] R. W. Wilson, Rev. Mod. Phys. **51**, 433 (1979).

[67] T. Ferbel and W. R. Molzon, Rev. Mod. Phys. **56**, 181 (1984).

[68] T. Peitzmann and M. H. Thoma, Phys. Rep. **364**, 175-246 (2002); [arXiv:hep-ph/0111114].

[69] J. Frantz (fot the PHENIX collaboration), J. Phys. G: Nucl. Part. Phys. **30**, S1003 (2004); [arXiv:nucl-ex/0404006].

[70] J. Adams *et al.*, STAR Collaboration, Phys. Rev. C **70**, 044902 (2004); [arXiv:nucl-ex/0401008].

[71] H. Sorge, Phys. Rev. C **52**, 3291 (1995); [arXiv:nucl-th/9509007].

[72] Special Issue: The Relativistic Heavy Ion Collider Project: RHIC and its Detectors, Nucl. Instrum. Methods Phys. Res., Sect. A **499**, v (2003).

[73] K.H. Ackermann *et al.*, Nucl. Instrum. Methods Phys. Res., Sect. A **499**, 624 (2003).

[74] M. Harrison *et al.*, Ann. Rev. Nucl. Part. Sci. **52**, 452 (2002).

[75] M. Harrison *et al.*, Nucl. Instrum. Methods Phys. Res., Sect. A **499**, 235 (2003).

[76] C. Adler *et al.*, Nucl. Instrum. Methods Phys. Res., Sect. A **499**, 433 (2003).

[77] C. Adler *et al.*, Nucl. Instrum. Methods Phys. Res., Sect. A **470**, 488 (2001).

[78] M. Adamczyk *et al.*, Nucl. Instrum. Methods Phys. Res., Sect. A **499**, 437 (2003).

[79] B.B. Back *et al.*, Nucl. Instrum. Methods Phys. Res., Sect. A **499**, 603 (2003).

[80] K. Adcox *et al.*, Nucl. Instrum. Methods Phys. Res., Sect. A **499**, 469 (2003).

[81] F. Bergsma *et al.*, Nucl. Instrum. Methods Phys. Res., Sect. A **499**, 633 (2003).

[82] M. Adnerson *et al.*, Nucl. Instrum. Methods Phys. Res., Sect. A **499**, 659 (2003).

[83] R. Bellwied *et al.*, Nucl. Instrum. Methods Phys. Res., Sect. A **499**, 640 (2003).

[84] L. Arnold *et al.*, Nucl. Instrum. Methods Phys. Res., Sect. A **499**, 652 (2003).

[85] J. Abele *et al.*, Nucl. Instrum. Methods Phys. Res., Sect. A **499**, 633 (2003).

[86] K.H. Ackermann *et al.*, Nucl. Instrum. Methods Phys. Res., Sect. A **499**, 713 (2003).

[87] M. Beddo *et al.*, Nucl. Instrum. Methods Phys. Res., Sect. A **499**, 725 (2003).

[88] C.E. Allgower *et al.*, Nucl. Instrum. Methods Phys. Res., Sect. A **499**, 740 (2003).

[89] J.M. Landgraf *et al.*, Nucl. Instrum. Methods Phys. Res., Sect. A **499**, 762 (2003).

[90] F.S. Bieser *et al.*, Nucl. Instrum. Methods Phys. Res., Sect. A **499**, 766 (2003).

[91] C. Adler *et al.*, Nucl. Instrum. Methods Phys. Res., Sect. A **499**, 778 (2003).

[92] B.G. Gibbard, T.G. Throwe, Nucl. Instrum. Methods Phys. Res., Sect. A **499**, 814 (2003).

[93] A.W. Chan *et al.*, Nucl. Instrum. Methods Phys. Res., Sect. A **499**, 819 (2003).

[94] L. Kotchenda *et al.*, Nucl. Instrum. Methods Phys. Res., Sect. A **499**, 703 (2003).

[95] W.J. Llope *et al.*, Nucl. Instrum. Methods Phys. Res., Sect. A **522**, 252 (2004).

[96] B. Bommer *et al.*, Nucl. Instrum. Methods Phys. Res., Sect. A **508**, 181 (2003).

[97] L.J. Ruan, Ph.D. Thesis, USTC, (2004); [arXiv:nucl-ex/0503015]

[98] Zhixu Liu *et al.*, High Energy Physics and Nuclear Physics, **27**, 72 (2003).

[99] W.J. Llope *et al.*, Nucl. Instrum. Methods Phys. Res., Sect. A **443**, 451 (2000).

[100] Y. Tanaka *et al.*, Nucl. Instrum. Methods Phys. Res., Sect. A **425**, 323 (1999).

[101] The STAR TOF Collaboration, *Proposal for a Large Area Time of Flight System for STAR*.

[102] CERN Program Library Long Writeup W5013, Detector Description and Simulation Tool. See also http://wwwasd.web.cern.ch/wwwasd/geant/.

[103] T. D. Lee, Proceedings of RIKEN BNL Research Center Workshop, Vol. **62**; Nucl. Phys. A **750**, 1 (2005).

[104] T. Sjötrand *et al.*, Computer Physics Commun. **135**, 238 (2001).

[105] X.N. Wang *et al.*, Phys. Rev. D **44**, 3501 (1991).

[106] S. A. Bass *et al.*, Prog. in Part. and Nucl. Phys. **41**, 255 (1998), [arXiv:nucl-th/9803035]; M. Bleicher *et al.*, J. Phys. G: Nucl. Part. Phys. **25**, 1859 (1999), [arXiv:hep-ph/9909407].

[107] Z.W. Lin *et al.*, Phys. Rev. C **64**, 011902(R) (2001); [arXiv:nucl-th/0011059].

[108] F.M. Liu *et al.*, Phys. Rev. D **67**, 034011 (2003); H.J. Drescher *et al.*, Phys. Rep. **350**, 93-289 (2001).

[109] K. Werner, J. Phys. G: Nucl. Part. Phys. **27**, 625 (2001).

[110] N. Xu and M. Kaneta, Nucl. Phys. A **698**, 306c (2001).

[111] R. Brun *et al.*, Nucl. Instrum. Methods Phys. Res., Sect. A **389**, 81 (1997). See also http://root.cern.ch/.

[112] F. Videbæk *et al.*, Phys. Rev. C **52**, 2684 (1995).

[113] S.S. Adler *et al.*, Phys. Rev. C **69**, 034909 (2004); [arXiv:nucl-ex/0307010].

[114] S. Esumi *et al.*, Phys. Rev. C **55**, R2163 (1997).

[115] H. van Hecke, H. Sorge, N. Xu, Phys. Rev. Lett. **81**, 5764 (1998); [arXiv:nucl-th/9804035].

[116] Y. Cheng *et al.*, Phys. Rev. C **68**, 034910 (2003).

[117] Y. Cheng *et al.*, Mod. Phys. Lett. A, Vol. 18, No. 16 (2003) 1107-1112.

[118] R. Bossingham *et al.*, STAR Note 281, STAR Offline Simulation and Analysis Software Design (unpublished).

[119] M.A. Lisa, STAR Note 238, The STAR-TPC Clusterfinder/Hitfiner (unpublished).

[120] Howard Matis, STAR Note 121, STAR Coordinate System (unpublished).

[121] Dietrich Liko, STAR Note 87, Track Fitting in the STAR Detector using the Kalman Filter Method (unpublished).

[122] S. Margetis and D. Cebra, STAR Note 89, Main Vertex Reconstruction in STAR (unpublished).

[123] Jeffery T. Mitchell and Iwona M. Sakrejda, STAR Note 190, Tracking for the STAR TPC, Documentation and User's Guide (unpublished).

[124] A. Tang, Ph.D. Thesis, Kent University, (2002).

[125] Manuel Calderón de la Barca Sánchez, Ph.D. Thesis, Yale University, (2001).

[126] J. Adams *et al.*, STAR Collaboration, [arXiv:nucl-ex/0133017].

[127] Masashi Kaneta, Ph.D. Thesis, Hiroshima University, (1999).

[128] J. Adams *et al.*, STAR Collaboration, [arXiv:nucl-ex/0306029]; C. Adler *et al.*, Phys. Rev. Lett. **86**, 4778(2001); **90**, 119903(2003).

[129] J. Adams *et al.*, STAR Collaboration, Phys. Rev. Lett. **92**, 112301 (2004); [arXiv:nucl-ex/0310004].

[130] Eugene Toyonari Yamamoto, Ph.D. Thesis, UCLA, (2001).

[131] K. Adcox *et al.*, PHENIX Collaboration, Phys. Rev. Lett. **88**, 242301 (2002).

[132] Zhixu Liu *et al.* "The Design and Implementation of BESIII Online Test Farm (in Chinese)" *report on NED2004*.

List of Publications

1. **Zhixu Liu**, Jinghua Fu & Lianshou Liu, High Energy Physics and Nuclear Physics, **24** (2000) 787, *"Influence of Multiplicity Fluctuation on the Erraticity Behaviour in High Energy Collsions"*.

2. C. Adler, *et al.*, STAR Collaboration, Phys. Rev. Lett. **87**, 262302 (2001), *"Measurement of Inclusive Antiprotons from Au + Au Collisions at* $\sqrt{s_{NN}} = 130$ *GeV"*, [arXiv:nucl-ex/0110009].

3. C. Adler, *et al.*, STAR Collaboration, Phys. Rev. Lett. **89**, 092301 (2002), *"Midrapidity* Λ *and* $\bar{\Lambda}$ *Production in Au + Au Collisions at* $\sqrt{s_{NN}} = 130$ *GeV"*, [arXiv:nucl-ex/0203016].

4. C. Adler, *et al.*, STAR Collaboration, Phys. Rev. Lett. **89**, 132301 (2002), *"Azimuthal Anisotropy of* K^0_S *and* Λ + $\bar{\Lambda}$ *Production at Midrapidity from Au + Au Collisions at* $\sqrt{s_{NN}} = 130$ *GeV"*, [arXiv:hep-ex/0205072].

5. C. Adler, *et al.*, STAR Collaboration, Phys. Rev. Lett. **89**, 202301 (2002), *"Centrality Dependence of High-*p_T *Hadron Suppression in Au + Au Collisions at* $\sqrt{s_{NN}} = 130$ *GeV"*, [arXiv:nucl-ex/0206011].

6. C. Adler, *et al.*, STAR Collaboration, Phys. Rev. Lett. **89**, 272302 (2002), *"Coherent* ρ^0 *Production in Ultraperipheral Heavy-Ion Collisions"*, [arXiv:nucl-ex/0206004].

7. C. Adler, *et al.*, STAR Collaboration, Phys. Rev. C **66**, 034904 (2002), *"Elliptic flow from two- and four-particle correlations in Au + Au collisions at* $\sqrt{s_{NN}} = 130$ *GeV"*, [arXiv:nucl-ex/0206001].

8. C. Adler, *et al.*, STAR Collaboration, Phys. Rev. C **66**, 061901(R) (2002), *"*$K^*(892)^0$ *production in relativistic heavy ion collisions at* $\sqrt{s_{NN}} = 130$ *GeV"*, [arXiv:nucl-ex/0205015].

9. C. Adler, *et al.*, STAR Collaboration, Phys. Rev. Lett. **90**, 032301 (2003), *"Azimuthal Anisotropy and Correlations in the Hard Scattering Regime at RHIC"*, [arXiv:nucl-ex/0206006].

10. C. Adler, *et al.*, STAR Collaboration, Phys. Rev. Lett. **90**, 082302 (2003), *"Disappearance of Back-To-Back High-*p_T *Hadron Correlations in Central Au + Au Collisions at* $\sqrt{s_{NN}} = 200$ *GeV"*, [arXiv:nucl-ex/0210033].

11. J. Adams, *et al.*, STAR Collaboration, Phys. Rev. Lett. **90**, 172301 (2003), *"Narrowing of the Balance Function with Centrality in Central Au + Au Collisions at $\sqrt{s_{NN}}=130$ GeV"*, [arXiv:nucl-ex/0301014].

12. J. Adams, *et al.*, STAR Collaboration, Phys. Rev. Lett. **91**, 072304 (2003), *"Evidence from d + Au Measurements for Final-State Suppression of High-p_T Hadrons in Au + Au Collisions at RHIC"*, [arXiv:nucl-ex/0306024].

13. J. Adams, *et al.*, STAR Collaboration, Phys. Rev. Lett. **91**, 172302 (2003), *"Transverse-Momentum and Collision-Energy Dependence of High-p_T Hadron Suppression in Au + Au Collisions at Ultrarelativistic Energies"*, [arXiv:nucl-ex/0305015].

14. J. Adams, *et al.*, STAR Collaboration, Phys. Rev. Lett. **91**, 262301 (2003), *"Three-Pion Hanbury Brown-Twiss Correlations in Relativistic Heavy-Ion Collisions from the STAR Experiment"*, [arXiv:nucl-ex/0306028].

15. J. Adams, *et al.*, STAR Collaboration, Phys. Rev. Lett. **91**, 262302 (2003), *"Pion-Kaon Correlations in Central Au + Au Collisions at $\sqrt{s_{NN}} = 130$ GeV"*, [arXiv:nucl-ex/0307025].

16. J. Adams, *et al.*, STAR Collaboration, Phys. Lett. B **567**, (2003), 167-174, *"Strange antiparticle-to-particle ratios at mid-rapidity in $\sqrt{s_{NN}}=130$ GeV Au + Au collisions"*, [arXiv:nucl-ex/0211024].

17. Y. Cheng, F. Liu, **Z. Liu**, K. Schweda, N. Xu, Phys. Rev. C **68**, 034910 (2003), *"Transverse expansion in ^{197}Au + ^{197}Au collisions at RHIC"*.

18. J. Adams, *et al.*, STAR Collaboration, Phys. Rev. C **68**, 044905 (2003), *"Net charge fluctuations in Au + Au collisions at $\sqrt{s_{NN}} = 130$ GeV"*, [arXiv:nucl-ex/0307007].

19. **Zhixu Liu**, Feng Liu & Bingyun Zhang, High Energy Physics and Nuclear Physics, **27**, 253 (2003), *"A PC-Linux Based Data Acquisition System for the STAR TOFp Detector"*.

20. J. Adams, *et al.*, STAR Collaboration, Phys. Rev. Lett. **92**, 052302 (2004), *"Particle-Type Dependence of Azimuthal Anisotropy and Nuclear Modification of Particle Production in Au + Au Collisions at $\sqrt{s_{NN}} = 200$ GeV"*, [arXiv:nucl-ex/0306007].

21. J. Adams, *et al.*, STAR Collaboration, Phys. Rev. Lett. **92**, 062301 (2004), *"Azimuthal Anisotropy at the Relativistic Heavy Ion Collider: The First and Fourth Harmonics"*, [arXiv:nucl-ex/0310029].

22. J. Adams, *et al.*, STAR Collaboration, Phys. Rev. Lett. **92**, 092301 (2004), *"ρ^0 Production and Possible Modification in Au + Au and p + p Collisions at $\sqrt{s_{NN}}=200$ GeV"*, [arXiv:nucl-ex/0307023].

23. J. Adams, *et al.*, STAR Collaboration, Phys. Rev. Lett. **92**, 112301 (2004), *"Identified Particle Distributions in pp and Au + Au Collisions at $\sqrt{s_{NN}} = 200$ GeV"*, [arXiv:nucl-ex/0310004].

24. J. Adams, *et al.*, STAR Collaboration, Phys. Rev. Lett. **92**, 171801 (2004), *"Cross Sections and Transverse Single-Spin Asymmetries in Forward Neutral-Pion Production from Proton Collisions at* $\sqrt{s_{NN}} = 200$ *GeV"*, [arXiv:hep-ex/0310058].

25. J. Adams, *et al.*, STAR Collaboration, Phys. Rev. Lett. **92**, 182301 (2004), *"Multistrange Baryon Production in Au + Au Collisions at* $\sqrt{s_{NN}} = 130$ *GeV"*, [arXiv:nucl-ex/0307024].

26. J. Adams, *et al.*, STAR Collaboration, Phys. Rev. Lett. **93**, 012301 (2004), *"Azimuthally Sensitive Hanbury Brown-Twiss Interferometry in Au + Au Collisions at* $\sqrt{s_{NN}} = 200$ *GeV"*, [arXiv:nucl-ex/0312009].

27. J. Adams, *et al.*, STAR Collaboration, Phys. Rev. Lett. **93**, 252301 (2004), *"Azimuthally Anisotropy and Correlations at Large Transverse Momenta in p + p and Au + Au Collisions at* $\sqrt{s_{NN}} = 200$ *GeV"*, [arXiv:nucl-ex/0407007].

28. C. Adler, *et al.*, STAR Collaboration, Phys. Lett. B **595**, (2004), 143-150, *"Kaon production and kaon to pion ratio in Au + Au collisions at* $\sqrt{s_{NN}} = 130$ *GeV"*, [arXiv:nucl-ex/0206008].

29. J. Adams, *et al.*, STAR Collaboration, Phys. Rev. C **70**, 031902(R) (2004), *"Production of* e^+e^- *pairs accompanied by nuclear dissociation in ultraperipheral heavy-ion collisions"*, [arXiv:nucl-ex/0404012].

30. J. Adams, *et al.*, STAR Collaboration, Phys. Rev. C **70**, 041901(R) (2004), *"Rapidity and centrality dependence of proton and antiproton production from* $^{197}Au + {}^{197}Au$ *collisions at* $\sqrt{s_{NN}} = 130$ *GeV"*, [arXiv:nucl-ex/0306029].

31. J. Adams, *et al.*, STAR Collaboration, Phys. Rev. C **70**, 044901 (2004), *"Centrality and pseudorapidity dependence of charged hadron production at intermediate* p_T *in Au + Au collisions at* $\sqrt{s_{NN}} = 130$ *GeV"*, [arXiv:nucl-ex/0404020].

32. J. Adams, *et al.*, STAR Collaboration, Phys. Rev. C **70**, 044902 (2004), *"Photon and neutral pion production in Au + Au collisions at* $\sqrt{s_{NN}} = 130$ *GeV"*, [arXiv:nucl-ex/0401008].

33. J. Adams, *et al.*, STAR Collaboration, Phys. Rev. C **70**, 054907 (2004), *"Measurements of transverse energy distributions in Au + Au collisions at* $\sqrt{s_{NN}} = 200$ *GeV"*, [arXiv:nucl-ex/0407003].

34. J. Adams, *et al.*, STAR Collaboration, Phys. Rev. C **70**, 064907 (2004), *"Pseudorapidity asymmetry and centrality dependence of charged Hadron spectra in d + Au collisions at* $\sqrt{s_{NN}} = 200$ *GeV"*, [arXiv:nucl-ex/0408016].

35. K.H. Ackermann, *et al.*, STAR Collaboration, Nucl. Instrum. Methods Phys. Res., Sect. A **499**, (2003) 624-632, *"STAR detector overview"*.

36. W.J. Llope, F. Geurts, J.W. Mitchell, **Z. Liu**, *et al.*, Nucl. Instrum. Methods Phys. Res., Sect. A **522**, (2004) 252-273, *"The TOFp/pVPD time-of-flight system for STAR"*, [arXiv:nucl-ex/0308022].

37. J. Adams, *et al.*, STAR Collaboration, Phys. Rev. Lett. **94**, 062301 (2005), *"Open Charm Yields in d + Au collisions at* $\sqrt{s_{NN}} = 200$ *GeV"*, [arXiv:nucl-ex/0407006].

38. **Zhixu Liu**, Feng Liu, Kejun Zhu, Fei Li, *"The Design and Implementation of BESIII Online Test Farm (in Chinese)"* , *report on NED2004, KunMing*; submitted to Nuclear Electronics and Detection Technology.

39. J. Adams, *et al.*, STAR Collaboration, Phys. Rev. C **71**, 031901(R) (2005), *"Transverse-momentum dependent modification of dynamic texture in central Au + Au collisions at* $\sqrt{s_{NN}} = 200$ *GeV"*, [arXiv:nucl-ex/0407001].

Acknowledgements

Thanks go to lots of people!

At first, I would like to thank Professor Liu Lianshou who guide me to the way of high energy physics experiment. He provides the chance and strong support for me to participate in the STAR TOFp DAQ project in 1999, which is a challenge for me as a undergraduate student and is very interesting too! Besides the job, his religious attitude on the studying and research will influence me forever! I always feel lucky to meet such a best and respectful teacher!

I'm grateful to my supervisor Professor Liu Feng and Professor Xu Nu too. Only with Liu Feng's guide, support and trust I can made the success on TOFp DAQ project and the later physics analysis. Xu Nu provides a chance for me doing some physics analysis on the most exciting experiment facility in the world and choose this nice topic for me. During the stage, they are always so kind and patient in guiding me, both on research and living.

Thanks to Dr. Xu Zhangbu, he gave me lots of help both on the work and life when I stayed in BNL. Thanks to Dr. K. Schweda for the valuable discussions and help on the topic of this thesis.

Thanks to all the professors, staffs and classmates in IOPP.

Thanks to all my friends! A bosom friend afar brings distance near! 海内存知己，天涯若比邻！

Thanks to every member of the STAR collaboration and the RHIC operations group. Only with their intelligence and hard work, we have such a successful hardware and software which help us to investigate the universe we're living in!

Thanks to Linux, the most excellent operating system, which provide great help on our work and bring many joys to our life too! Thanks to LaTeX which make the writing of this dissertation smooth and full of pleasure!

Finally, I'd like to thank my parents and young sister. Without their sacrifice and support, I won't be here.